

AD-A168 794

EXPERIMENTAL AND THEORETICAL INVESTIGATION OF MICROWAVE
MILLIMETER RADIAT (U) MARYLAND UNIV COLLEGE PARK LAB
FOR PLASMA AND FUSION ENERGY S. M W DESTLER 30 NOV 85

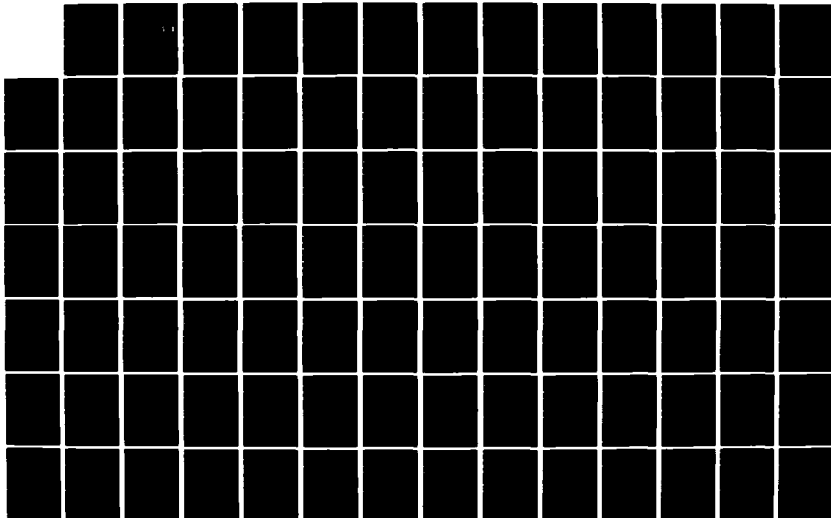
1/2

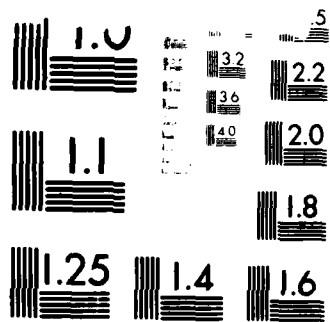
UNCLASSIFIED

AFOSR-TR-86-0280 AFOSR-83-0013

F/G 20/14

NL





M. H.

②
Z

AFOSR-TR- 86 - 0 2 80

AD-A168 794

EXPERIMENTAL AND THEORETICAL INVESTIGATION OF MICROWAVE AND
MILLIMETER WAVE RADIATION FROM HOLLOW, ROTATING ELECTRON BEAMS

Contract No. AFOSR-83-0013

DTIC
SELECTE
JUN 12 1986
S D D

FINAL PROGRESS REPORT

For the Period December 1, 1984 through November 30, 1985

Submitted to

Air Force Office of Scientific Research

Prepared by

The Electrical Engineering Department and
The Laboratory for Plasma and Fusion Energy Studies
University of Maryland
College Park, Maryland 20742

Approved for public release;
distribution unlimited.

DTIC FILE COPY

86 6 10 133

UNCLASSIFIED

SECURITY CLASSIFICATION OF THIS PAGE (When Data Entered)

REPORT DOCUMENTATION PAGE		READ INSTRUCTIONS BEFORE COMPLETING FORM
1. REPORT NUMBER AFOSR-TR- 86-0280	2. GOVT ACCESSION NO. AD-A168794	3. RECIPIENT'S CATALOG NUMBER
4. TITLE (and Subtitle) EXPERIMENTAL & THEORETICAL INVESTIGATION OF MICROWAVE & MILLIMETER WAVE RADIATION FROM HOLLOW, ROTATING ELECTRON BEAMS		5. TYPE OF REPORT & PERIOD COVERED FINAL 1 Dec 84 - 30 Nov 85
7. AUTHOR(s) Dr William W Destler		6. PERFORMING ORG. REPORT NUMBER
9. PERFORMING ORGANIZATION NAME AND ADDRESS University of Maryland College Park, MD 20742		8. CONTRACT OR GRANT NUMBER(s) AFOSR 83-0013
11. CONTROLLING OFFICE NAME AND ADDRESS AFOSR/NP Bldg 410 Bolling AFB DC 20332-6448		10. PROGRAM ELEMENT, PROJECT, TASK AREA & WORK UNIT NUMBERS 61102F 2301/A8
14. MONITORING AGENCY NAME & ADDRESS (if different from Controlling Office) AFOSR/NP Bldg 410 Bolling AFB DC 20332-6448		12. REPORT DATE 30 Nov 1985
		13. NUMBER OF PAGES 107
		15. SECURITY CLASS. (of this report) Unclassified
16. DISTRIBUTION STATEMENT (of this Report) Approved for public release; distribution unlimited		15a. DECLASSIFICATION DOWNGRADING SCHEDULE
17. DISTRIBUTION STATEMENT (of the abstract entered in Block 20, if different from Report)		
18. SUPPLEMENTARY NOTES		
19. KEY WORDS (Continue on reverse side if necessary and identify by block number)		
20. ABSTRACT (Continue on reverse side if necessary and identify by block number) Research on microwave gener- ation from rotating electron beams in various conducting boundary systems has been pursued at the University of MD under AFOSR sponsorship for several years. Recently, the major emphasis of this research has been on the production of radiation from rotating electron beams in magetron-like conducting boundary systems. These experimental configurations are now recognized as an entirely new type of microwave tube, referred to in the literature as a Gyromagnetron, High Harmonic Gyrotron, or Cust Injected Magnetron (Cusptron).		

DD FORM 1473
1 JAN 73

86 6 10 133

UNCLASSIFIED

SECURITY CLASSIFICATION OF THIS PAGE (When Data Entered)

FINAL PROGRESS REPORT

Submitted to: Air Force Office of Scientific Research

Submitted by: Electrical Engineering Department
Laboratory for Plasma and Fusion Energy Studies
University of Maryland
College Park, Maryland 20742

Principal Investigators: William W. Destler, Professor
Electrical Engineering Department

Charles D. Striffler, Professor
Electrical Engineering Department

Title of Research: "Experimental and Theoretical Investigation
of Microwave and Millimeter Wave Radiation
from Hollow, Rotating Electron Beams"

Accession For	
NTIS CRA&I	<input checked="" type="checkbox"/>
DTIC TAB	<input type="checkbox"/>
Unannounced	<input type="checkbox"/>
Justification	
By	
Distribution /	
Availability Codes	
Dist	Avail and/or Special
A-1	



I. INTRODUCTION

Research on microwave generation from rotating electron beams in various conducting boundary systems has been pursued at the University of Maryland under AFOSR sponsorship for several years. Recently, the major emphasis of this research has been on the production of radiation from rotating electron beams in magnetron-like conducting boundary systems. These experimental configurations are now recognized as an entirely new type of microwave tube, referred to in the literature as a Gyromagnetron, High Harmonic Gyrotron, or Cusp Injected Magnetron (Cusptron). The interest in this new device has centered around its potential to reduce the required magnetic field in microwave tubes by an order of magnitude by allowing operation at a high harmonic of the electron cyclotron frequency.

This area of research has seen substantial progress during the last year, and a summary of theoretical and experimental research conducted during this period is presented in Section II. Results from research on millimeter and submillimeter waves produced by rotating electron beams in rippled magnetic fields, partially funded by AFOSR (with additional funds from DOE) are also summarized in Section II of this progress report.

II. FINAL PROGRESS REPORT

For the Period December 1, 1984 to November 30, 1985

A. Experimental Research

1. Improvements to the Experimental Facilities

During the past year the experimental facilities have been enhanced by the installation of a completely digital fast data acquisition system funded by a grant from AFOSR under the DOD-University Instrumentation Program. This new system includes five channels of Tektronix 7912AD fast digitization controlled by a DEC 11/73 computer. Additional equipment related to this project includes an Imagen laser printer and several graphics terminals. This facility has been installed in a separate shielded room in our high bay area, and is currently being connected to the various experiments it is designed to support. In addition to this facility, a 40 kV, 40 A, 5 μ s pulse modulator has been installed to power the CUSPTRON experiment, and this new modulator is now fully operational. Additional remarks about the experimental facilities can be found in Section III of this progress report.

2. High Power Microwave Experiments

Experiments designed to use the high voltage rotating beam facility have produced significant results during the past year. These experiments, in which a rotating electron beam interacts with the modes of a magnetron-type conducting boundary system, have demonstrated that efficient radiation

can be produced using either annular sector resonator or hole and slot resonator configurations. Using a 2 MeV, 1-2 kA, 5 ns rotating electron beam pulse, about 300 MW have been produced at 8 GHz using a hole and slot resonator system with ten resonators, and about 500 MW have been produced at 15.5 GHz using a 20 slot annular sector resonator system. These results are detailed in a paper entitled, "High Power Microwave Generation from a Large Orbit Gyrotron with Vane and Hole and Slot Resonators," published in the IEEE Trans. Plasma Science (special issue on high power microwave generation) and enclosed in Appendix B.

3. Millimeter Wave Generation from Rotating Beams in Rippled Magnetic Fields

These experiments, conducted in collaboration with Professor George Bekefi's group at MIT, are designed to investigate a novel kind of free electron laser configuration. In this work, a rotating beam interacts with an azimuthally periodic wiggler field provided by samarium cobalt magnets located interior and exterior to the beam. Narrow band radiation at power levels in excess of 200 kW has been observed at 90 GHz and 180 GHz in these experiments, and the studies are detailed in a paper entitled, "Millimeter Wave Generation from a Rotating Electron Beam in a Rippled Magnetic Field," published in the Physics of Fluids and enclosed in Appendix B.

4. CUSPTRON Experiments

These experiments on our low voltage table top rotating beam facility (25-40 kV, 1-2 A, 5 μ s, 100 pps) are now fully underway. Over 500 W of microwave power at the sixth harmonic of the cyclotron frequency have been

observed when the rotating beam interacts with a six slot vane resonator system, and experiments designed to produce radiation at the twelfth harmonic are currently in progress. The potential of this new device lies in the extremely low magnetic fields required for its operation (typically 200 gauss compared to many kilogauss for comparable magnetrons or gyrotrons).

B. Theoretical Research

The theoretical contributions to our research this past year have been the best since the inception of our program. Not only have details of the many calculations that have been done by our group merged into common agreement, but our ideas as to how systems should be designed to enhance radiation have been quantified. We believe that we can now delineate the main factors that determine the best conditions for optimum coupling of a rotating beam to a given wall geometry. The theoretical areas studied were:

- The stability of a thin E layer via a Vlasov formalism was completed and shown to agree with the single particle approach. This was used to study the interaction of a thin rotating E layer with a vane resonator wall structure (see Refs. 23 and 28 of Appendix A).
- It was proved that for a cusp injected system the 2π mode of the waveguide structure is the dominant mode of operation. Thus, the injection radius of the beam selects the proper radial mode number of

the " 2π " harmonic, and for strong coupling the beam must be close to the slotted wall structure. However, most of the energy is coupled into the fundamental mode (see Ref. 28 of Appendix A).

- Both resonant and nonresonant interaction is considered via the Vlasov and fluid formalisms. For the nonresonant, long wavelength limit, the traditional negative mass instability is recovered (see Refs. 23, 29, and 30 of Appendix A).
- The derivation of a general growth rate expression for systems involving large orbit, thin, annular, relativistic electron beams was completed. This growth rate formula is written in terms of parameters which contain the required information about the waveguide wall structure. This method extends previous results to systems whose empty waveguide modes are hybrids. As an example of this latter case, growth rates for coaxial systems with dielectric liners are calculated via this formalism. The use of dielectric liners may be very useful for low energy systems where it is difficult to simultaneously have resonant interaction at a strong coupling position of the beam (see Ref. 31 in Appendix A).
- The production of high power microwave radiation from a large orbit gyrotron in azimuthally periodic boundary systems was studied theoretically. Linear growth rates are calculated for the 2π modes of magnetron-like vane resonator (VR) and hole-and-slot resonator (HASR) systems using a general growth rate formalism. This formalism

was used to design the resonator structures for the experiments performed in our laboratory. The radiation characteristics are in reasonably good agreement with the theoretical predictions especially with respect to radial mode competition problems (see Ref. 32 in Appendix A).

- The macroscopic fluid equations were used to study the effect of beam thickness on the linear growth rates of large orbit gyrotron configurations. Two methods were used to calculate the growth rates. The analytic approach solves the problem to first order in the ratio of beam thickness to the average beam radius and recovers the zero thickness limit. The numeric approach uses complete orthonormal systems comprised of the homogeneous wave equation solutions to calculate the growth rates for beams with arbitrary thicknesses. It is concluded that thick, tenuous beams in resonant systems must be operated near the cutoff of the EM wave. The decrease in growth rate as the wavelength decreases is attributed to the loss of synchronism in systems where the beam has a spread in its canonical angular momentum [see Ref. 33 in Appendix A (paper in the process of being written)].
- The study of single particle motion in hollow-cylindrical waveguide fields has been initiated. A purely linearized analytic approach can be used for particles far from resonance and an analytic-iterative analysis can be used for particles that are near or at resonant if they are trapped. These analytic results are compared to a numerical

solution of the equations of motion. The main information in which we are interested pertains to the process of physical bunching and to the net energy gained or lost by a representative group of particles in the electromagnetic field. We define the magnitude of physical bunching by the percentage of particles trapped in their azimuthal wave period. The effect of the magnitude and slope of the electric field is also investigated. For our set of parameters, we determine that $d\gamma/dt$ is solely responsible for azimuthal bunching. This can be seen in both the linear analytic theory and the numerical solutions. We also observe that the tangential magnetic force causes a spreading of the bunch in the z direction. This spreading does not occur for $k_z = 0$ and $v_{z0} = 0$, i.e. cutoff, since in that case the tangential magnetic force is zero. Energy loss (gain) by the particles is seen to be related to both the percentage trapped and the position of the bunch in the phase of the wave [see enclosed abstract (Ref. 35 in Appendix A)].

APPENDIX A

List of Publications and Presentations Resulting from this Work

APPENDIX A

List of Publications and Presentations Resulting from this Work

1. W. W. Destler, D. W. Hudgings, M. J. Rhee, S. K. Kawasaki, and V. L. Granatstein, "Experimental Study of Microwave Generation and Suppression in a Non-Neutral E-Layer," J. Appl. Phys. 48, 3291 (1977).
2. W. W. Destler, W. Namkung, and R. L. Weiler, "Experimental Study of Intense Microwave Generation by the Negative Mass Instability," Bull. Am. Phys. Soc. 24, 1068 (1979).
3. W. Namkung, H. Romero, and C. D. Striffler, "Theoretical Study of Microwave Generation from a Rotating E-Layer-Coaxial Waveguide System," Bull. Am. Phys. Soc. 24, 1068 (1979).
4. T. F. Wang and C. D. Striffler, "Negative Mass Instability of a Relativistic E-Ring in a Hollow Waveguide," Bull. Am. Phys. Soc. 24, 1068 (1979).
5. W. W. Destler, C. D. Striffler, W. Namkung, H. Romero, and R. Weiler, "High Power Microwave Generation from an Intense Rotating Electron Beam," 1980 IEEE Int. Conf. on Plasma Science, Madison, WI, May 19-21, 1980.
6. W. W. Destler, R. Kulkarni, C. D. Striffler, and R. L. Weiler, "High Power Microwave Generation from a Cusp-Injected Magnetron," Bull. Am. Phys. Soc. II, 25, 886 (1981).
7. W. W. Destler, R. L. Weiler, and C. D. Striffler, "High Power Microwave Generation from a Rotating E-Layer in a Magnetron-Type Waveguide," Appl. Phys. Lett. 38, 570 (1981).
8. W. W. Destler, R. Kulkarni, C. D. Striffler, and R. L. Weiler, "High Power Microwave Generation from a Rotating E-Layer in Various Conducting Wall Systems," 1981 IEEE Int. Conf. on Plasma Science, Santa Fe, NM, May 18-20, 1981.
9. W. W. Destler, H. Romero, C. D. Striffler, R. L. Weiler, and W. Namkung, "Intense Microwave Generation from a Non-Neutral Rotating E-Layer," J. Appl. Phys. 52, 2740 (1981).
10. R. Kulkarni, D. Calderone, and C. D. Striffler, "Stability of a Rotating E-Layer in a Magnetron-Type Waveguide," Bull. Am. Phys. Soc. 26, 935 (1981).

11. W. W. Destler, D. Calderone, R. Kulkarni, W. Namkung, R. Weiler, and C. D. Striffler, "High-Power Microwave Generation from an Intense Rotating Electron Beam," 1982 IEEE Int. Conf. on Plasma Science, Ottawa, Ontario, Canada, May 17-19, 1982.
12. R. Kulkarni, C. D. Striffler, W. W. Destler, and R. L. Weiler, "Mode Structure and Interaction of a Rotating Relativistic Electron Beam in a Magnetron-Type Waveguide," Bull. Am. Phys. Soc. 27, 1073 (1982).
13. W. W. Destler, R. Kulkarni, C. D. Striffler, and R. L. Weiler, "Microwave Generation at High Harmonics of the Electron Cyclotron Frequency," Bull. Am. Phys. Soc. 27, 1017 (1982).
14. W. Namkung, W. Lawson, W. W. Destler, and C. D. Striffler, "Microwave Generation from a Non-Relativistic Rotating E-Layer through a Magnetic Cusp (Cusptron)," Bull. Am. Phys. Soc. 27, 1062 (1982).
15. W. W. Destler, R. Kulkarni, C. D. Striffler, and R. L. Weiler, "Microwave Generation from Rotating Electron Beams in Magnetron-Type Waveguides," J. Appl. Phys. 54, 4152 (1983).
16. C. D. Striffler, W. W. Destler, R. Kulkarni, and R. L. Weiler, "High Power Microwave Generation from Rotating E-Layers in Magnetron-Type Conducting Boundary Systems," IEEE Trans. Nucl. Sci. NS-30, 3429 (1983).
17. H. S. Uhm, C. M. Kim, and W. Namkung, "Linear Theory of Cusptron Microwave Tubes," Phys. Fluids 27, 488 (1984).
18. W. W. Destler, "Experimental Studies of High Power Microwave Generation from Rotating Electron Beams in Magnetron-Type Waveguides," Bull. Am. Phys. Soc. 28, 1087 (1983).
19. R. Kulkarni and C. D. Striffler, "Interaction of a Rotating Electron Beam with a Cylindrical Slotted Wall Structure," Bull. Am. Phys. Soc. 28, 1087 (1983).
20. W. Namkung, "Observation of Microwave Generation from a Cusptron Device," Phys. Fluids 27, 329 (1984).
21. G. Bekefi, R. E. Shefer, and W. W. Destler, "Millimeter Wave Emission from a Rotating Electron Ring in a Rippled Magnetic Field," Appl. Phys. Lett. 44, 280 (1984).
22. G. Bekefi, R. E. Shefer, and W. W. Destler, "Millimeter Wave Radiation from a Rotating Electron Beam in a Rippled Magnetic Field," IEEE Int. Conf. on Plasma Science, St. Louis, MO, May 14-16, 1984.

23. R. Kulkarni, W. W. Destler, W. G. Lawson, C. D. Striffler, and S. B. Swanekamp, "High Power Microwave Generation from a Cusp-Injected Intense Relativistic Electron Beam," IEEE Int. Conf. on Plasma Science, St. Louis, MO, May 14-16, 1984.
24. R. L. Weiler, Ph.D. Thesis, "High Power Microwave Generation from Rotating Electron Beams in Magnetron-Type Boundary Systems," 1984.
25. W. W. Destler, F. M. Aghamir, D. A. Boyd, G. Bekefi, R. E. Shefer, and Y. Z. Yin, "Experimental Study of Millimeter Wave Radiation from a Rotating Electron Beam in a Rippled Magnetic Field," Phys. Fluids (to be published, June 1985).
26. W. W. Destler and W. Lawson, "Experimental Study of High Power Microwave Generation from Rotating Electron Beams in Magnetron-Type Waveguides," Bull. Am. Phys. Soc. 29, 1281 (1984).
27. F. M. Aghamir, W. W. Destler, R. E. Shefer, G. Bekefi, and Y. Z. Yin, "Measurements of Radiation Spectra from a Rotating Electron Beam in a Rippled Magnetic Field," Bull. Am. Phys. Soc. 29, 1281 (1984).
28. R. Kulkarni and C. D. Striffler, "Stability of a Thin Rotating E-Layer with a Magnetron-Type Slotted Wall Structure," Bull. Am. Phys. Soc. 29, 1179 (1984).
29. W. Lawson and C. D. Striffler, "Theoretical Investigation of the Effect of Beam Thickness on Linear Growth Rates for Rotating, Annular, Electron Beams," Bull. Am. Phys. Soc. 29, 1179 (1984).
30. C. D. Striffler and W. Lawson, "Refinements in the Calculation of Linear Growth Rates for Thin Rotating Electron Beams in Various Cylindrical Wall Structures," Bull. Am. Phys. Soc. 29, 1281 (1984).
31. W. Lawson and C. D. Striffler, "A General Linear Growth Rate Formula for Large Orbit, Annular Electron Beams," Phys. Fluids 28 (9), 2868 (1985).
32. W. Lawson, W. W. Destler and C. D. Striffler, "High Power Microwave Generation from a Large Orbit Gyrotron in Vane and Hole-and-Slot Conducting Wall Geometries," IEEE Trans. on Plasma Science PS-13, 444 (1985).
33. W. G. Lawson, Ph.D. Thesis, "Generation of Microwave Radiation from Annular, Rotating Electron Beams in Various Waveguide Geometries," April 1985.
34. W. Lawson, W. W. Destler, and C. D. Striffler, "High Power Microwave Generation from a Large Orbit Gyrotron," 1985 Particle Accelerator Conference, May 13-16, 1985.

35. H. Bluem, W. Lawson, and C. D. Striffler, "Single Particle Trajectories in a Large Orbit Gyrotron," 1985 IEEE Int. Conf. on Plasma Science, June 3-5, 1985.
36. W. Lawson, W. W. Destler, and C. D. Striffler, "High Power Microwave Generation from a Large Orbit Gyrotron in Azimuthally Periodic Waveguide with Hole-and-Slot Resonators," 1985 IEEE Int. Conf. on Plasma Science, June 3-5, 1985.
37. W. W. Destler, F. M. Aghamir, and D. A. Boyd, "Experimental Study of Millimeter Wave Radiation from a Rotating Electron Beam in a Rippled Magnetic Field," Phys. Fluids 28 (6), 1962 (1985).
38. W. Lawson and C. D. Striffler, "A Linear Growth rate Fluid Formulation for Large Orbit, Annular Electron Layers with Finite Thickness," submitted to Phys. Fluids (to be published May 1986).

APPENDIX B
Copies of Papers Published

A general linear growth rate formula for large orbit, annular electron beams

W. Lawson and C. D. Striffler

Electrical Engineering Department and Laboratory for Plasma and Fusion Energy Studies, University of Maryland, College Park, Maryland 20742

(Received 4 February 1985; accepted 3 June 1985)

Microwave radiation can be produced at cyclotron harmonics as a result of the synchronous interaction between a rotating E layer and an em wave. The derivation of a general growth rate expression is presented here for systems involving large orbit, thin, annular, relativistic electron beams. This growth rate formula is written in terms of parameters which contain the required information about the waveguide wall structure. This method extends previous results to systems that have empty waveguide modes which are hybrids. As an example of this latter case, growth rates for coaxial systems with dielectric liners are calculated via this formalism.

I. INTRODUCTION

Microwave generation at cyclotron harmonics via large orbit, annular electron beams has received considerable attention during the past few years. Numerous theoretical and experimental efforts have resulted in a good understanding of the radiation process.¹⁻¹² Studies have been done for beams in various waveguide geometries with the magnetron's vane resonator system receiving most of the attention.

One promising device at the University of Maryland generates a rotating beam with a magnetic cusp field.¹³ This device has been used to generate power levels of 500 MW both at the 12th and 20th harmonics of the relativistic cyclotron frequency with a vane resonator system.^{14,15} The hollow E layer nominally has a particle energy of 2 MeV, a current of 1-2 kA, and a pulse length of 5-10 nsec. Other experiments on cusp-injected devices are in progress at Maryland¹⁶ and elsewhere.¹⁷ Furthermore, other injection schemes have successfully been developed.¹⁸

Several of the previous linear growth rate analyses used the fields explicitly associated with the particular waveguide in the analysis (cf. Refs. 1 and 2). This makes it necessary to repeat most of the procedure every time the waveguide geometry is changed. In fact, a large part of the analysis is independent of the waveguide and should only have to be done once. In this analysis we perform all of the geometry-independent work first. Some geometry parameters are then defined that enable us to write a growth rate formula without *a priori* knowledge of the waveguide wall structure. For a given system the geometry parameters can be found by following a simple procedure involving only the application of boundary conditions that do not involve the beam (similar to Ref. 11). Consequently, we have reduced this linear growth rate problem to an algebraic exercise. As an added feature this procedure will generate the dispersion relation for the system without the beam.

Up to this time all the linear growth rate studies have been valid only for systems that have empty waveguide modes which are TE or TM. In addition to recovering previous results, our method works on systems that have empty waveguide modes which are hybrid. This enables us, for example, to calculate growth rates for waveguides with dielectric liners.

The growth rate formula is derived in Sec. II. The geometry parameters are defined and the special cases of transverse electric and magnetic waves are discussed as well. In Sec. III we recover the results of Sprangle (Ref. 1) and Destler *et al.* (Ref. 2) and discuss the possible need for dielectric liners. Growth rates for a coaxial system with a dielectric liner on the outer wall are derived in Sec. IV. The special cases for TE and TM waves are carefully discussed before the general case is derived. Conclusions are drawn in Sec. V.

II. THE GENERAL GROWTH RATE FORMULA

The linear growth rate problem can roughly be divided into two parts. The first part involves calculating the perturbed sources in terms of the em fields at the equilibrium radius. Because this calculation has essentially been done before (cf. Ref. 1), we only briefly sketch the derivation here. In this sketch we reorganize the equations to better fit the general analysis and emphasize the key points in the derivation.

In the second part we close the system of equations by integrating two components of Ampère's law across the beam. This produces two equations that express the jumps in $c\bar{B}_z$ and $r\partial_r\bar{E}_z$ across the beam in terms of certain beam parameters and the values of $r\partial_r c\bar{B}_z$ and \bar{E}_z at the beam radius. It is at this point that the waveguide geometry first enters into the analysis. The particular boundary conditions at the waveguide walls determine the ratios of $c\bar{B}_z$ and $r\partial_r\bar{E}_z$ to $r\partial_r c\bar{B}_z$ and \bar{E}_z at the beam radius. In fact, the geometry parameters used in the growth rate expression are composed of these ratios. These geometry parameters are generalizations of the (two) normalized wave admittances used by others in the analysis of decoupled systems (see Ref. 3, for example). The generalization is necessary because the usual wave admittances are insufficient for the hybrid case. The reformulation of the em fields in the source-free regions and the incorporation of the geometry parameters are the main new features in this analysis.

A. The perturbed source terms

The type of system we consider has an electron beam propagating in some cylindrical waveguide which is im-

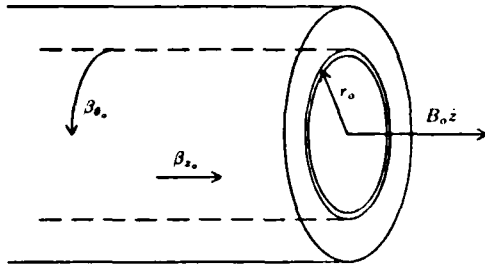


FIG. 1. The equilibrium model.

mersed in a uniform magnetic field $B_0 \hat{z}$ (see Fig. 1). The only restrictions placed on the waveguide are that it must be axisymmetric and invariant to translations in the \hat{z} direction. These restrictions, along with the linearization, allow us to assume that only one harmonic perturbation exists in the system. That is, perturbations with different harmonic numbers do not interact in any way.

We assume that the beam is very thin; its equilibrium density is given by

$$n_0(r) = n_s \delta(r - r_0),$$

where r_0 is the beam radius and n_s is the surface particle density. We also assume that the beam is sufficiently tenuous so that the equilibrium self-fields can be neglected. Each electron moves on a predominantly helical orbit with an unperturbed, normalized velocity of $(0, \beta_\theta, \beta_z)$. This simple distribution enables us to use the single particle equations in our analysis.

The first step is to linearize and Fourier analyze the Lorentz force equation. We write the particle positions as

$$r = r_0 + r_1, \quad \theta = \theta_0 + \Omega_0 t + \theta_1, \quad z = z_0 + v_z t + z_1,$$

where $\Omega_0 = eB_0/(m_0 \gamma_0)$ is the electron-cyclotron frequency and $\gamma_0 m_0 c^2$ is the electron energy. The perturbations r_1 , θ_1 , and z_1 are assumed to be small compared to their zeroth-order counterparts.

We assume that all perturbations have their dependence on the time, t , and the θ and z coordinates defined by $\exp[i(k_z z + l\theta - \omega t)]$. The amplitudes of the perturbations are denoted \bar{r}_1 , $\bar{\theta}_1$, and \bar{z}_1 . Consequently, the linearized, Fourier analyzed version of the total time derivative is $d/dt \rightarrow -i\psi_l$, where

$$\psi_l = \omega - l\Omega_0 - k_z v_z. \quad (1)$$

The quantity ψ_l is a measure of the difference between the actual em wave in the beam-waveguide system and the doppler-shifted cyclotron harmonic. In the following analysis ψ_l plays a very important role. The synchronous limit is defined by $\psi_l \rightarrow 0$. Thus we say that the beam is synchronous with the em wave when ψ_l is small compared to the other frequencies in the analysis ($\psi_l \ll \Omega_0$, in particular). In our derivation we always assume the synchronous limit and only keep the lowest order terms in ψ_l . This assumption has many consequences. Most importantly, it enables us to obtain an explicit growth rate formula. The other consequences will be discussed as they appear. We will show later that the synchronous assumption is a good one for tenuous beams.

The linearized, Fourier-analyzed Lorentz force equation is found to be

$$\bar{r}_1 = (-ie/m_0 \gamma_0 \Omega_0 \psi_l)(\bar{E}_\theta + \beta_z c \bar{B}_r) + O(1), \quad (2a)$$

$$r_0 \bar{\theta}_1 = (-e/m_0 \gamma_0 \psi_l^2)(\beta_\theta^2 \bar{E}_\theta + \beta_\theta \beta_z \bar{E}_z) + O(\psi_l^{-1}), \quad (2b)$$

$$\bar{z}_1 = (e/m_0 \gamma_0 \psi_l^2)[(1 - \beta_z^2) \bar{E}_z - \beta_\theta c \bar{B}_r - \beta_\theta \beta_z \bar{E}_\theta]. \quad (2c)$$

Equation (2) reveals that, to lowest order in ψ_l , the perturbed particle positions depend only on the field components, which are continuous across the beam. This is convenient because the continuous fields are well defined at the beam radius in terms of limiting values as $r \rightarrow r_0$. When $r \neq r_0$, the vacuum equations apply and the continuous fields can be written in terms of \bar{E}_z and $r \partial_r c \bar{B}_z$.

Conservation of electrons on each differential surface element requires that, again to lowest order in ψ_l (cf. Ref. 1),

$$\bar{n}_1 = -in_s(l\bar{\theta}_1 + k_z \bar{z}_1)\delta(r - r_0). \quad (3)$$

From this we find the perturbed current to be (as always, to lowest order in ψ_l)

$$\psi_l^2 \bar{J}_r / \epsilon_0 c = 0, \quad (4a)$$

$$\psi_l^2 \bar{J}_\theta / \epsilon_0 c = -(r_0 \bar{\omega}_b / c)^2 \Omega_0 \times [-i\Omega_* \bar{E}_z^0 + \Omega_0 (r \partial_r c \bar{B}_z)^0] \delta(r - r_0), \quad (4b)$$

$$\frac{\psi_l^2 \bar{J}_z}{\epsilon_0 c} = -\left(\frac{r_0 \bar{\omega}_b}{c}\right)^2 \frac{v_z}{r_0} \times [-i\Omega_* \bar{E}_z^0 + \Omega_0 (r \partial_r c \bar{B}_z)^0] \delta(r - r_0), \quad (4c)$$

where $\bar{\omega}_b^2 = e^2 n_s / (m_0 \gamma_0 r_0 \epsilon_0)$, $\Omega_* = (k_z c - \omega \beta_z)$, and the superscript zeros mean that the function is evaluated at the equilibrium radius r_0 . From Eqs. (3) and (4) we see that, in the synchronous limit, the source perturbations lie on the $r = r_0$ surface. This fact will be important in the next section when we apply the jump conditions.

B. The jump conditions and the geometry parameters

There are two unknowns on the rhs of Eq. (4) and therefore two more equations are needed to close the system. We integrate the Fourier-analyzed θ and z components of Ampère's law across the beam to get

$$c \bar{B}_z \Big|_{r_0^-}^{r_0^+} = - \int_{r_0^-}^{r_0^+} \frac{\bar{J}_\theta(r) dr}{\epsilon_0 c}, \quad (5a)$$

$$c \bar{B}_\theta \Big|_{r_0^-}^{r_0^+} = \int_{r_0^-}^{r_0^+} \frac{r \bar{J}_z(r) dr}{\epsilon_0 c}. \quad (5b)$$

Substituting Eq. (4) into Eq. (5) and rewriting $c \bar{B}_\theta$ in terms of the axial fields gives

$$\psi_l^2 (r \partial_r \bar{E}_z) \Big|_{r_0^-}^{r_0^+} = 2 \frac{v}{\gamma_0} (-i\Omega_*) \times [-i\Omega_* \bar{E}_z^0 + \Omega_0 (r \partial_r c \bar{B}_z)^0], \quad (6a)$$

$$\psi_l^2 (c \bar{B}_z) \Big|_{r_0^-}^{r_0^+} = 2 \frac{v}{\gamma_0} (\Omega_0) [-i\Omega_* \bar{E}_z^0 + \Omega_0 (r \partial_r c \bar{B}_z)^0], \quad (6b)$$

where $v = r_0 e^2 n_s / (2m_0)$ is Budker's parameter. Nothing

more can be done without considering the waveguide geometries.

When $r \neq r_0$ the vacuum waveguide equations apply. In cylindrical coordinates, the general solution is a linear combination of Bessel functions of the first (J_l) and second (Y_l) kinds. We divide the \hat{r} direction into two regions: region I, where $r < r_0$, and region II, where $r > r_0$. Symbolically, we write the axial fields in the two regions as

$$\bar{E}_z = \begin{cases} f_{ee}^-(r)\bar{E}_z^0 + if_{eb}^-(r)(r\partial_r c\bar{B}_z)^0, & r < r_0, \\ f_{ee}^+(r)\bar{E}_z^0 + if_{eb}^+(r)(r\partial_r c\bar{B}_z)^0, & r > r_0, \end{cases} \quad (7)$$

and

$$c\bar{B}_z = \begin{cases} if_{be}^-(r)\bar{E}_z^0 + f_{bb}^-(r)(r\partial_r c\bar{B}_z)^0, & r < r_0, \\ if_{be}^+(r)\bar{E}_z^0 + f_{bb}^+(r)(r\partial_r c\bar{B}_z)^0, & r > r_0. \end{cases} \quad (8)$$

The radial functions $f_{\pm\pm}(r)$ are just linear combinations of J_l and Y_l . Their coefficients are determined by boundary conditions that do not involve the beam. Examples of the calculations of these functions are given in the following two sections.

To proceed with the general calculation, we define

$$g_{bb} = \frac{c\bar{B}_z|_{r_0^+}}{(r\partial_r c\bar{B}_z)^0|_{\bar{E}_z^0=0}} = f_{bb}^+(r_0) - f_{bb}^-(r_0), \quad (9a)$$

$$g_{ee} = \frac{r\partial_r \bar{E}_z|_{r_0^+}}{\bar{E}_z^0|_{(r\partial_r c\bar{B}_z)^0=0}} = r \frac{df_{ee}^+}{dr} \Big|_{r_0} - r \frac{df_{ee}^-}{dr} \Big|_{r_0}, \quad (9b)$$

$$g_{be} = \frac{c\bar{B}_z|_{r_0^+}}{i\bar{E}_z^0|_{(r\partial_r c\bar{B}_z)^0=0}} = f_{be}^+(r_0) - f_{be}^-(r_0), \quad (9c)$$

$$g_{eb} = \frac{r\partial_r \bar{E}_z|_{r_0^+}}{i(r\partial_r c\bar{B}_z)^0|_{\bar{E}_z^0=0}} = r \frac{df_{eb}^+}{dr} \Big|_{r_0} - r \frac{df_{eb}^-}{dr} \Big|_{r_0}, \quad (9d)$$

to be the geometry parameters. We label g_{bb} the TE parameter, g_{ee} the TM parameter, and g_{be} and g_{eb} the hybrid parameters. Plugging Eq. (9) into Eq. (6) yields the dispersion relation

$$\psi_l^2 (g_{bb} g_{ee} + g_{be} g_{eb}) = 2(\nu/\gamma_0) [g_{ee} \Omega_0^2 - (g_{be} + g_{eb}) \Omega_0 \Omega_* - g_{bb} \Omega_*^2] \quad (10)$$

for the beam waveguide system in the synchronous, tenuous beam limit.

When there is no beam, $\nu = 0$, and the empty waveguide dispersion is

$$D_e(\omega, k_z) = g_{bb} g_{ee} + g_{be} g_{eb} = 0. \quad (11)$$

We denote solutions of Eq. (11) by (ω^e, k_z^e) . If, by a suitable choice of system parameters, the perturbed beam frequency $i\Omega_0 + k_z^e v_z$ is equal to some empty waveguide frequency ω^e , we say that the beam perturbation is in resonance with the empty waveguide mode (at k_z^e). Resonant interaction for a simple waveguide geometry is depicted in Fig. 2. We note that, in general, there are two resonant points, if any. The intersection corresponding to k_z^e (k_z^e) is called the high-(low-) frequency intersection point. If $k_z^e < 0$, then the resonance is called a backward wave intersection; otherwise it is

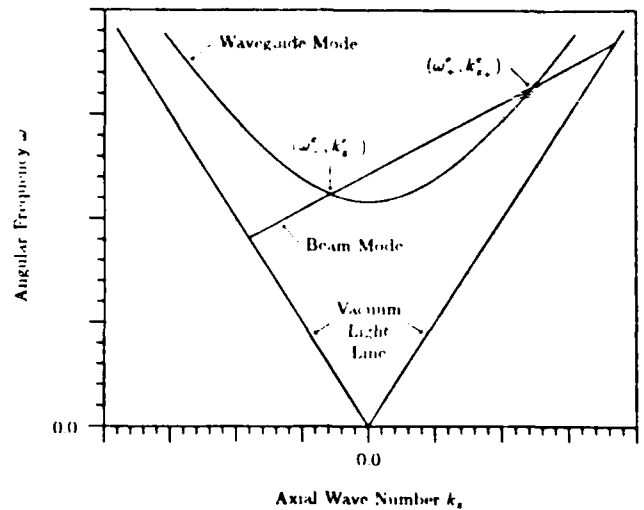


FIG. 2. Graphical description of resonant interaction.

a forward wave intersection ($k_z^e = 0$ is called the cutoff). For a tangential intersection, there is only one resonant point and that point is characterized by identical group velocities for the waveguide and beam modes, i.e., the grazing condition.

C. Properties of the growth rate formula

To keep the analysis consistent, the geometry parameters must also be evaluated to lowest order in ψ_l . Although $D_e(\omega, k_z)$ is usually zeroth order in ψ_l , at resonance it becomes first order. Therefore, at resonance the dispersion relation becomes a cubic in ψ_l instead of a quadratic. In this paper we consider only the resonant case because the cubic growth rate dominates the quadratic growth rate at low densities.

We emphasize that the dispersion function [Eq. (10)] is valid off resonance. Only synchronism is required by the analysis. For example, in the appropriate limit we could show that our growth rate agrees with Uhm's negative mass growth rate in coaxial geometry.¹⁹

At resonance we obtain from Eqs. (10) and (11) that

$$\psi_l^3 = 2 \left(\frac{\nu}{\gamma_0} \right) \frac{g_{ee} \Omega_0^2 - (g_{be} + g_{eb}) \Omega_0 \Omega_* - g_{bb} \Omega_*^2}{(g_{bb} g_{ee} + g_{be} g_{eb})}, \quad (12)$$

where the prime denotes the derivative with respect to ω and the geometry parameters have been evaluated at (ω^e, k_z^e) . We note that the frequency shift ψ_l depends only on ν/γ_0 , the frequencies Ω_0 and Ω_* , and the geometry parameters. We write $\psi_l = \omega_r + i\Gamma$ so that $\Gamma > 0$ represents a growth in beam amplitude with time. Assuming the rhs of Eq. (12) is real, the growth rate and frequency shift are given by

$$\Gamma = (\sqrt{3}/2) |\psi_l|^{1/3}, \quad (13a)$$

$$\omega_r = -\text{sgn}(\psi_l) \Gamma / \sqrt{3}, \quad (13b)$$

where sgn denotes the signum function.

It follows from Eqs. (6) and (9) that the empty waveguide modes are TE or TM if $g_{be} = 0 = g_{eb}$. In this case the empty dispersion relation and corresponding growth rate for a TE mode are

$$g_{\omega\omega} = 0, \quad (14a)$$

$$\frac{\Gamma_{TE}}{\Omega_0} = \frac{\sqrt{3}}{2} \left(\frac{2\nu/\gamma_0}{\Omega_0 g'_{\omega\omega}} \right)^{1/3}. \quad (14b)$$

The corresponding expressions for a TM mode are

$$g_{\omega\omega} = 0, \quad (15a)$$

$$\frac{\Gamma_{TM}}{\Omega_0} = \frac{\sqrt{3}}{2} \left(\frac{2\nu/\gamma_0}{\Omega_0 g'_{\omega\omega}} \right)^{1/3}. \quad (15b)$$

Notice that the TM growth rate depends on Ω_0 , but the TE growth rate depends on Ω_0 . Consequently, if $\Omega_0 = 0$, then the TM modes are stable but the TE modes are still unstable. This can be seen physically by considering a transformation to the beam frame (moving with a velocity v_z with respect to the lab frame). For a TM mode $\Omega_0 = 0$ implies that $\vec{E}_1 = 0$ in the beam frame. Thus $\dot{\gamma}$ is second order and particles do not lose energy in the linear approximation. For a TE mode, however, \vec{E}_0 is finite in the beam frame and $\dot{\gamma}$ remains a first-order term. The simplest way to obtain $\Omega_0 = 0$ is to set $v_z = 0 = k_z$. In the dielectric-free cases, $\Omega_0 = 0$ whenever the grazing condition is satisfied.

Also, notice that $\Gamma \propto n^{1/3}$. This scaling law implies that the synchronous limit is valid for sufficiently tenuous beams. In the next section we use Eqs. (14) and (15) to quickly recover the results of Sprangle and Destler *et al.*

III. DISCUSSION OF PREVIOUS WORK

In this and the next section it is convenient to adopt the standard notation for the cross products of Bessel functions:²⁰

$$P_i(a,b) = J_i(a)Y_i(b) - Y_i(a)J_i(b), \quad (16a)$$

$$Q_i(a,b) = J_i(a)Y'_i(b) - Y_i(a)J'_i(b), \quad (16b)$$

$$R_i(a,b) = J'_i(a)Y_i(b) - Y'_i(a)J_i(b), \quad (16c)$$

$$S_i(a,b) = J'_i(a)Y'_i(b) - Y'_i(a)J'_i(b). \quad (16d)$$

It is simple to show from Bessel's equation that, if $a = a(z)$ and $b = b(z)$, then

$$P'_i(a,b) = a'R_i + b'Q_i, \quad (17a)$$

$$Q'_i(a,b) = a'S_i + b'[(l^2/b^2 - 1)P_i - (1/b)Q_i], \quad (17b)$$

$$R'_i(a,b) = a'[(l^2/a^2 - 1)P_i - (1/a)R_i] + b'S_i, \quad (17c)$$

$$S'_i(a,b) = a'[(l^2/a^2 - 1)Q_i - (1/a)S_i] + b'[(l^2/b^2 - 1)R_i - (1/b)S_i]. \quad (17d)$$

Clever choices for arguments of these cross products simplify the algebra tremendously.

Consider the case of only a smooth outer conducting wall of radius r_w (see Fig. 3). We apply the usual boundary conditions at r_w and growth conditions at $r = 0$ and make the following identifications [via Eqs. (7) and (8)]:

$$f_{\omega}^- = \frac{J_l(x)}{J_l(x_w)}, \quad f_{\omega}^+ = \frac{P_l(x, x_w)}{P_l(x_0, x_w)},$$

$$f_{\omega\omega}^- = \frac{J_l(x)}{x_0 J'_l(x_0)}, \quad f_{\omega\omega}^+ = \frac{Q_l(x, x_w)}{x_0 S_l(x_0, x_w)},$$

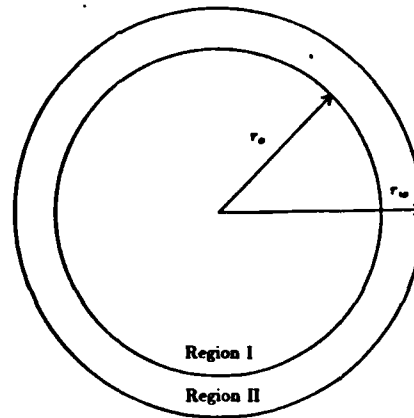


FIG. 3. Cross section of the simple cylindrical waveguide geometry.

and

$$f_{\omega\omega}^- \equiv f_{\omega\omega}^+ \equiv 0 \equiv f_{\omega\omega}^- \equiv f_{\omega\omega}^+,$$

for $\xi^2 = (\omega/c)^2 - k_z^2$, $x(r) = r\xi$, and $x_0 = x(r_0)$, etc. From Eq. (9) the TE and TM geometry parameters are found to be

$$g_{\omega\omega} = \frac{2}{\pi} \frac{J'_l(x_w)}{x_0^2 J'_l(x_0) S_l(x_0, x_w)}$$

and

$$g_{\omega\omega} = -\frac{2}{\pi} \frac{J_l(x_w)}{J_l(x_0) P_l(x_0, x_w)}.$$

As expected, the TE solutions are characterized by $J'_l(x_w) = 0$ and the TM solutions are characterized by $J_l(x_w) = 0$. The growth rates are found from Eqs. (14) and (15) to be

$$\frac{\Gamma_{TE}}{\Omega_0} = \frac{\sqrt{3}}{2} \left(2 \frac{\nu}{\gamma_0} \frac{(c/r_w)^2}{\Omega_0 \omega} \right)^{1/3} \times \left| \frac{x_0 J'_l(x_0)}{[1 - (l/x_w)^2]^{1/2} J_l(x_w)} \right|^{2/3}$$

and

$$\frac{\Gamma_{TM}}{\Omega_0} = \frac{\sqrt{3}}{2} \left(2 \frac{\nu}{\gamma_0} \frac{(c/r_w)^2}{\Omega_0 \omega} \right)^{1/3} \left| \frac{J_l(x_0)}{J'_l(x_w)} \right|^{2/3}.$$

These results do indeed agree with Sprangle's synchronous case (Ref. 1).

When a smooth inner conductor of radius r_i is added to the system (see Fig. 4), only the boundary conditions in the region below the beam are affected. The net difference is in the two functions f_{ω}^- and $f_{\omega\omega}^-$, which become

$$f_{\omega}^- = P_l(x, x_i)/P_l(x_0, x_i)$$

and

$$f_{\omega\omega}^- = Q_l(x, x_i)/x_0 S_l(x_0, x_i)$$

for the inner conductor case. The geometry parameters become

$$g_{\omega\omega} = \frac{2}{\pi} \frac{S_l(x_w, x_i)}{x_0^2 S_l(x_0, x_i) S_l(x_0, x_w)}$$

and

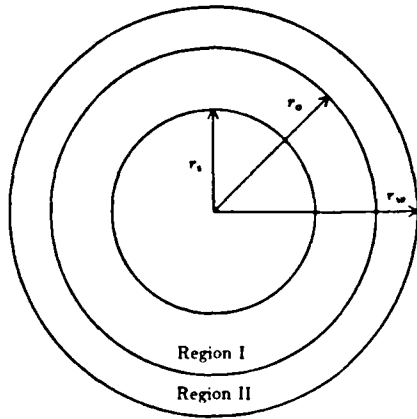


FIG. 4. Cross section of the coaxial waveguide geometry.

$$g_{ee} = -\frac{2}{\pi} \frac{P_l(x_w, x_i)}{P_l(x_0, x_i)P_l(x_0, x_w)}$$

so that TE solutions are characterized by $S_l(x_w, x_i) = 0$ and TM solutions by $P_l(x_w, x_i) = 0$. The TE and TM growth rates are found from Eqs. (14) and (15) to be

$$\frac{\Gamma_{TE}}{\Omega_0} = \frac{\sqrt{3}}{2} \left(2 \frac{v}{\gamma_0} \frac{(c/r_w)^2}{\Omega_0 \omega} \right)^{1/3} \times \left| \frac{(\pi/2)x_w x_0^2 S_l(x_0, x_i) S_l(x_0, x_w)}{dS_l(x_w, x_i)/dx_w} \right|^{1/3},$$

$$\frac{\Gamma_{TM}}{\Omega_*} = \frac{\sqrt{3}}{2} \left(2 \frac{v}{\gamma_0} \frac{(c/r_w)^2}{\Omega_* \omega} \right)^{1/3} \times \left| \frac{(\pi/2)x_w P_l(x_0, x_i) P_l(x_0, x_w)}{dP_l(x_w, x_i)/dx_w} \right|^{1/3},$$

where Eq. (17) is used to compute the derivatives.

These results agree with Destler (Ref. 2) except for an amplitude factor. As pointed out by Destler *et al.*, the discrepancy comes from the method of calculating the perturbed charge density. There is strong evidence pointing to the correctness of our results. First, it was already pointed out here that our results agree with Uhm's kinetic theory approach in the proper limit. Furthermore, a fluid analysis done by our group²¹ has recovered the dispersion relation Eq. (10) in the infinitesimal E layer limit (at least when $g_{eb} = 0 = g_{eb}$).

In both the cases with and without an inner conductor, if resonance is possible then the resonant wavenumbers are given by

$$(ck_z)_\pm = \gamma_{z_0}^2 l \Omega_0 \beta_{z_0} \pm \gamma_{z_0} [(\gamma_{z_0} l \Omega_0)^2 - (\xi c)^2]^{1/2} \quad (18)$$

for $\gamma_{z_0}^{-2} = 1 - \beta_{z_0}^2$. The condition for resonance can be written

$$\frac{r_0}{r_w} < \frac{l}{x_w} \frac{\gamma_0 \beta_0}{[1 + (\gamma_0 \beta_0)^2]^{1/2}} \quad (19)$$

At high azimuthal harmonics, the peak E_θ field is very close to the wall. Thus in order to get reasonable growth rates, it is necessary to make the ratio r_0/r_w as large as possible. For all possible TE or TM solutions of either case, it is always true that $l < x_w$. Since $\beta_{z_0} < 1$, r_0/r_w must be very small unless the

beam energy is large. Consequently, we do not expect low-energy systems to be very successful in these simple geometries.

For low-energy systems something must be done to (in essence) raise the possible values of l/x_w . This is just another way of saying that something is needed to "slow down" the em wave. One possibility is the slotted wall structure. This method has received considerable attention and will not be discussed here. Another possible method involves the insertion of a dielectric liner. This approach is studied in detail in the next section.

IV. THE DIELECTRIC LINER

Consider the system shown in Fig. 5. It is similar to the coaxial system except that a dielectric liner of relative permittivity ϵ_r occupies the space between $r = r_d$ and $r = r_w$. As before, the beam radius is r_0 and the inner and outer wall radii are r_i and r_w , respectively. There is no fundamental difference between this system and one without an inner conductor. In fact, the results are virtually identical until the inner radius becomes relatively large. However, the dispersion relation for the coaxial dielectric liner case takes on a more symmetric form and is easier to solve numerically. For these reasons we present the details of the calculation for the coaxial case. Afterward, we present the results for the special case $r_i = 0$.

The procedure for obtaining the geometry parameters is still straightforward, but now the algebra is more complicated. Also, the results are harder to analyze. First, the modes only decouple into TE and TM modes at isolated points. Second, the dispersion curves are no longer simple hyperbolas in $\omega - k_z$ space. Finally, the arguments of some of the Bessel functions become imaginary in part of the $\omega - k_z$ plane.

In Sec. IV A, we derive the geometry parameters and the empty waveguide dispersion relation. In Sec. IV B, we discuss in detail the special cases where the modes are either TE or TM. We present the general result and apply it to both a high-energy and a low-energy system in Sec. IV C.

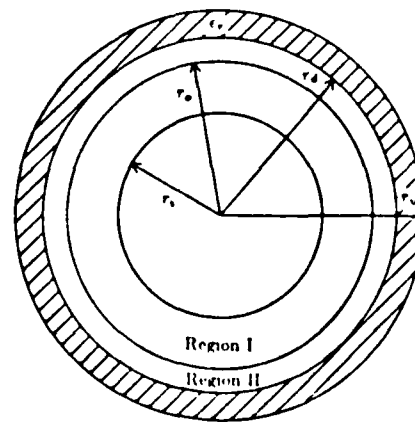


FIG. 5. Cross section of a coaxial system with a dielectric liner.

A. The empty waveguide dispersion relation

In anticipation of the results to come, we define

$$\xi_A^2 = (\omega/c)^2 - k_z^2, \quad (20a)$$

$$\xi_B^2 = \epsilon_r(\omega/c)^2 - k_z^2, \quad (20b)$$

and

$$\Psi_c = l(\omega k_z/c)(\epsilon_r - 1)/\xi_B^2. \quad (21)$$

We also define five sets of cross products:

$$\Phi_1(r) = \Phi_l(x, x_i), \quad \hat{\Phi}_1 = \Phi_1(r_0), \quad (22a)$$

$$\Phi_2(r) = \Phi_l(x, x_d), \quad \hat{\Phi}_2 = \Phi_2(r_0), \quad (22b)$$

$$\Phi_3(r) = \Phi_l(x, x_0), \quad \hat{\Phi}_3 = \Phi_3(r_d), \quad (22c)$$

$$\hat{\Phi}_4 = \Phi_l(x_d, x_i), \quad (22d)$$

$$\Phi_5(r) = \Phi_l(y, y_w), \quad \hat{\Phi}_5 = \Phi_5(r_d), \quad (22e)$$

for $\Phi = P, Q, R,$ and S ; for $x = r\xi_A, y = r\xi_B,$ and $y_d = r_d\xi_B,$ etc. Finally, we define some more general cross products:

$$\kappa^{i,j} = x_d(\epsilon_r \hat{P}_i \hat{R}_j - \hat{P}_j \hat{R}_i), \quad (23a)$$

$$\chi^{i,j} = x_d(\hat{Q}_i \hat{S}_j - \hat{Q}_j \hat{S}_i), \quad (23b)$$

$$\tau^{i,j} = \Psi_c \hat{P}_i \hat{Q}_j, \quad (23c)$$

$$\eta^{i,j} = \kappa^{i,j} \chi^{i,j} - \tau^{i,j} \tau^{j,i}, \quad (23d)$$

for $\xi = \xi_A/\xi_B.$

Now we must divide the r coordinate space into three regions. We write the axial fields symbolically in these regions as

$$\tilde{E}_z = \begin{cases} f_{ee}^-(r) \tilde{E}_z^0 + if_{eb}^-(r) (r \partial_r c \tilde{B}_z)^0, & r_i < r < r_0, \\ f_{ee}^+(r) \tilde{E}_z^0 + if_{eb}^+(r) (r \partial_r c \tilde{B}_z)^0, & r_0 < r < r_d, \\ f_{ee}^*(r) \tilde{E}_z^0 + if_{eb}^*(r) (r \partial_r c \tilde{B}_z)^0, & r_d < r < r_w, \end{cases} \quad (24)$$

and

$$c \tilde{B}_z = \begin{cases} if_{be}^-(r) \tilde{E}_z^0 + f_{bb}^-(r) (r \partial_r c \tilde{B}_z)^0, & r_i < r < r_0, \\ if_{be}^+(r) \tilde{E}_z^0 + f_{bb}^+(r) (r \partial_r c \tilde{B}_z)^0, & r_0 < r < r_d, \\ if_{be}^*(r) \tilde{E}_z^0 + f_{bb}^*(r) (r \partial_r c \tilde{B}_z)^0, & r_d < r < r_w. \end{cases} \quad (25)$$

We then systematically apply all the boundary conditions that do not involve the beam in order to identify the 12 functions defined above. In addition to the usual boundary conditions at $r_i, r_0,$ and $r_w,$ there are six boundary conditions at $r_d.$ The interesting boundary condition is

$$E_r|_{r_d} = \epsilon_r E_r|_{r_d};$$

the other five reflect the continuous nature of the remaining field components. Two of the boundary conditions are redundant. The remaining four enable the task of finding the 12 functions to be completed. The results are

$$f_{eb}^-(r) = 0, \quad f_{be}^-(r) = 0,$$

$$f_{ee}^-(r) = P_1(r)/\hat{P}_1, \quad f_{bb}^-(r) = Q_1(r)/x_0 \hat{S}_1,$$

$$f_{eb}^+(r) = \frac{2}{\pi} \frac{r^{3.5}}{x_0 \eta^{3.5}} P_3(r), \quad f_{be}^+(r) = -\frac{2}{\pi} \frac{r^{5.5}}{\eta^{3.5}} Q_3(r),$$

$$f_{ee}^*(r) = \frac{1}{\hat{P}_3} \left(\frac{2}{\pi} \frac{\hat{P}_3 \chi^{3.5}}{\eta^{3.5}} P_3(r) - P_2(r) \right),$$

$$f_{bb}^*(r) = \frac{1}{x_0 \hat{Q}_3} \left(\frac{2}{\pi} \frac{\hat{Q}_3 \kappa^{3.5}}{\eta^{3.5}} Q_3(r) - P_2(r) \right).$$

$$f_{eb}^*(r) = \frac{2}{\pi} \frac{r^{3.5}}{x_0 \eta^{3.5}} P_3(r), \quad f_{be}^*(r) = -\frac{2}{\pi} \frac{r^{5.5}}{\eta^{3.5}} Q_3(r),$$

$$f_{ee}^*(r) = \frac{2}{\pi} \frac{\chi^{3.5}}{\eta^{3.5}} P_3(r), \quad f_{bb}^*(r) = \frac{2}{\pi} \frac{\kappa^{3.5}}{x_0 \eta^{3.5}} Q_3(r).$$

Given the field functions, the geometry parameters are found from Eq. (9) to be

$$g_{bb} = \left(\frac{2}{\pi} \right)^2 \frac{\hat{Q}_3 \kappa^{3.5}}{x_0^2 \hat{Q}_3 \eta^{3.5}} + \frac{\hat{P}_3}{x_0 \hat{Q}_3} - \frac{\hat{Q}_1}{x_0 \hat{S}_1}, \quad (26a)$$

$$g_{ee} = - \left(\frac{2}{\pi} \right)^2 \frac{\hat{P}_3 \chi^{3.5}}{\hat{P}_3 \eta^{3.5}} + \frac{x_0 \hat{Q}_3}{\hat{P}_3} - \frac{x_0 \hat{R}_1}{\hat{P}_1}, \quad (26b)$$

$$g_{eb} = g_{be} = - \left(\frac{2}{\pi} \right)^2 \frac{r^{5.5}}{x_0 \eta^{3.5}}. \quad (26c)$$

We note that the dielectric empty waveguide modes decouple into TE and TM modes if $r^{5.5} = 0.$

Two equivalent forms of the empty waveguide dispersion relation will be used in this section. The first comes from applying the definition [Eq. (11)]

$$\left[\frac{\hat{P}_3}{\hat{Q}_3} - \frac{\hat{Q}_1}{\hat{S}_1} + \left(\frac{2}{\pi} \right)^2 \frac{\hat{Q}_3 \kappa^{3.5}}{x_0 \hat{Q}_3 \eta^{3.5}} \right] \left[\frac{\hat{Q}_3}{\hat{P}_3} - \frac{\hat{R}_1}{\hat{P}_1} - \left(\frac{2}{\pi} \right)^2 \frac{\hat{P}_3 \chi^{3.5}}{x_0 \hat{P}_3 \eta^{3.5}} \right] + \left[\left(\frac{2}{\pi} \right)^2 \frac{r^{5.5}}{x_0 \eta^{3.5}} \right]^2 = 0.$$

The numerator of this relation appears to depend on the beam radius $r_0.$ It should not, because r_0 has no physical significance when there is no beam and thus cannot affect the zeros of the dispersion relation. After more algebra, the dispersion relation can be written so that the numerator is independent of $r_0:$

$$D_e(\omega, k_z) = \frac{-\eta^{4.5}}{(\pi/2)^2 x_0^2 \hat{P}_1 \hat{S}_1 \eta^{3.5}} = 0. \quad (27)$$

Thus empty waveguide solutions are characterized by $\eta^{4.5} = 0.$

A typical dispersion plot is shown in Fig. 6. The cutoff line is defined by $k_z = 0.$ The vacuum and dielectric light

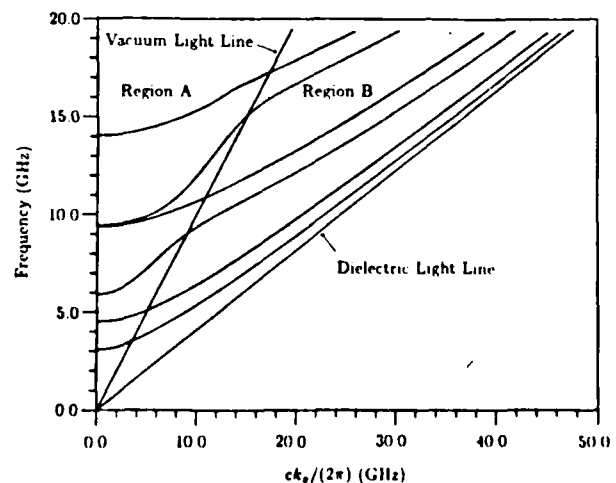


FIG. 6. Typical dispersion plot for a dielectric system. Parameters: $l = 7,$ $r_i = 0.055$ m, $r_d = 0.065$ m, $r_w = 0.075$ m, and $\epsilon_r = 6.0.$

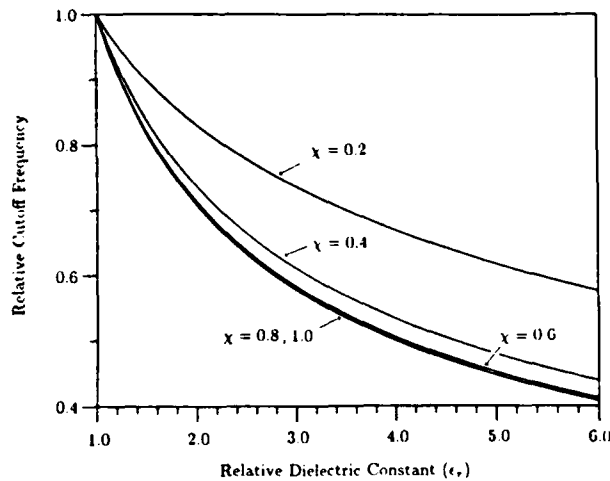


FIG. 7. The effect of liner thickness on the cutoff frequency of the first radial mode. Parameters: $l = 7$, $r_i = 0.025$ m, $r_w = 0.075$ m. The measure of liner thickness is $\chi = (r_w - r_d)/(r_w - r_i)$.

lines are defined by $\omega/(ck_z) = 1$ and $\omega/(ck_z) = \epsilon_r^{-1/2}$, respectively. We denote the region in $\omega - k_z$ space between the cutoff line and the vacuum light line as region A. The region between the vacuum and dielectric light lines is denoted region B. In region A, ξ_A and ξ_B are both real. In region B, ξ_B is still real but ξ_A is purely imaginary and Φ_1 through Φ_4 are given in terms of modified Bessel functions. Fortunately, the geometry parameters are still real, so the growth rate equation [Eq. (13)] is still valid for resonant points in region B.

The dielectric has two major effects on the dispersion curves. First, the cutoff points are lowered (in frequency). Figure 7 shows the relative cutoff frequency for the lowest dispersion curve versus the relative permittivity for several liner thicknesses. The figure reveals that the relative cutoff rapidly approaches $\epsilon_r^{-1/2}$ as the thickness increases. Second, the dispersion curves are asymptotic to the dielectric light line. This feature is more important for linearly streaming beams ($l = 0$) where the beam line is always below the vacuum light line. Depression of the cutoff frequency is more important for the cases of interest in this paper ($l \neq 0$).

B. The special cases of TE and TM modes

From the definition of $r^{(j)}$ [Eq. (23)], we see that the modes will be TE or TM if $\Psi_c = 0$, $\hat{Q}_3 = 0$, or $\hat{P}_3 = 0$. Equation (21) reveals that there are three ways to have $\Psi_c = 0$. If $\epsilon_r = 1$, we are obviously back to the coaxial case without a dielectric. The second possibility is $l = 0$. The theory for this case has been considered elsewhere and successful experiments have been performed by J. Walsh *et al.*²² at Dartmouth.

The final possibility is $k_z = 0$. At cutoff, $\xi_B = \sqrt{\epsilon_r} \xi_A$ and $\eta^{4.5} = \kappa^{4.5} \chi^{4.5}$. The TE result is specified by $g_{bb} = 0$, which is equivalent to $\chi^{4.5} = 0$. As in the case without a dielectric, only $c\bar{B}_z$, \bar{E}_r , and \bar{E}_θ are nonzero at this cutoff point. The TM result is given either by $g_{rr} = 0$ or $\kappa^{4.5} = 0$. At

the TM cutoff point, only \bar{E}_z , $c\bar{B}_r$, and $c\bar{B}_\theta$ are nonzero.

At a point where $\hat{Q}_3 = 0$,

$$g_{bb} = \frac{-(2/\pi)\hat{Q}_4}{x_0^2 \hat{Q}_3 \hat{S}_1}$$

Thus the resulting TE mode is characterized by

$$\hat{Q}_4(x_0) = 0 = \hat{Q}_3(y_w). \quad (28)$$

This TE mode has $c\bar{B}_z(r_d) = 0$. Consequently, $\bar{E}_r(r_d) = 0$ and so \bar{E}_r is continuous at r_d . The growth rate is found from Eq. (14):

$$\frac{\Gamma_{TE}}{\Omega_0} = \frac{\sqrt{3}}{2} \left(2 \frac{v}{\gamma_0} \frac{(c/r_0)^2}{\Omega_0 \omega} \right)^{1/3} \left| \frac{(\pi/2)x_0^3 \hat{Q}_3 \hat{S}_1}{d\hat{Q}_4/dx_0} \right|^{1/3}$$

When $\hat{P}_3 = 0$,

$$g_{rr} = (2/\pi) \hat{P}_4 / \hat{P}_1 \hat{P}_3$$

and a TM mode has

$$\hat{P}_4(x_0) = 0 = \hat{P}_3(y_w). \quad (29)$$

The TM mode is characterized by $\bar{E}_z(r_d) = 0$, almost as though there were a conducting wall at r_d . The growth rate is given by

$$\frac{\Gamma_{TM}}{\Omega_*} = \frac{\sqrt{3}}{2} \left(2 \frac{v}{\gamma_0} \frac{(c/r_0)^2}{\Omega_* \omega} \right)^{1/3} \left| \frac{(\pi/2)x_0 \hat{P}_1 \hat{P}_3}{d\hat{P}_4/dx_0} \right|^{1/3}$$

It is known²³ that the zeros of $\hat{P}_4(x_0)$ are all real, so these TM modes can only exist in region A. Also, we can show that $\hat{Q}_4(x_0)$ has no purely imaginary zeros so the TE modes all lie in region A as well. A dispersion plot highlighting the TE and TM points is shown in Fig. 8. Let (ξ_A, ξ_B) represent any solution of either Eq. (28) or Eq. (29). If $\xi_B > \sqrt{\epsilon_r} \xi_A$, then the pair (ξ_A, ξ_B) corresponds to the solution of the dispersion relation that has

$$\omega = c[(\xi_B^2 - \xi_A^2)/(\epsilon_r - 1)]^{1/2}$$

and

$$ck_z = c[(\xi_B^2 - \epsilon_r \xi_A^2)/(\epsilon_r - 1)]^{1/2}.$$

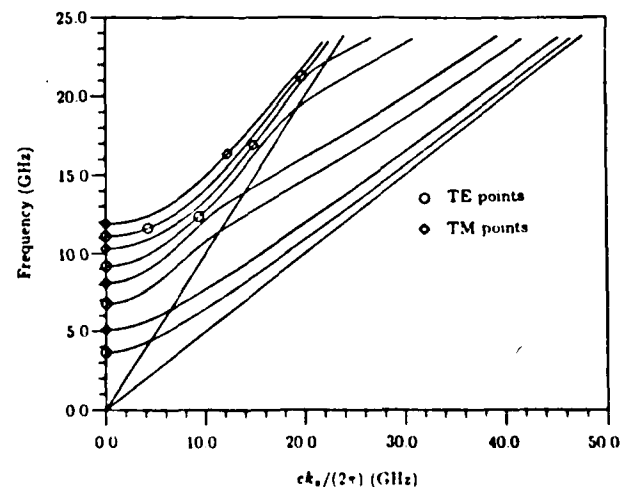


FIG. 8. A dispersion plot revealing the locations of the TE and TM points. Parameters: $l = 7$, $r_i = 0.020$ m, $r_d = 0.065$ m, $r_w = 0.075$ m, and $\epsilon_r = 4.0$.

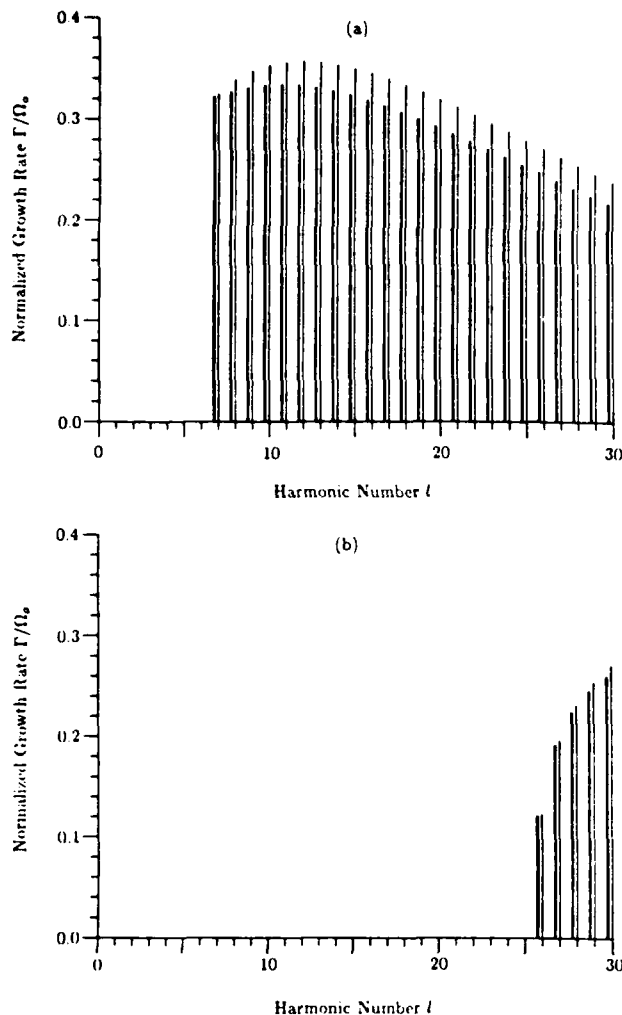


FIG. 9. The linear growth rate curves for a high-energy beam in the simple waveguide geometry: (a) the lowest TE mode, (b) the lowest TM mode. The thin line represents the low-frequency intersection and the thick line represents the high-frequency intersection. Parameters: $n_s = 10^{14} \text{ m}^{-2}$, $\beta_{e0} = 0.935$, $\beta_{z0} = 0.305$, $r_0 = 0.06 \text{ m}$, and $r_w = 0.075 \text{ m}$.

Furthermore, if $\hat{\xi}_B$ represents any other solution [of $\hat{P}_3(y_w) = 0$ or $\hat{Q}_3(y_w) = 0$, whichever is appropriate] and $\hat{\xi}_B > \xi_B$, then $(\hat{\xi}_A, \hat{\xi}_B)$ also corresponds to a solution of the dispersion relation.

C. The general result

The calculation of the derivative of the empty waveguide dispersion relation is straightforward but tedious. The final expression is quite lengthy and is not presented here. For our purposes it is sufficient to write

$$(g_{bb} g_{ee} + g_{be} g_{eb})' = \frac{-(\eta^{4.5})'}{(\pi/2)^2 x_0^2 P_1 S_1 \eta^{1.5}}, \quad (30)$$

when $\eta^{4.5} = 0$. Once again the prime denotes the derivative with respect to ω .

The solution for the case of $r_s = 0$ can be found by following the same procedure outlined above. The solution can

be written in the same form, provided that the following substitutions are made:

$$\begin{aligned} \hat{P}_1, \hat{Q}_1 &\rightarrow J_l(x_0), & \hat{R}_1, \hat{S}_1 &\rightarrow J_l'(x_0), \\ \hat{P}_4, \hat{Q}_4 &\rightarrow J_l(x_d), & \hat{R}_4, \hat{S}_4 &\rightarrow J_l'(x_d). \end{aligned}$$

In the following, we present results both for $r_s = 0$ and $r_s > 0$.

The first example is for a high-energy beam. The parameters for this example are $\beta_{e0} = 0.935$, $\gamma_0 = 5.46$, $r_s = 0$, and $r_0/r_w = 0.8$. A plot of growth rate versus harmonic number is shown in Fig. 9 for the lowest two dispersion curves when there is no liner. Without a dielectric liner there is resonant interaction starting with $l = 7$.

Figure 10 shows the growth rates for the system when a 1 cm thick dielectric liner with a relative permittivity of 2.3 is placed against the outer wall. Although nothing drastic happens, there are some noticeable differences between the two systems. For the dielectric case, there is resonant interaction starting with $l = 4$. Also, the dielectric liner reduces the ini-

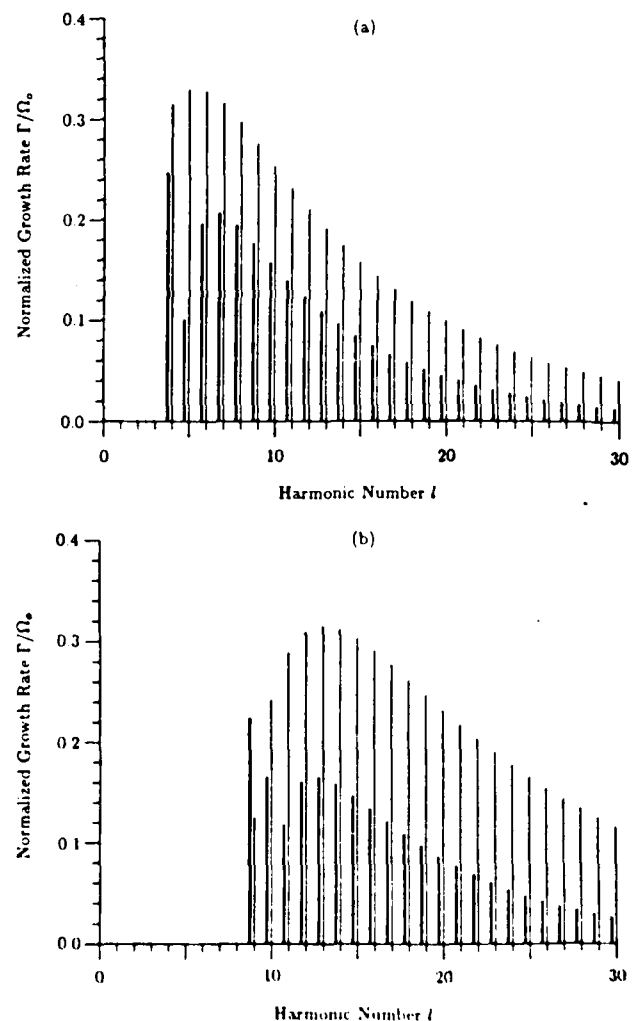


FIG. 10. The linear growth rate curves for a high-energy beam in a dielectric-lined waveguide: (a) the first radial mode, (b) the second radial mode. Parameters: $n_s = 10^{14} \text{ m}^{-2}$, $\beta_{e0} = 0.935$, $\beta_{z0} = 0.305$, $r_0 = 0.06 \text{ m}$, $r_s = 0.0$ m, $r_d = 0.065 \text{ m}$, $r_w = 0.075 \text{ m}$, and $\epsilon_r = 2.3$.

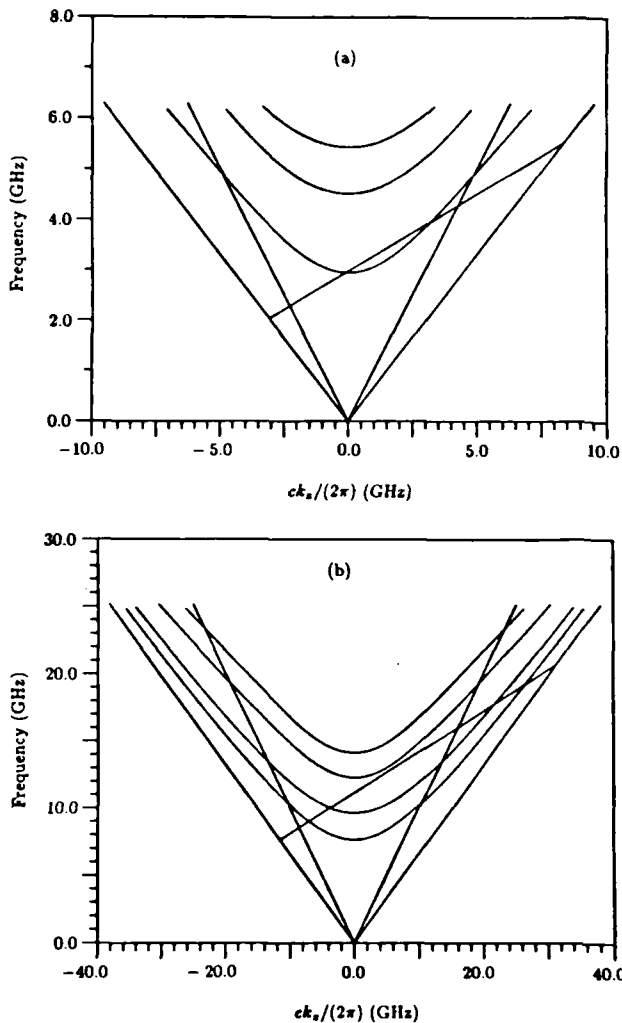


FIG. 11. The dispersion curves for a high-energy beam in a dielectric-lined waveguide: (a) $l = 4$, (b) $l = 15$. Parameters: $\beta_{e0} = 0.935$, $\beta_{e2} = 0.305$, $r_0 = 0.06$ m, $r_1 = 0.0$ m, $r_d = 0.065$ m, $r_w = 0.075$ m, and $\epsilon_r = 2.3$.

tial harmonic for the second radial mode from $l = 26$ to $l = 9$. Furthermore, there is a dip in the forward wave growth rate at $l = 5$ for the lowest curve and $l = 11$ for the second curve. These dips correspond to the places where the resonant points "cross over" the vacuum light line. For the dielectric-free case, the growth rates for the forward and backward waves are comparable. However, in the dielectric case, the forward wave growth rates are often much smaller than the corresponding backward wave, especially when the resonant intersection is in region B.

The dispersion curves for the fourth and twentieth harmonics are plotted in Fig. 11; the beam lines are also plotted. The dispersion curves that produce resonant intersections appear to be approximately hyperbolas asymptotic to the dielectric light line. The E_θ fields are plotted in Fig. 12 for the backward wave intersection when $l = 4$ and for the second forward wave intersection when $l = 20$. It is typical that the field is relatively large at the beam location when the intersection occurs in region A. Likewise, when the intersection is in region B, the bulk of the field is in the dielectric. If one

desires to operate at a point in region B, the beam must be placed very close to the dielectric wall.

The effect of the dielectric is more pronounced in our second example. For this system, we have a low-energy beam ($\gamma_0 = 1.033$) with $\beta_{e0} = 0.23$, $r_1/r_w = 0.2$, and $r_0/r_w = 0.3$. By plugging these numbers into Eq. (19), we see that there can be no resonant interaction for any l unless $r_0/r_w < 0.231$ (without some slow wave structure). Thus for this example there is no resonant growth at all without a dielectric liner.

When we add a dielectric liner with a thickness of 3.0 cm and $\epsilon_r = 2.3$, we get resonant interaction starting with $l = 11$. The resonant growth rate curve is plotted in Fig. 13. The growth rate decreases much more rapidly with increasing l than the previous case did. Whereas we might expect the first example to multimode, the low-energy example is likely to operate only at the lowest harmonic. The dispersion curves and beam line for the $l = 11$ case are plotted in Fig. 14. We see that the only two intersections are both forward waves and the system is relatively close to a tangential intersection point. Again the dispersion curves are essentially hyperbolas asymptotic to the dielectric light line.

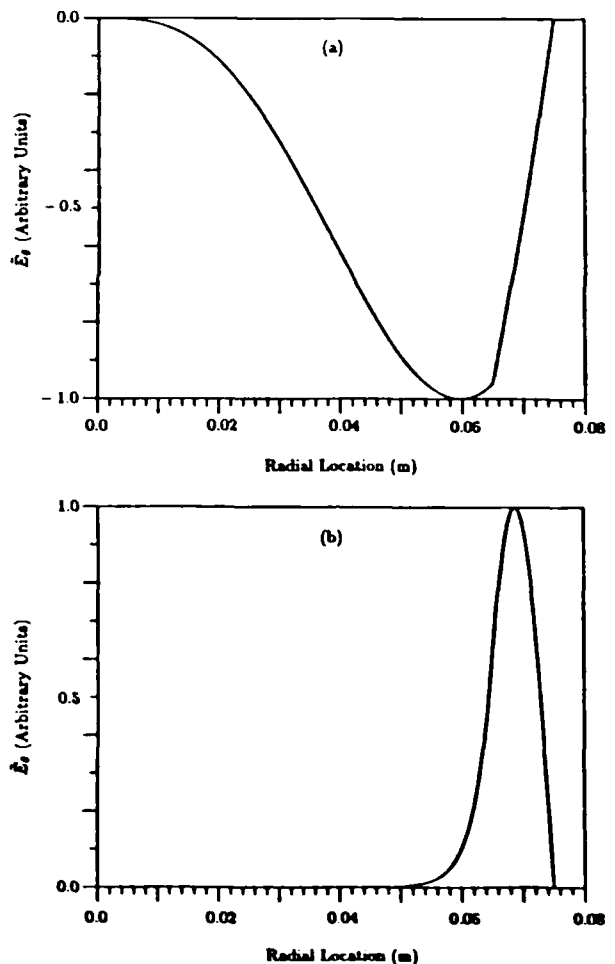


FIG. 12. The empty waveguide E_θ profile for: (a) the $l = 4$ backward wave intersection ($f = 2.94$ GHz, $\lambda_c = 2.98$ m), (b) the $l = 15$ forward wave intersection with the second radial mode ($f = 17.8$ GHz, $\lambda_c = 0.014$ m). Parameters: $\beta_{e0} = 0.935$, $\beta_{e2} = 0.305$, $r_0 = 0.06$ m, $r_1 = 0.0$ m, $r_d = 0.065$ m, $r_w = 0.075$ m, and $\epsilon_r = 2.3$.

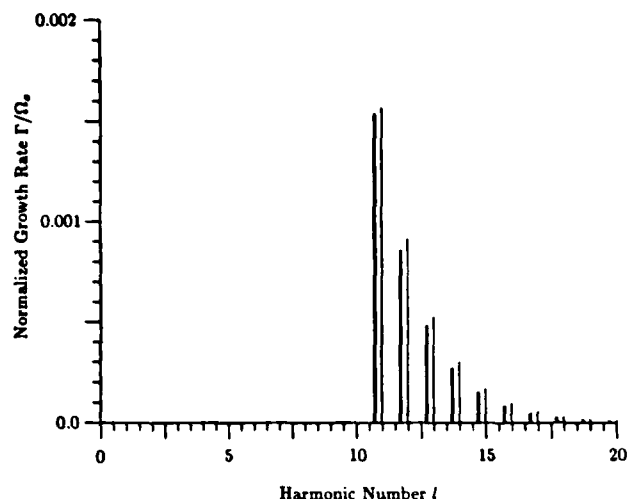


FIG. 13. The linear growth rate curves for a low-energy beam in a dielectric-lined coaxial waveguide. Parameters: $n_i = 10^{14} \text{ m}^{-2}$, $\beta_{\theta_0} = 0.23$, $\beta_{\phi_0} = 0.10$, $r_0 = 0.015 \text{ m}$, $r_i = 0.01 \text{ m}$, $r_d = 0.02 \text{ m}$, $r_w = 0.05 \text{ m}$, and $\epsilon_r = 2.3$.

V. SUMMARY

We have developed a powerful procedure for calculating the linear growth rates of a particular class of beam-waveguide systems. The method easily recovers previous results and can also handle systems with hybrid empty waveguide modes. Using this method we have derived many properties of waveguide systems with dielectric liners. We have demonstrated the usefulness of such liners in low-energy systems.

Some of the effects neglected by our idealized, zero thickness beam analysis should be pointed out. In high harmonic systems with finite thickness beams, betatron oscillations and frequency (Ω_0) spread may reduce the growth rates considerably. Also, dielectric losses were neglected in our analysis. The stabilization of the negative mass instability by lossy dielectrics has been examined previously by Briggs and Neil.²⁴ These nonideal effects should be carefully estimated before any particular dielectric, large orbit device is constructed.

This general procedure can be applied to many more systems than the ones described in this paper. Although the model assumed azimuthal symmetry, the method can actually accommodate systems with periodic boundary conditions in the θ direction. For example, the method can be applied to the popular vane-type resonator system.²⁵ This type of application will be discussed in detail in a future paper.

ACKNOWLEDGMENTS

We would like to thank Dr. F. W. G. Olver for his invaluable suggestions concerning the properties of Bessel functions. We are also grateful to R. Kulkarni and D. Welsh for many helpful discussions. Finally, we appreciate the ef-

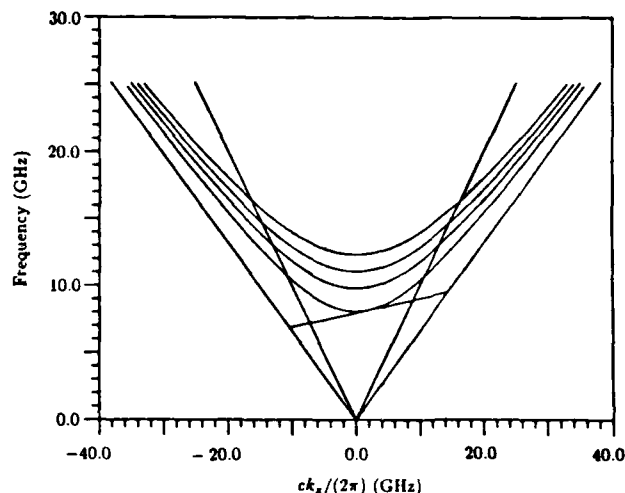


FIG. 14. The dispersion curves for a low-energy beam in a dielectric-lined coaxial waveguide. Parameters: $\beta_{\theta_0} = 0.23$, $\beta_{\phi_0} = 0.10$, $r_0 = 0.015 \text{ m}$, $r_i = 0.01 \text{ m}$, $r_d = 0.02 \text{ m}$, $r_w = 0.05 \text{ m}$, $l = 11$, and $\epsilon_r = 2.3$.

forts of S. Swanekamp in the preparation of the field plots.

This work was supported by the Air Force Office of Scientific Research and the University of Maryland Computer Science Center.

- ¹P. Sprangle, *J. Appl. Phys.* **47**, 2935 (1976).
- ²W. W. Destler, H. Romero, C. D. Striffler, R. L. Weiler, and W. Namkung, *J. Appl. Phys.* **52**, 2740 (1981).
- ³R. J. Briggs and V. K. Neil, *J. Nucl. Energy Part C* **9**, 209 (1967).
- ⁴W. W. Destler, D. W. Hudgings, M. J. Rhee, S. Kawasaki, and V. L. Granatstein, *J. Appl. Phys.* **48**, 3291 (1977).
- ⁵H. S. Uhm and R. C. Davidson, *J. Appl. Phys.* **49**, 593 (1978).
- ⁶Y. Goren, H. S. Uhm, and R. C. Davidson, *J. Appl. Phys.* **49**, 3789 (1978).
- ⁷Y. Y. Lau and L. R. Barnett, *Int. J. Infrared Millimeter Waves* **3**, 619 (1982).
- ⁸W. W. Destler, R. Kulkarni, C. D. Striffler, and R. L. Weiler, *J. Appl. Phys.* **54**, 4152 (1983).
- ⁹C. D. Striffler, W. W. Destler, R. Kulkarni, and R. L. Weiler, *IEEE Trans. Nucl. Sci.* **NS-30**, 3429 (1983).
- ¹⁰K. R. Chu and D. Dialetis, *Int. J. Infrared Millimeter Waves* **5**, 37 (1984).
- ¹¹H. S. Uhm, C. M. Kim, and W. Namkung, *Phys. Fluids* **27**, 488 (1984).
- ¹²D. Chernin and Y. Y. Lau, *Phys. Fluids* **27**, 2319 (1984).
- ¹³M. J. Rhee and W. W. Destler, *Phys. Fluids* **17**, 1574 (1974).
- ¹⁴W. W. Destler, R. L. Weiler, and C. D. Striffler, *Appl. Phys. Lett.* **38**, 570 (1981).
- ¹⁵W. W. Destler, *Bull. Am. Phys. Soc.* **28**, 1087 (1983).
- ¹⁶W. W. Destler and W. Lawson, *Bull. Am. Phys. Soc.* **29**, 1281 (1984).
- ¹⁷B. Chang, D. B. McDermott, and N. C. Luhmann, Jr., *Bull. Am. Phys. Soc.* **29**, 1180 (1984).
- ¹⁸D. B. McDermott, N. C. Luhmann, Jr., P. S. Furuno, and A. Kupiszewski, *Int. J. Infrared Millimeter Waves* **4**, 639 (1983).
- ¹⁹H. S. Uhm and R. C. Davidson, *Phys. Fluids* **20**, 771 (1977).
- ²⁰M. Abramowitz and I. A. Stegun, *Handbook of Mathematical Functions* (Dover, New York, 1965), p. 3610.
- ²¹W. Lawson and C. D. Striffler, *Bull. Am. Phys. Soc.* **29**, 1179 (1984).
- ²²J. E. Walsh, T. C. Marshall, and S. P. Schlesinger, *Phys. Fluids* **20**, 709 (1977).
- ²³M. Abramowitz and J. A. Stegun, in Ref. 20, p. 374.
- ²⁴R. J. Briggs and V. K. Neil, *J. Nucl. Energy, Part C* **8**, 255 (1966).
- ²⁵C. D. Striffler and W. Lawson, *Bull. Am. Phys. Soc.* **29**, 1281 (1984).

High-Power Microwave Generation from a Large-Orbit Gyrotron in Vane and Hole-and-Slot Conducting Wall Geometries

WESLEY LAWSON, WILLIAM W. DESTLER, MEMBER, IEEE, AND CHARLES D. STRIFFLER, MEMBER, IEEE

Abstract—The production of high-power microwave radiation from a large-orbit gyrotron in azimuthally periodic boundary systems is studied theoretically and experimentally. Linear growth rates are calculated for the 2π modes of magnetron-like vane resonator (VR) and hole-and-slot resonator (HASR) systems using a general growth-rate formalism. The experiment involves the interaction of a 2.3-MeV, 1-2-kA, 5-ns rotating electron layer with two different periodic structures. About 500 MW is produced in *Ku* band with a 20-slot VR system and about 300 MW is produced in *X* band with a 10-slot HASR system. The relative merits of both types of systems are discussed.

I. INTRODUCTION

A. General Discussion

IN RECENT YEARS, there has been considerable theoretical and experimental work performed on the subject of microwave generation at high cyclotron harmonics from large-orbit gyrotrons. These devices would be extremely desirable in high-power high-frequency applications because of the reduced magnetic-field requirements inherent in high-harmonic operation. Recent theoretical studies [1], [2] with smooth wall geometries indicate that multimoding would occur in high-energy systems because of the slow variation of growth rate with harmonic number l . Subsequent theoretical studies [3]–[7] considered azimuthally periodic structures in attempts to favorably select a particular harmonic. These studies concentrated on the magnetron-like vane resonator (VR) structure.

Microwave radiation at cyclotron harmonics from a rotating *E* layer has been observed [8] (and subsequently analyzed [9]) in the Astron machine. More recently, this radiation process has been the subject of several experimental studies on the University of Maryland's high-energy Rotating Beam Facility (RBF) [10], [11]. With a smooth cylindrical conducting boundary, broad-band radiation was observed in *X* band (8–12 GHz) at power levels of ~200 kW per mode. With a 12-vane system and a cyclotron frequency of ~0.77 GHz, single-mode operation at ~9.6 GHz was achieved at power levels more than three orders of magnitude above the smooth wall results.

Manuscript received March 29, 1985; revised July 31, 1985. This work was supported in part by the Air Force Office of Scientific Research and in part by the University of Maryland Computer Science Center.

The authors are with the Electrical Engineering Department and Laboratory for Plasma and Fusion Energy Studies, University of Maryland, College Park, MD 20742.

In this study, a general growth-rate formalism is applied to the VR configuration and to the magnetron-like hole-and-slot resonator (HASR) configuration. For both cases, the properties of the dispersion and growth-rate curves are considered in detail. Designs for a 20-slot VR structure and a 10-slot HASR structure are analyzed according to the linear theory. Experimental results for the two designs are then presented and discussed.

The theoretical formalism is discussed in Sections I-B and I-C and the experimental apparatus is described in Section I-D. In Section II, the VR structure is presented. The HASR structure is the subject of Section III and conclusions are drawn in Section IV.

B. Theoretical Formalism in Axisymmetric Systems

In this paper, linear growth rates are calculated for the azimuthally periodic structures via a general growth-rate formula that was derived previously by the authors [12]. The general formalism is valid for a special class of cylindrical waveguide systems. The systems have thin, tenuous, large-orbit, annular electron beams. Furthermore, the systems are axisymmetric and invariant under translations in the \hat{z} direction. For systems that satisfy the above assumptions, an explicit formula gives the linear growth rates of the EM waves. In Section I-C, it is shown that the axisymmetric growth-rate formula can be applied directly to azimuthally periodic systems in an appropriate limit.

The type of system considered by the general formalism has an electron beam propagating in some cylindrical waveguide immersed in a uniform magnetic field B_0 (see Fig. 1). The beam is assumed to be cold; all electrons move predominately on helical orbits about the system axis. The beam is also assumed to be very thin; its equilibrium density is given by

$$n_0(r) = n_s \delta(r - r_0) \quad (1)$$

where r_0 is the equilibrium beam radius and n_s is the surface particle density. Furthermore, the beam is assumed to be sufficiently tenuous so that the dc self-fields are neglected. Each electron has an initially unperturbed (normalized) velocity of $(0, \beta_{\theta 0}, \beta_z)$. This simple distribution enables the use of the single-particle equations in the analysis.

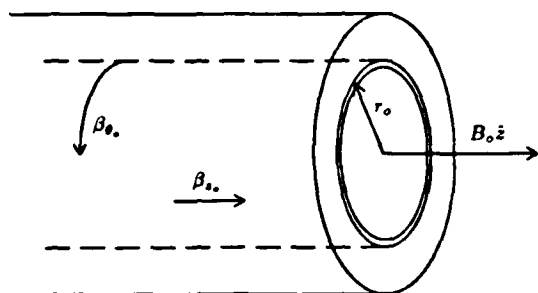


Fig. 1. The equilibrium model.

The linear growth-rate problem is divided into two parts. The first part involves the calculation of the perturbed sources in terms of the EM fields via the equations of motion and charge conservation. The linearized and Fourier-analyzed ($\exp[i(k_z z + l\theta - \omega t)]$ dependence) equations are solved for the perturbed current to lowest order in the parameter $\psi_l = \omega - l\Omega_0 - ck_z\beta_{z0}$:

$$\frac{\psi_l^2 J_{l1}}{\epsilon_0 c} = 0 \quad (2a)$$

$$\frac{\psi_l^2 J_{l0}}{\epsilon_0 c} = - \left(\frac{2\nu}{\gamma_0} \right) \Omega_0 [-i\Omega_0 \bar{E}_z^0 + \Omega_0 (r\partial_r c\bar{B}_z^0)] \delta(r - r_0) \quad (2b)$$

$$\frac{\psi_l^2 J_{z1}}{\epsilon_0 c} = - \left(\frac{2\nu}{\gamma_0} \right) \frac{v_{z0}}{r_0} [-i\Omega_0 \bar{E}_z^0 + \Omega_0 (r\partial_r c\bar{B}_z^0)] \delta(r - r_0) \quad (2c)$$

where $\gamma_0 m_0 c^2$ is the equilibrium particle energy, $\Omega_0 = eB_0/(m_0 \gamma_0)$, $\Omega_s = k_z c - \omega\beta_{z0}$, $\nu = n_s e^2 r_0 \mu_0 / (2m_0)$ is Budker's parameter, and the superscript zeros indicate that the fields are to be evaluated at the equilibrium radius r_0 .

The parameter ψ_l is a measure of the difference between the frequencies of the actual EM wave and the beam perturbation ($\omega_0 = l\Omega_0 + ck_z\beta_{z0}$). The synchronous limit is defined by $\psi_l \rightarrow 0$. Thus a beam is said to be synchronous with an EM wave when ψ_l is small compared to the other frequencies in the analysis ($\psi_l \ll \Omega_0$ in particular). A beam is said to be resonant if ω_0 is equal to the frequency of an empty waveguide mode. This paper considers exclusively the synchronous resonant case.

In the second part of the analysis, the r direction is divided into two regions: Region I, where $r < r_0$, and Region II, where $r > r_0$. In those regions, $\bar{J} = 0$ and the axial fields are written as a linear combination of Bessel functions (the homogeneous wave equation solutions):

$$\chi(r) = AJ_l(\xi r) + BY_l(\xi r) \quad (3)$$

for $\xi^2 = (\omega/c)^2 - k_z^2$ and $\chi = \{E_z, cB_z\}$. The boundary conditions that do not involve the beam are applied in order to find the solutions in the two regions in terms of the unknowns \bar{E}_z^0 and $(r\partial_r c\bar{B}_z^0)$. The system of equations is closed by integrating two components of Ampere's law across the beam. Two equations are produced that express the jumps in $c\bar{B}_z$ and $r\partial_r \bar{E}_z$ across the beam in terms of

certain beam parameters and the values of $(r\partial_r c\bar{B}_z^0)$ and (\bar{E}_z^0) .

Although the beam generally couples the axial fields together, the synchronous resonant growth rates for homogeneous TE modes depend only on $c\bar{B}_z$ and its derivative. The empty waveguide solutions and corresponding growth rates for homogeneous TE modes are given by

$$g_{bb} \equiv \frac{c\bar{B}_z(r_0^+) - c\bar{B}_z(r_0^-)}{(r\partial_r c\bar{B}_z^0)} \Big|_{E_z^0=0} = 0 \quad (4a)$$

and

$$\frac{\Gamma_{TE}}{\Omega_0} = \frac{\sqrt{3}}{2} \left| \frac{2\nu/\gamma_0}{\Omega_0 \partial_\omega g_{bb}} \right|^{1/3} \quad (4b)$$

for $\Gamma = \text{Im}(\omega)$. Equation (4) is applied to VR systems in Section II and to HASR systems in Section III.

C. Extension of the Growth-Rate Formula to Azimuthally Periodic Structures

The systems considered in this paper are assumed to be invariant under translations in the \hat{z} direction. Consequently, the general EM wave solution can be written as a sum over the azimuthal harmonic numbers l . In the axisymmetric analysis, all the boundary conditions are satisfied with only one harmonic perturbation and the amplitudes of all the other harmonic perturbations are set to zero. Without azimuthal symmetry, the harmonic perturbations are coupled together. Nonetheless, (2) is valid for each l , provided that \bar{E}_z^0 and $(r\partial_r c\bar{B}_z^0)$ are interpreted to be the coefficients corresponding to the l th harmonic of the fields.

The synchronous condition implies that the actual EM wave frequency is near one of the beam frequencies. Because each beam mode is separated by Ω_0 , only one of the ψ_l 's will be small (if $\psi_l \ll \Omega_0$, then $\psi_{l+n} \sim n\Omega_0$). If l_0 corresponds to the synchronous beam mode, then as $\psi_{l_0} \rightarrow 0$, J_{l_0} becomes much larger than all the other perturbed current harmonics. Consequently, the synchronous assumption implies that only one harmonic in the beam is excited. Thus $(r\partial_r \bar{E}_z)_{l_0}$ and $(c\bar{B}_z)_{l_0}$ will be subjected to jump conditions at r_0 , but all the other field harmonics will be continuous across the beam. This implies that there are still only two boundary conditions that involve the beam. Hence, the boundary conditions away from the beam can be used to find the field profiles in terms of two unknowns. In other words, the linear growth-rate formula can be applied directly to the periodic case without any additional assumptions.

The solution is still found by dividing the space in the waveguide into appropriate regions and applying all of the boundary equations away from the beam. One of the boundaries is at the inner radius of the slotted wall. The exact solution involves matching the EM fields just above and below this boundary at every azimuthal location. The first simplifying assumption is that the slots only contain the $l = 0$ harmonic. This means that the EM fields remain constant across a given slot opening and they cannot all

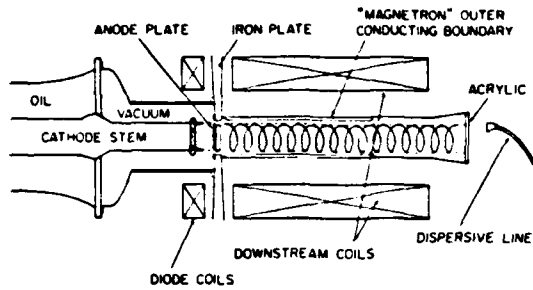


Fig. 2. The general experimental configuration.

be matched exactly. Instead, one of the fields ($c\vec{B}_z$) is matched on the average across the opening. This technique corresponds to the impedance matching technique used in early magnetron research [13]. This assumption enables the empty waveguide dispersion relation to be written in a reasonably simple form. The dispersion relation can in principle be found without this assumption, but the exact solution requires the calculation of the determinant of an infinitely large matrix. It has been shown that the approximate results are close to the exact results in cases similar to those considered in this paper [14].

In general, there can be a uniform phase shift between each pair of neighboring slots, provided that the total phase shift around the structure is a multiple of 2π . This analysis considers only the 2π mode (i.e., all resonators are in phase), because we believe that it is the predominant mode in our geometry. Our belief is based on an initial condition calculation [15] which shows that the 2π mode is favored in systems where the beam is symmetrically injected into the resonator. For the 2π mode, it can be shown that the EM fields only contain multiples of n , where n is the number of resonators in the system. The synchronous harmonic is assumed to be $l_0 = n$.

Finally, it turns out that the empty waveguide modes for the slotted wall systems still decouple into TE and TM modes. Only resonant interactions with magnetron-TE modes are considered in this paper.

D. Experimental Apparatus

A brief description of the experimental apparatus is offered here; a more detailed description can be found in [10]. The RBF is shown schematically in Fig. 2. The beam is produced at the knife-edged cathode of a field-emission diode. The rotating E layer is generated by passing the linearly streaming annular beam through a balanced magnetic cusp [16]. The cusp is maintained by two sets of pancake coils on opposite sides of an iron plate. The downstream magnetic field is essentially uniform in the region 0.15 to ≥ 1.0 m from the cusp center. In this uniform region, magnetic-field measurements are accurate to within 1 percent. Nominally, the electron beam has a 0.06-m radius, an energy of ~ 2.3 MeV, a current of 1-2 kA, and a post-cusp pulse duration of ~ 5 ns.

The signal is generated by the interaction of the rotating beam with the magnetron-like structure and travels through the remainder of the downstream region (total

length of ~ 3 m) in a smooth cylindrical waveguide. A cylindrical horn at the end of the drift tube provides the transition to free space. The transition from the smooth wall radius to the final horn radius of ~ 0.15 m occurs in ~ 0.50 m. Measurements of the radiated power at this point indicate that it is unpolarized and almost uniformly distributed over the solid angle subtended by the output horn. The absence of any mode pattern is attributed partially to the resolution limit of the receiving horn and partially to mode conversion both at the periodic wall-smooth wall boundary and in the output horn. An open-ended waveguide (WR90) placed >5 free-space wavelengths from the transmitting horn is used as the receiving horn in the X-band measurements. A rectangular horn with a 2.3×10^{-3} m² cross-sectional area placed >10 free-space wavelengths from the transmitting horn is used in the Ku -band measurements.

The portion of the radiated power picked up by the receiving antenna is transmitted down a long rectangular waveguide (~ 35 m). The waveguide provides both signal dispersion and attenuation. At the end of this dispersive line, the signal is further attenuated by a directional coupler and a variable attenuator. The final power level is measured by a calibrated crystal detector which is connected to an oscilloscope through a 50- Ω load.

The total output power is estimated by calculating the fraction of power intercepted by the receiving horn and correcting for the attenuation suffered by the signal along its path to the detector [10]. As in all high-power microwave measurements of this type, total peak power is difficult to measure to an accuracy of better than 3 dB. The spectrum is determined by measuring the arrival time of the signal and using standard dispersive line theory. Uncertainties in the frequency and power measurements due to the uncertainty in the measurement of the arrival time can also be easily found from dispersive line theory.

II. THE VANE-RESONATOR CONFIGURATION

A. Theory

The VR system is shown in Fig. 3. The beam radius is r_0 , the inner wall radius of the magnetron structure is r_w , the outer wall radius is r_s , and the number of slots is n . The angle of the slot opening is $\Delta\theta$ and the angle of one period is θ_r . The region defined by $r < r_w$ is denoted by the interaction region. The region defined by $r_w < r < r_s$ is called the slot region.

Using the fact that $c\vec{B}_z$ is bounded as $r \rightarrow 0$ and that only the n th azimuthal component of $c\vec{B}_z$ is discontinuous at r_0 , it can be seen that

$$c\vec{B}_z = \sum_{l=-\infty}^{\infty} (r\partial_r c\vec{B}_z)_l \left[\frac{J_l(x)}{x_n J_l(x_n)} \right] e^{il\theta} + (r\partial_r c\vec{B}_z)_n^0 \left[\frac{J_n(x)}{x_0 J_n(x_0)} \right] e^{in\theta} \quad (5a)$$

when $0 \leq r < r_0$, and

$$\begin{aligned}
c\bar{B}_z &= \sum_{\substack{l=-\infty \\ l \neq n}}^{\infty} (r\partial_r c\bar{B}_z)_l^- \left[\frac{J_l(x)}{x_w J'_l(x_w)} \right] e^{il\theta} \\
&+ (r\partial_r c\bar{B}_z)_n^- \left[\frac{Q_n(x, x_0)}{x_w S_n(x_w, x_0)} \right] e^{in\theta} \\
&+ (r\partial_r c\bar{B}_z)_n^0 \left[\frac{Q_n(x, x_w)}{x_0 S_n(x_0, x_w)} \right] e^{in\theta} \quad (5b)
\end{aligned}$$

when $r_0 < r < r_w$, and

$$c\bar{B}_z = \begin{cases} (r\partial_r c\bar{B}_z)^+ \left[\frac{Q_0(x, x_s)}{x_w S_0(x_w, x_s)} \right], & 0 \leq \theta_p \leq \Delta\theta \\ 0, & \Delta\theta \leq \theta_p \leq \theta_r \end{cases} \quad (5c)$$

when $r_w < r \leq r_s$, where $\theta_p = \theta - p\theta_r$, $0 \leq p \leq n-1$, $\xi = [(\omega/c)^2 - k_z^2]^{1/2}$, $x = r\xi$, etc., and the superscript \pm refers to r_w^\pm . The standard notation for the cross products of Bessel functions has been adopted here [17]:

$$P_n(a, b) = J_n(a) Y_n(b) - Y_n(a) J_n(b) \quad (6a)$$

$$Q_n(a, b) = J_n(a) Y'_n(b) - Y_n(a) J'_n(b) \quad (6b)$$

$$R_n(a, b) = J'_n(a) Y_n(b) - Y'_n(a) J_n(b) \quad (6c)$$

$$S_n(a, b) = J'_n(a) Y'_n(b) - Y'_n(a) J'_n(b). \quad (6d)$$

The continuity of \bar{E}_θ at r_w requires that

$$\frac{(r\partial_r c\bar{B}_z)_l^-}{(r\partial_r c\bar{B}_z)^+} = \begin{cases} \Delta\theta/\theta_r, & l = 0 \\ \frac{n/l}{\pi} \sin(l\Delta\theta/2) e^{-il\Delta\theta/2}, & l/n \text{ an integer} \\ 0, & \text{else.} \end{cases} \quad (7)$$

Matching the average value of $c\bar{B}_z$ across the slot opening results in a relationship between $(r\partial_r c\bar{B}_z)^+$ and $(r\partial_r c\bar{B}_z)_n^0$. The geometry factor g_{hb} can then be found from (4) to be

$$g_{hb} = \frac{D(\xi)}{D(\xi) \left[\frac{x_0^2 J_n^2(x_0) S_n(x_0, x_w)}{J_n^2(x_w)} \right] + \left(\frac{\Delta\theta}{\theta_r} \right) \frac{x_0^2}{x_w} \left[\frac{J_n^2(x_0)}{J_n^2(x_w)} \right] \left[\frac{\sin(n\Delta\theta/2)}{n\Delta\theta/2} \right]^2} \quad (8)$$

where the slot term is given by

$$D_s(\xi) = \frac{Q_n(x_w, x_r)}{S_0(x_w, x_r)} \quad (9a)$$

and the interaction region term is given by

$$D_i(\xi) = \left(\frac{\Delta\theta}{\theta_r} \right) \sum_{q=-\infty}^{\infty} \frac{J_{qn}(x_w)}{J'_{qn}(x_w)} \left[\frac{\sin(qn\Delta\theta/2)}{qn\Delta\theta/2} \right]^2 \quad (9b)$$

and

$$D(\xi) = D_s(\xi) - D_i(\xi). \quad (9c)$$

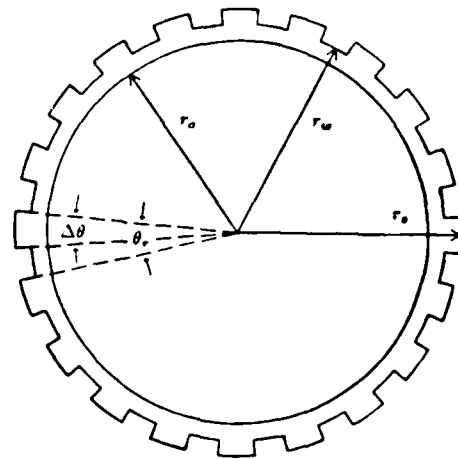


Fig. 3. Cross section of the 20-slot VR structure.

Equation (4) implies that the magnetron-TE empty waveguide modes are given by $D(\xi) = 0$ and that the resonant growth rate for these modes is given by

$$\frac{\Gamma}{\Omega_0} = \frac{\sqrt{3}}{2} \left\{ \left(\frac{2\nu/\gamma_0}{x_w \Omega_0 \partial_w D(\xi)} \right) \left(\frac{\Delta\theta}{\theta_r} \right) \left[\frac{\sin(n\Delta\theta/2)}{n\Delta\theta/2} \right]^2 \cdot \left[\frac{x_0 J_n^2(x_0)}{J_n^2(x_w)} \right]^{1/3} \right\} \quad (10)$$

The results for the non 2π modes are quite similar. If the phase shift between two adjacent resonators is assumed to be $\exp[i l_0 \theta_r]$ for $0 < l_0 < n$, then the correct empty waveguide dispersion relation is found by substituting $l_0 + qn$ for qn wherever it appears in (9b). If the synchronous harmonic is l_0 , then the correct growth rate is found by substituting l_0 for n everywhere in (10). Non 2π mode growth rates for VR systems have been computed elsewhere [5]. Those results typically indicate that the growth rates are comparable to the growth rates of 2π modes.

B. Design

The parameters for the experimental VR structure are $n = 20$, $r_w = 0.0652$ m, $r_s = 0.070$ m, and $\Delta\theta/\theta_r = 0.535$. Plots of $D_s(\xi)$ and $D_i(\xi)$ for these parameters are shown in Fig. 4. Solutions of the empty waveguide equation occur whenever the D_s and D_i curves intersect and are indicated in the figure by circles. The radial mode with which we expect predominant beam interaction is also indicated in the figure. The poles of D_s are given by the zeros of $J'_{qn}(x_w)$ for $q = \{0, 1, \dots\}$, and the poles of D_i are given by the zeros of $S_0(x_w, x_r)$. When $r_s - r_w \ll r_w$, D_s varies

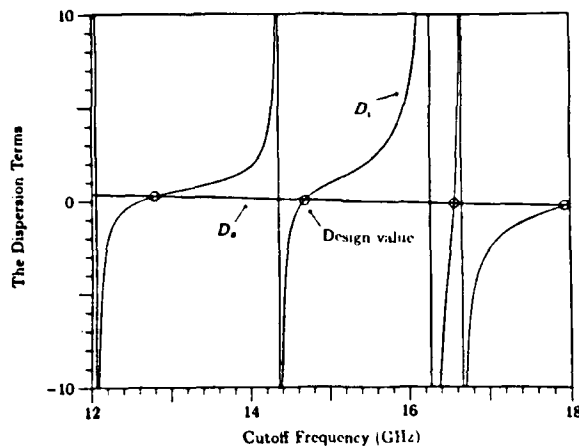


Fig. 4. The contributions of the slot and interaction regions to the dispersion function of the VR system. The circles indicate empty waveguide solutions. Parameters: $n = 20$, $r_w = 0.0652$ m, $r_s = 0.070$ m, $\Delta\theta/\theta = 0.535$.

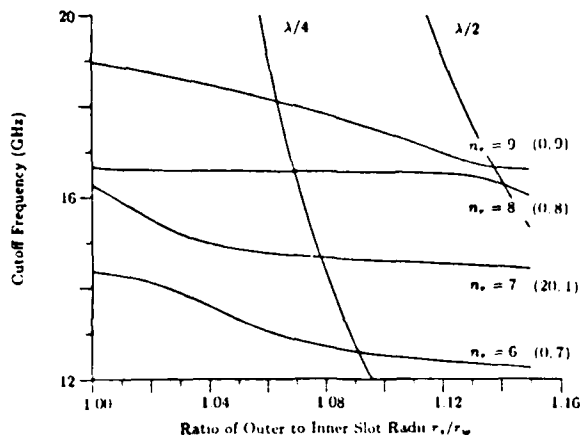


Fig. 5. The dependence of the cutoff frequency on the slot depth. Parameters: $n = 20$, $r_w = 0.0652$, and $\Delta\theta/\theta = 0.535$.

rapidly compared to D_s , because the poles of D_i are far more frequent than the poles of D_s .

Because D_s is strictly decreasing and D_i is strictly increasing (on each domain where the functions are defined)

$$|D'(\xi)| = |D'_s(\xi)| + |D'_i(\xi)|.$$

We do not want to be near any of the poles of D_i , because $\Gamma \propto D'(\xi)^{-1/3}$. This generally means that we must have $|D_i|$ small at the desired operating point.

Fig. 4 can be used to determine the effect of adjustments in the parameters on the cutoff frequencies of the various modes and the values of $D'(\xi)$ at those points. For example, increasing r_s does not affect D_s , but will cause D_i to decrease more rapidly, resulting in lower cutoff frequencies. Furthermore, the mode trapped between 16 and 16.5 GHz will have a low growth rate for all values of r_s .

The effect of slot depth on the cutoff frequency is further demonstrated in Fig. 5. The sixth through the ninth radial modes are plotted for $n = 20$, $r_w = 0.0652$ m, and $\Delta\theta/\theta = 0.535$. The cutoff frequencies of these modes are in the regime of beam-waveguide resonance. The smooth wall

case is located at $r_s/r_w = 1.0$. The numbers in parentheses next to each radial mode number n_r , indicate the limiting smooth wall mode as $r_s \rightarrow r_w$. For example, the seventh magnetron-TE radial mode approaches the first smooth wall radial mode of $l = 20$ when $r_s \rightarrow r_w$. As predicted, all of the cutoff frequencies are decreasing functions of the slot depth.

The EM wave in the slot can be naively pictured as a TEM wave traveling down a shorted waveguide. The $\lambda/4$ line indicates the time it would take a TEM mode to travel up and down the slot twice, assuming that it was traveling at the speed of light. The corresponding expression for the frequency is $f = c/[4(r_s - r_w)]$. The $\lambda/4$ label comes from the fact that a quarter-wavelength standing wave is approximately set up in the slot at these frequencies. For a VR system, the actual $\lambda/4$ frequencies are given by the first zero of $R_1(x_w, x_s)$. The frequency of the naive estimate is usually close to (but smaller than) the actual result. The $\lambda/2$ line roughly corresponds to the frequencies where \bar{E}_θ is zero at the slot entrance. The actual frequencies are given by the first zero of $S_0(x_w, x_s)$ (the first pole of D_s). At these frequencies, the standing wave in the slot is a half-wavelength. A $\lambda/2$ point always has poor coupling to the slot and should be avoided. At higher values of r_s/r_w (not plotted), good coupling can be achieved at frequencies corresponding to the $3\lambda/4$ slot mode.

The lowest azimuthal components of the \bar{E}_θ field for the desired operating point are plotted in Fig. 6. For the interaction region, the $l = 0$ contribution is plotted in Fig. 6(a) and the $l = 20$ contribution is plotted in Fig. 6(b). The total \bar{E}_θ field in the slot is plotted in both figures and is normalized to unity at the slot entrance. For this case ($r_s/r_w = 1.074$), the operating frequency is below the $\lambda/4$ frequency and the standing wavelength is slightly less than $\lambda/4$.

The bulk of the $l = 20$ field component is near r_w . Because resonant interaction occurs at $l = 20$, it is necessary to place the beam near that wall. Furthermore, a study considering the initial condition problem on the RBF [15] concluded that the beam should be placed at a maximum of the $l = 0$ component of \bar{E}_θ . Our 0.06-cm beam radius well satisfies both criteria. In fact, the best experimental results for the VR system occur when the downstream magnetic field is made a few percent larger than the diode magnetic field. The effect of this unbalanced cusp is to decrease the average beam radius [18], placing the beam in an even more favorable location.

The magnetron-TE dispersion relation in $\omega - ck_z$ space is a hyperbola given by $\omega_c^2 = \omega_{cut}^2 + c^2 k_z^2$, where ω_{cut} is the cutoff frequency of the mode under consideration (see Fig. 5 for ω_{cut}). Resonances occur at axial wavenumbers where $\omega_r(k_r) = \omega_0(k_r)$. In general there are two values of k_r for resonances; these are denoted as a low-frequency resonance (sometimes a backward traveling wave) and a high-frequency resonance (always a forward traveling wave). When these two roots converge into one, this resonance is denoted as the grazing condition. A given beam mode interacts with any radial mode that has

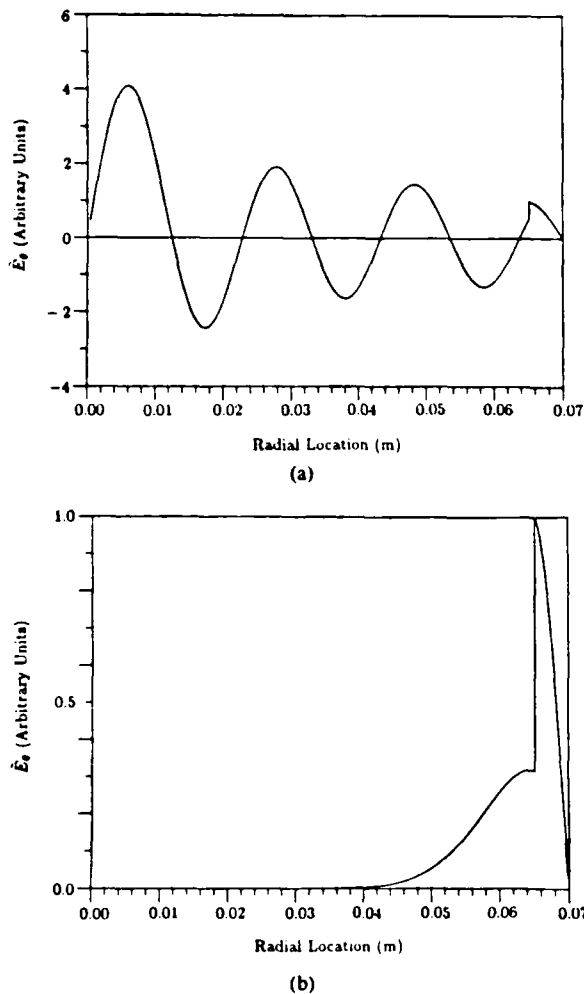


Fig. 6. The VR empty waveguide \vec{E}_z field at the center of the slot opening: (a) the $l = 0$ component and (b) the $l = n$ component. The 20 slot VR parameters: $n = 20$, $n_r = 7$, $r_w = 0.0652$, $r_s = 0.070$ m, and $\Delta\theta/\theta_r = 0.535$. See (7).

$$\omega_{\text{cut}} \leq \frac{l\Omega_0}{(1 - \beta_{z0}^2)^{1/2}}. \quad (11)$$

In high-energy machines, the resonant frequencies are usually very sensitive to small changes in the beam energy and the applied magnetic field. This is especially true for the highest radial mode that satisfies (11). Unfortunately, the highest resonant radial mode is usually the desired mode for operation. The design procedures are further complicated by the uncertainty in the RBF beam energy.

A plot of growth rate versus $f_r = \omega_r/2\pi$ at the resonant points is shown in Fig. 7 for nominal beam parameters: $n_r = 10^{14} \text{ m}^{-2}$, $\beta_{0n} = 0.951$, $\beta_{z0} = 0.250$, and $r_0 = 0.06$. The beam energy is adjusted slightly so that equality in (11) is nearly achieved for the highest radial mode (the so-called grazing condition [12]). The growth rate for the desired mode is reasonably large at ~ 15.2 GHz. Thus the theoretical considerations seem favorable for this configuration and microwave radiation from a single radial mode appears likely.

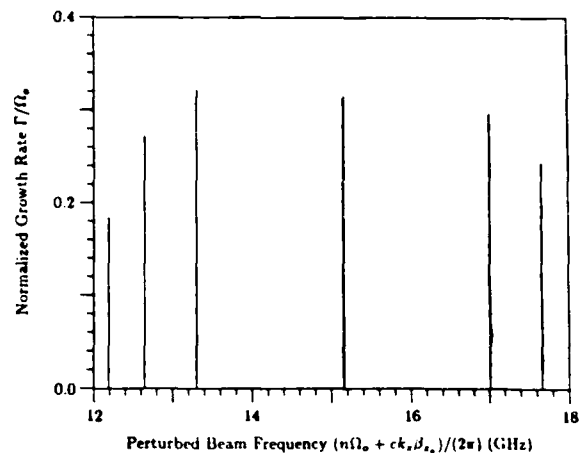


Fig. 7. The linear growth rates for the 20-slot VR system. Beam parameters: $n_r = 10^{14} \text{ m}^{-2}$, $\beta_{0n} = 0.951$, $\beta_{z0} = 0.250$, $r_0 = 0.06$ m. The VR parameters are given in Fig. 4. The growth rate at ~ 15.2 GHz is for the grazing condition with the $n_r = 7$ mode. The other low (-) and high (+) resonant mode interactions are: $\omega_-(n_r = 4) \sim 12.2$ GHz; $\omega_-(n_r = 5) \sim 12.6$ GHz; $\omega_-(n_r = 6) \sim 13.3$ GHz; $\omega_+(n_r = 6) \sim 17$ GHz; and $\omega_+(n_r = 5) \sim 17.7$ GHz.

C. Experiment

Previous experimental studies of high-power microwave generation from rotating electron beams in magnetron-like boundary systems have included configurations with a) outer VR boundaries only [11], b) coaxial systems with resonators on the outer wall, c) coaxial systems with resonators on the inner wall [5], and d) coaxial systems with resonators on both walls (in phase and 180° out of phase) [5]. Previous attempts to produce microwaves at or around the twentieth harmonic of the electron cyclotron frequency have shown that the slot depth and the radial position of the beam relative to the resonators are of critical importance in maximizing microwave output. Maximum microwave power observed at the twentieth harmonic using inner wall resonators is about 40 MW.

The best $n = 20$ VR results to date were obtained using an outer wall resonator system with $r_w = 0.0652$ m, $r_s = 0.070$ m, and $\Delta\theta/\theta_r = 0.535$. The resonators are placed 14 cm back from the iron plate so that they will not scrape off the beam during its initial expansion. A typical result for the VR experiment is shown in Fig. 8. Approximately 500 MW of power is observed at a frequency of 15.5 GHz. Power levels at other frequencies are typically down by a factor of 15 dB. For this case, the diode magnetic field is set to 1450 G and the downstream field is set to 1500 G. The average field of 1475 G is very close to the cutoff field of 1525 G (see [16]). Consequently, the axial velocity is relatively low and the beam density is high. This result represents about a 15-percent conversion efficiency of beam power to RF power.

The error bars in Fig. 8 do not reflect the uncertainty in the power level due to possible systematic error in the general measurement scheme (e.g., error in the estimation of the fraction of power intercepted by the receiving horn). In Section I-D, we estimated that error to be ± 3 dB. Instead, the error bars incorporate only the uncertainties

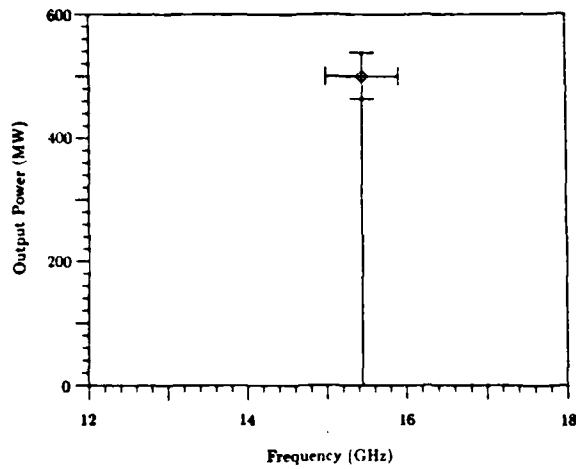


Fig. 8. Radiated microwave spectrum from the 20-slot VR system. Diode magnetic field: 1450 G. Downstream field: 1500 G. Approximate beam parameters are given in Fig. 7. The error bars incorporate only the uncertainties in the measurements of the arrival time and the detector voltage. They do not reflect possible systematic errors in the power measurement scheme.

in the measurements of the arrival time and the detector voltage. In this way, relative comparisons between the results of the various wall configurations can reasonably be made. Unfortunately, the large net error estimate (± 3.5 dB) leaves the uncertainty in the efficiency to be (more than) a factor of two.

The diagnostics for the experiment leave several questions unanswered. For example, at these high harmonics, the mode spacing is quite small and the uncertainty in the beam energy makes it impossible for us to identify the exact mode from the frequency measurements. Thus it is possible that the machine is actually operating in a mode near the synchronous 2π mode. The experimental results are consistent with the 2π mode theory, but they do not confirm it.

In spite of the uncertainties, several conclusions can be drawn from this and previous experiments on the RBF. First, a properly designed periodic structure can excite radiation at a single frequency with power levels three orders of magnitude above those from a smooth wall configuration. Also, the output from this 20-slot VR experiment is comparable in power to the best 12-slot VR experiments previously performed on the RBF. This result indicates that the outlook for operating at extremely high cyclotron harmonics is promising (although initial 30-slot VR experiments had severe multimoding problems and achieved power levels at best a factor of 10 higher than smooth wall results [19]). Finally, it should be pointed out that in previous studies with periodic structures on the inner wall [4], radiation in the frequency range consistent with the π mode remained at smooth wall power levels (were not enhanced) in systems that radiated effectively in the frequency range consistent with the 2π mode. This fact lends some support to the initial condition calculation, because the cusp injects the rotating beam symmetrically into the region with the periodic structures.

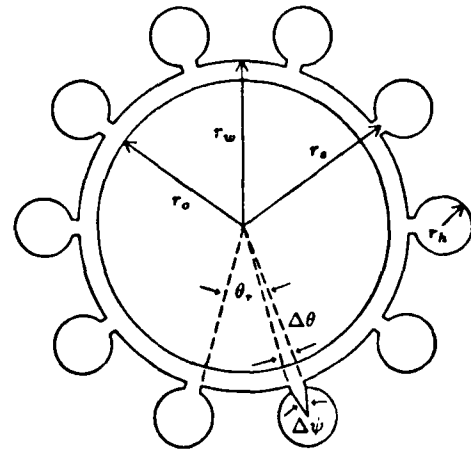


Fig. 9. Cross section of the 10-slot HASR structure.

III. THE HOLE-AND-SLOT CONFIGURATION

A. Theory

The HASR system is shown in Fig. 9. It is assumed that the HASR system consists of a VR system with a hole added at the end of each vane. The rectangular slot case is similar and is not considered here. The hole radius is r_h and the angle of the hole opening is $\Delta\psi = 2 \sin^{-1} [\sin(\Delta\theta/2) r_s/r_h]$.

An additional assumption has to be made for the HASR system. Let r and θ denote the cylindrical coordinates whose origin is at the center axis, and let r^* and θ^* denote the cylindrical coordinates whose origin is at the center of a (hole) resonator. At the opening of the hole, the arc defined by $|r| = r_s$ is assumed to coincide with the arc defined by $|r^*| = r_h$. This assumption will be good only for relatively thin slots. Mathematically, the restriction is that $\Delta\theta \ll r_h/r_s$. This assumption simplifies the calculation of the boundary conditions at the hole opening, because the fields in the resonator are easily expressed in terms of the (r^*, θ^*) coordinate system.

The field in the slot is now

$$c\vec{B}_z = (r\partial_r c\vec{B}_z)^* \frac{Q_0(x, x_s)}{x_s S_0(x_s, x_s)} + (r\partial_r \vec{B}_z)^* \frac{Q_0(x, x_s)}{x_s S_0(x_s, x_s)} \quad (12a)$$

and the field in the hole resonator is

$$c\vec{B}_z = \sum_{m=-\infty}^{\infty} (r\partial_r c\vec{B}_z)_m^* \frac{J_m(\lambda^*)}{x_h J'_m(\lambda_h)} e^{im\theta^*} \quad (12b)$$

where $x^* = r^*\xi$, $x_h = r_h\xi$, and the field in the interaction region is still given by (5a) and (5b).

The requirement that

$$\frac{(r\partial_r c\vec{B}_z)^*}{(r\partial_r c\vec{B}_z)} = \frac{\pi x_s}{2} \left\{ Q_0(x_s, x_s) + \frac{\Delta\psi}{2\pi} S_0(x_s, x_s) \cdot \sum_{m=-\infty}^{\infty} \frac{J_m(\lambda_h)}{J'_m(\lambda_h)} \left[\frac{\sin(m\Delta\psi/2)}{m\Delta\psi/2} \right]^2 \right\} \quad (13)$$

comes from matching \tilde{E}_θ and the average $c\tilde{B}_z$ field at $r = r_s$. At this point, the solution can be found by following the steps for the VR solution, because there is only one remaining unknown in the slot and all the boundary conditions at r_w remain to be applied.

The dispersion relation can be split into three parts. The slot term and the interaction term are still given by (9a) and (9b). The hole resonator term is given by

$$D_h^{-1}(\xi) = \left(\frac{\pi}{2}\right)^2 x_w x_s S_0(x_w, x_s) \times \left\{ R_0(x_w, x_s) + \frac{\Delta\psi}{2\pi} S_0(x_w, x_s) \sum_{m=-\infty}^{\infty} \frac{J_m(x_h)}{J'_m(x_h)} \left[\frac{\sin(m\Delta\psi/2)}{m\Delta\psi/2} \right]^2 \right\}. \quad (14)$$

The equations for the geometry factor (8) and the growth rate (10) are valid for the HASR system after the substitution

$$D(\xi) = D_h(\xi) + D_s(\xi) - D_r(\xi). \quad (15)$$

It is often more convenient to plot the entire resonator term $D_r(\xi) = D_s(\xi) + D_h(\xi)$. From (9a) and (14), it is easy to show that

$$D_r(\xi) = \frac{P_0(x_w, x_s) + (\Delta\psi/2\pi) Q_0(x_w, x_s) \sum_{m=-\infty}^{\infty} \frac{J_m(x_h)}{J'_m(x_h)} [\sin(m\Delta\psi/2)/m\Delta\psi/2]^2}{R_0(x_w, x_s) + (\Delta\psi/2\pi) S_0(x_w, x_s) \sum_{m=-\infty}^{\infty} \frac{J_m(x_h)}{J'_m(x_h)} [\sin(m\Delta\psi/2)/m\Delta\psi/2]^2}. \quad (16)$$

B. Design

The parameters for the HASR system are $n = 10$, $r_w = 0.068$ m, $r_s = 0.0703$ m, $r_h = 0.012$ m, and $\Delta\theta/\theta_r = 0.147$. The dispersion functions D_r and D_s are plotted in Fig. 10. Recall that solutions are given by the intersections of the two curves. In the figure, these points are indicated by circles. The system is designed to operate in the fifth radial mode. The cutoff frequency for that mode is 7.63 GHz. The poles and the zeros of D_r can be found from (16).

The analogy of TEM $\lambda/4$, $\lambda/2$, etc. modes is more abstract for the HASR resonators, but still can be applied. The $\lambda/2$ point, for example, corresponds to the first pole of D_r (16). In the experimental design, the $\lambda/2$ point is at ~ 7 GHz and the desired operating point is between that and the $3\lambda/4$ point. The proximity of the $\lambda/2$ point to the mode at 7.13 GHz results in a large value of $|D'(\xi)|$ and consequently a small value of growth rate (see (10)). However, D_r decreases sufficiently rapidly so that the desired mode has a favorable growth rate. Thus careful placement of the first pole of D_r can virtually eliminate competition from the radial mode nearest the desired operating point.

The 20-slot VR case previously discussed was designed for the $\lambda/4$ mode, had slowly varying growth rates, and should not be compared with this HASR example. However, the same idea can be applied to the VR systems operating between the $\lambda/2$ and $3\lambda/4$ points. In general, D_r varies more rapidly than D_s , and so the nulling of the near-

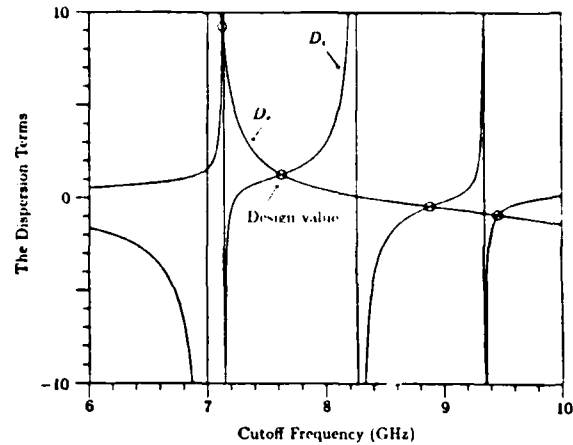


Fig. 10. The contributions of the resonator and interaction regions to the dispersion function of the HASR system. The circles indicate empty waveguide solutions. Parameters: $n = 10$, $r_w = 0.068$ m, $r_s = 0.070$ m, $r_h = 0.012$ m, $\Delta\theta/\theta_r = 0.147$.

est radial mode competitor may not be as complete with VR systems. The added flexibility in the choice of r_h is another advantage of HASR systems.

In Fig. 11, the total \tilde{E}_θ field profile of the fifth radial mode is plotted as a function of r . The field along the line

passing through the center of the slot is shown in Fig. 11(a). The \tilde{E}_θ field midway between slots is plotted in Fig. 11(b). The beam is located in a reasonably favorable position of the field profile. At small radii, the $l = 0$ term dominates and the field is essentially independent of azimuthal angle. However, near r_w , the $l = n$ term is quite strong and the \tilde{E}_θ field is essentially n periodic. Compared to the VR example, the relative contribution of the $l = 0$ term is greatly reduced. This is partly due to the smaller value of $\Delta\theta/\theta_r$, and partly due to the lower radial mode number. The \tilde{E}_θ field in the hole is quite large, though the hole volume is relatively small.

In the experiment, the best results occurred at magnetic fields between 1300 and 1325 G. The growth rates are shown in Fig. 12 for the nominal parameters $\beta_{e0} = 0.854$, $\beta_{e1} = 0.487$, and $r_0 = 0.06$ m. The growth rates for the fifth radial mode (at ~ 8.1 and ~ 9.7 GHz) are approximately six times larger than the growth rates of the fourth radial mode (at ~ 7.2 and ~ 10.6 GHz), indicating that single-mode operation should be feasible.

C. Experiment

The HASR system is inserted into the RBF and held in place ~ 15 cm from the iron plate. An adapter brought the wall radius down from the RBF's 7.5 cm to the HASR's 6.8 cm. The overall length of the HASR structure is ap-

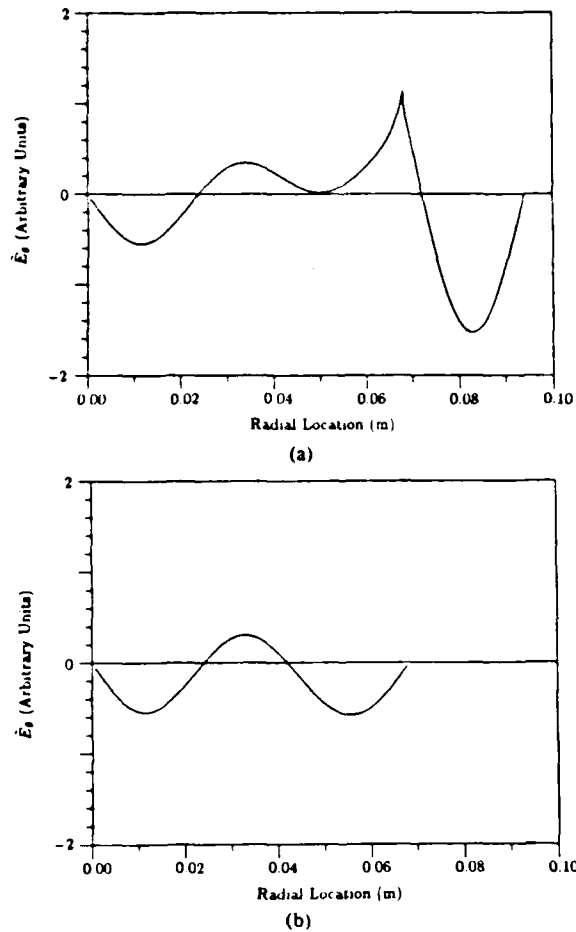


Fig. 11. The HASR empty waveguide E_z field: (a) at the slot center and (b) midway between two slot centers. The 10-slot HASR parameters: $n = 10$, $n_r = 5$, $r_w = 0.068$ m, $r_s = 0.070$ m, $r_h = 0.012$ m, and $\Delta\theta/\theta = 0.147$.

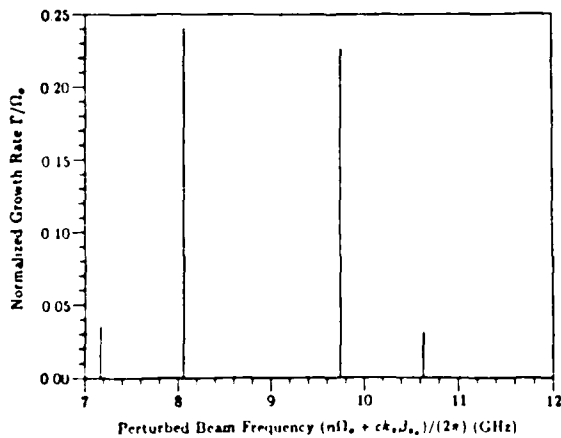


Fig. 12. The linear growth rates for the 10-slot HASR system. Beam parameters: $n_r = 10^{19}$ m $^{-3}$, $\beta_{z0} = 0.854$, $\beta_{\perp 0} = 0.487$, and $r_s = 0.06$ m. The HASR parameters are given in Fig. 10. The mode identifications are $\omega_-(n_r = 4) \sim 7.2$ GHz, $\omega_-(n_r = 5) \sim 8.1$ GHz, $\omega_+(n_r = 5) \sim 9.7$ GHz, and $\omega_+(n_r = 4) \sim 10.6$ GHz.

proximately 60 cm. Short rods with 20° tapers are inserted in the holes at the input side of the structure to provide a continuous transition from the smooth wall configuration to the periodic configuration. The HASR structure

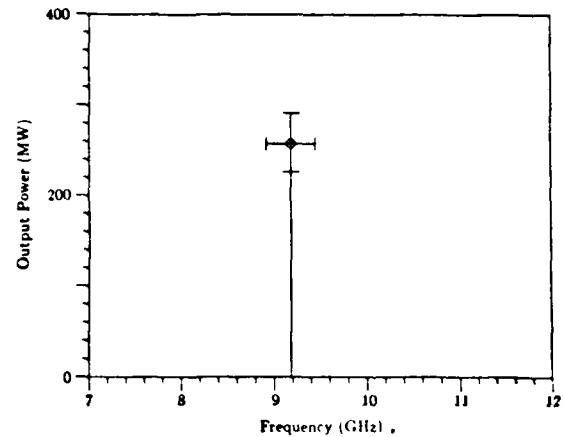


Fig. 13. Radiated microwave spectrum from the 10-slot HASR system. Magnetic field: 1300 G. Approximate beam parameters are given in Fig. 12. The error bars incorporate only the uncertainties in the measurements of the arrival time and the detector voltage. They do not reflect possible systematic errors in the power measurement scheme.

is tapered at the output end so that the large amount of field energy in the hole can easily be collected. The 24° taper brings the inner radius out to a smooth wall radius ($r_w > r_s + 2r_h$). A 10-cm-radius smooth wall tube brings the microwave radiation from the end of the HASR system to a cylindrical cone at the end of the vacuum chamber.

The best results for this experiment are shown in Fig. 13. Approximately 260 MW of power is observed at a frequency of 9.2 GHz in a balanced field of 1300 G. Power levels at other frequencies are typically down by more than 10 dB. Single-mode operation is consistently achieved at power levels exceeding 200 MW. By comparing Figs. 12 and 13, it appears these conditions represent the forward-wave resonance with the $n_r = 5$ waveguide mode.

It is unfortunate that the sharp resonance at 1300 G occurred so far below the cutoff field (1525 G). The beam density at this point is only one-half of the density at the 20-slot VR resonance point (because β_{z0} at 1300 G is nearly twice the value of β_{z0} at 1475 G). This reduction in n_r probably accounts (at least partially) for the reduced power levels in the 10-slot HASR device.

The error bars on the frequency measurement result from the uncertainty in the arrival-time measurement. Again, the power-level error bars reflect only the uncertainties in the arrival time and the detector voltage.

IV. SUMMARY

In this paper, we have shown that the results of a general axisymmetric linear growth-rate formalism are applicable to azimuthally periodic systems in the synchronous limit. We used the growth-rate formula to calculate the properties of magnetron-like VR and HASR structures. We found that the HASR system theoretically has an advantage over the VR system in that its parameters can be more readily adjusted to suppress radial mode competition. Unfortunately, an additional assumption in the HASR analysis forced a restriction on the maximum allowable size for the relative slot opening ($\Delta\theta/\theta$). This is undesirable be-

cause of the resultant reduction in slot coupling [$\Gamma \propto (\Delta\theta/\theta_r)^{1/3}$].

Experiments with a 20-slot VR system and a 10-slot HASR system successfully produced high-power microwaves at power levels comparable to previous 12-slot VR systems. The radiation in each case was determined to be at a single frequency (corresponding to a single mode) to within the accuracy of the dispersive line measurements. Both systems had relatively stable operation at frequencies consistent with synchronous 2π modes, although the modes were not positively identified as such. The results indicate that both of these configurations may be well suited to high-power generation in the centimeter and millimeter regime.

We have successfully demonstrated that more than one type of configuration can be used to promote single-mode operation in high-power large-orbit gyrotrons. However, much work remains to be done on these configurations before optimal designs can be built. Alternate schemes for periodic structures can be tested with the linear theory via (4). Nonlinear theories and particle simulations need to address questions of efficiency. Other experiments should be performed to determine the actual operating mode, test the initial condition calculation [15], and evaluate the suitability of various resonator configurations.

ACKNOWLEDGMENT

The authors would like to thank D. Cohen, J. Pyle, and F. Williams for their technical assistance.

REFERENCES

- [1] P. Sprangle, "Excitation of electromagnetic waves from a rotating annular relativistic E-beam," *J. Appl. Phys.*, vol. 47, no. 7, pp. 2935-2940, July 1976.
- [2] W. W. Destler, H. Romero, C. D. Striffler, R. L. Weiler, and W. Namkung, "Intense microwave generation from a non-neutral rotating E-layer," *J. Appl. Phys.*, vol. 52, no. 4, pp. 2740-2749, Apr. 1981.
- [3] Y. Y. Lau and L. R. Barnett, "Theory of a low magnetic field gyrotron (Gyromagnetron)," *Int. J. Infrared Millimeter Waves*, vol. 3, no. 5, pp. 619-644, Sept. 1982.
- [4] W. W. Destler, R. Kulkarni, C. D. Striffler, and R. L. Weiler, "Microwave generation from rotating electron beams in magnetron-type waveguides," *J. Appl. Phys.*, vol. 54, no. 7, pp. 4152-4162, July 1983.
- [5] C. D. Striffler, W. W. Destler, R. Kulkarni, and R. L. Weiler, "High power microwave generation from rotating E-layers in magnetron-type conducting boundary systems," *IEEE Trans. Nucl. Sci.*, vol. NS-30, no. 4, pp. 3429-3431, Aug. 1983.
- [6] K. R. Chu and D. Dialetis, "Theory of harmonic gyrotron oscillator with slotted resonant structure," *Int. J. Infrared Millimeter Waves*, vol. 5, no. 1, pp. 37-56, Jan. 1984.
- [7] H. S. Uhm, C. M. Kim, and W. Namkung, "Linear theory of cusptron microwave tubes," *Phys. Fluids*, vol. 27, no. 2, pp. 488-498, Feb. 1984.
- [8] N. C. Christofilos, R. J. Briggs, R. E. Hester, E. J. Lauer, and P. B. Wiess, "Experimental studies with the astron facility," in *IAEA Proc. Conf. Plasma Physics Controlled Nuclear Fusion Res.*, vol. 2, 1966, pp. 211-225.
- [9] R. J. Briggs and V. K. Neil, "Negative-mass instability in a cylindrical layer of relativistic electrons," *Plasma Phys.*, vol. C-9, pp. 209-227, 1967.
- [10] W. W. Destler, D. W. Hudgings, M. J. Rhee, S. Kawasaki, and V. L. Granatstein, "Experimental study of microwave generation and suppression in a non-neutral E Layer," *J. Appl. Phys.*, vol. 48, pp. 3291-3296, Aug. 1977.
- [11] W. W. Destler, R. L. Weiler, and C. D. Striffler, "High-power microwave generation from a rotating E-layer in a magnetron-type waveguide," *Appl. Phys. Lett.*, vol. 38, no. 7, pp. 570-572, Apr. 1981.
- [12] W. Lawson and C. D. Striffler, "A general linear growth rate formula for large orbit, annular electron beams," *Phys. Fluids*, vol. 28, no. 9, pp. 2868-2877, Sept. 1985.
- [13] G. B. Collins, *Microwave Magnetrons*. New York: McGraw-Hill, 1948, pp. 56-69.
- [14] J. Y. Choe, "Dispersion characteristics of the cusptron structure," *Bull. Amer. Phys. Soc.*, vol. 28, no. 8, p. 1142, Oct. 1983.
- [15] R. Kulkarni and C. D. Striffler, "Stability of a thin rotating E-layer with a magnetron-type slotted wall structure," *Bull. Amer. Phys. Soc.*, vol. 29, no. 8, p. 1179, Oct. 1984.
- [16] M. J. Rhee and W. W. Destler, "Relativistic electron dynamics in a cusped magnetic field," *Phys. Fluids*, vol. 17, no. 8, pp. 1574-1581, Aug. 1974.
- [17] M. Abramowitz and J. A. Stegun, Eds., *Handbook of Mathematical Functions*. New York: Dover, 1965, p. 361.
- [18] W. W. Destler and M. J. Rhee, "Radial and axial compression of a hollow electron beam using an asymmetric magnetic cusp," *Phys. Fluids*, vol. 20, no. 9, pp. 1582-1584, Sept. 1977.
- [19] W. Lawson, W. W. Destler, and C. D. Striffler, "High power microwave generation from a large orbit gyrotron," submitted to *IEEE Trans. Nucl. Sci.*, Oct. 1985, also in *1985 PAC Proc.*

Experimental study of millimeter wave radiation from a rotating electron beam in a rippled magnetic field

W. W. Destler, F. M. Aghamir, and D. A. Boyd
University of Maryland, College Park, Maryland 20742

G. Bekefi, R. E. Shefer, and Y. Z. Yin^{a)}
Massachusetts Institute of Technology, Cambridge, Massachusetts 02139

(Received 18 October 1984; accepted 10 March 1985)

The generation of millimeter wave radiation from the interaction of a rotating electron beam (2 MeV, 1 kA, 5 nsec) with an azimuthally periodic wiggler magnetic field has been studied experimentally. Calculations of the effects of the wiggler magnetic field on the single particle electron orbits are presented, together with experimental measurements of the effects of the wiggler field on the electron beam. Narrow-band radiation at power levels in excess of 200 kW has been observed at 88 and 175 GHz for wiggler fields with 6.28 and 3.14 cm periods, respectively. The radiation frequency spectra for various experimental configurations are presented, and results are compared with theoretical expectations.

I. INTRODUCTION

In recent years many theoretical and experimental studies have been reported of linear free-electron lasers (FEL's) in which short-wavelength radiation is produced by the interaction of an electron beam with a spatially periodic wiggler magnetic field.¹⁻¹⁰ Recently, a novel circular geometry FEL has been explored both theoretically and experimentally in a collaborative effort by researchers at the Massachusetts Institute of Technology and the University of Maryland.¹¹⁻¹⁶ In this concept, a rotating, relativistic electron beam interacts with an azimuthally periodic wiggler field produced by samarium cobalt magnets placed interior and exterior to the beam. The potential advantages of such systems include a longer effective interaction region, a more compact geometrical configuration, and internal feedback resulting from the recirculation of the electromagnetic wave. This last feature may mean that the device can operate as an oscillator rather than an amplifier, as in the case of linear FEL's.

In the experiments to date, two principal methods have been used to generate the rotating electron beam. The first experiments employed a diode configuration similar to those used in relativistic magnetrons.^{11,14} Here the electrons perform $E \times B$ drifts around the azimuth in the presence of a radial electric field and an axial magnetic field. Addition of an azimuthally periodic magnetic field then results in a circular FEL. Although initial experimental results from this configuration are encouraging, one potential drawback of this configuration is the considerable electron velocity shear inherent to cross field electron flow in magnetron-like devices.

Recently we published a preliminary study of a second configuration that effectively circumvents this velocity shear problem.¹⁵ This experiment involves the generation of an essentially monoenergetic rotating electron beam by passing a hollow, nonrotating electron beam through a narrow magnetic cusp. In this manner, the $v_z \times B_z$ force at the center of

the cusp effectively converts the axial beam velocity into rotational velocity downstream of the cusp transition region. If the cusp is symmetric, the downstream beam performs simple axis encircling cyclotron orbits with a gyroradius equal to the radius of the beam on the upstream side of the cusp.¹⁷

To the axial magnetic field about which the beam electrons rotate is added an azimuthally periodic wiggler field, which is primarily radial near the center of the gap, and thus transverse to the electron beam flow. The wiggler field is produced by samarium cobalt magnets placed behind two concentric metal cylinders in such a way that the beam sees only smooth conducting boundaries. The proximity of the conducting walls to the beam also serves to suppress the negative mass instability, which has been used to produce radiation at microwave frequencies in previous studies.^{18,19}

In this paper, we present the first detailed measurements of the operational characteristics of this new circular FEL configuration. Measurements of the effect of the wiggler field on the rotating electron beam are presented, as are radiation spectra obtained for a number of wiggler configurations. Section II of this paper contains a discussion of theoretical considerations, and the experiments are presented in Sec. III. Conclusions are drawn in Sec. IV.

II. THEORETICAL DISCUSSION

A. Electron motion in the axial and wiggler magnetic fields

The general configuration used for these studies is detailed in Fig. 1. Downstream of the cusp transition, the electron orbits have axial (v_{z2}) and azimuthal ($v_{\theta 2}$) velocity components given in terms of the upstream axial velocity (v_{z1}) by

$$v_{z1}^2 = v_{z2}^2 + v_{\theta 2}^2 = v_{z2}^2 + r_c^2 \Omega_{\parallel}^2,$$

where r_c is the cathode radius and $\Omega_{\parallel} = eB_z/m_0\gamma$ is the relativistic electron-cyclotron frequency in the downstream axial magnetic field. Thus, as the magnetic field is raised

^{a)} Permanent address: Institute of Electronics, Academia Sinica, Beijing, People's Republic of China.

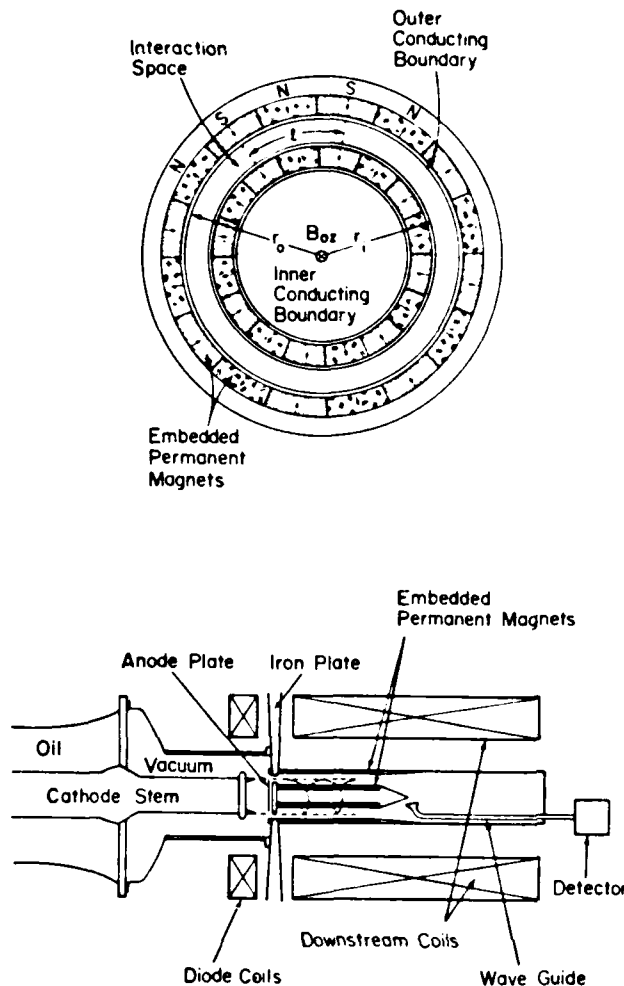


FIG. 1. General experimental configuration.

toward a cutoff value, given by

$$B_{zc} = v_{z1} m_0 \gamma / r_c e,$$

the axial velocity is reduced and electron orbits become fairly tight helices. Beyond the cusp the electrons move in the presence of the combined axial and wiggler magnetic fields, which can be approximated (subject to the condition that $\nabla \cdot \mathbf{B} = \nabla \times \mathbf{B} = 0$ in the region between two conducting boundaries of radii r_0 and r_1) by the expression

$$\mathbf{B} = \hat{r} \frac{B_{0w}}{3} \cos(N\theta) \left[\left(\frac{r}{r_0} \right)^{N-1} + \left(\frac{r}{r_1} \right)^{N+1} \right] \\ \times \left(\frac{r_0}{r_1} \right)^{(N-1)/2N} - \hat{\theta} \frac{B_{0w}}{2} \sin(N\theta) \left[\left(\frac{r}{r_0} \right)^{N-1} \right. \\ \left. - \left(\frac{r}{r_1} \right)^{N+1} \right] \left(\frac{r_0}{r_1} \right)^{(N-1)/2N} + \hat{z} B_z.$$

Here \hat{r} , $\hat{\theta}$, and \hat{z} are unit vectors in the radial, azimuthal, and axial directions, respectively, $N = \pi(r_0 + r_1)/l_0$ is the number of spatial periods around the azimuth, l_0 is the linear periodicity specified midway in the gap, and B_{0w} is the amplitude of the radial component of the field at a distance

$$r = (r_0^{N-1} + r_1^{N+1})^{1/2N},$$

where the azimuthal component vanishes. It is easily seen

that near the center of the gap, the field is primarily radial and that the undulatory $\mathbf{v}_\theta \times \mathbf{B}$ force is the $\pm z$ direction, analogous to the transverse motion of electrons in a linear FEL.

Because of the complicated nature of the combined axial and wiggler fields, a single particle computer simulation program has been used to check that the particle orbits are as desired. Figure 2 shows calculated particle orbits with and without the wiggler fields, results that show clearly that the electron orbits are almost unperturbed in the r - θ plane, and the undulation is primarily axial, as desired. While Fig. 2 shows typical electron orbits for an electron with an initial radial position of precisely 6 cm (the cathode radius), electrons launched at other radial positions within the radial width of the beam do not show significantly different behavior. We have performed these calculations for each of the several wiggler field configurations investigated experimentally, and in no case are the electron orbits unsatisfactory.

B. Excitation of TM waves by the rotating electron beam

In a previous theoretical paper by two of the authors (Y. Yin and G. Bekefi),¹⁶ the radiative process has been identified as the coupling of a "synchronous mode,"²⁰ upshifted in frequency by the wiggler periodicity N :

$$\omega = (l + N)\Omega_{||}$$

to one or more of the TM waves supported by the coaxial conducting boundary system. The radiation frequency is given by

$$\omega = \frac{N\Omega_{||}}{1 - [l\Omega_{||}/\omega_c(l, m)]} = \frac{k_w v_\theta}{1 - (v_\theta/v_{ph})}$$

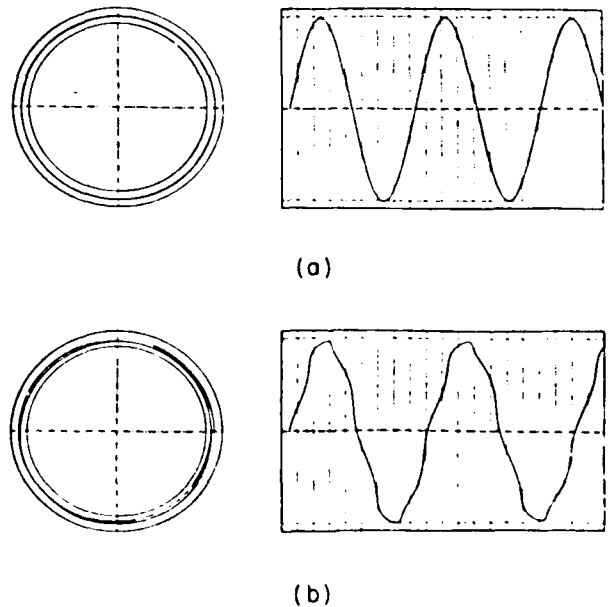


FIG. 2. Calculated particle orbits in the r - θ and r - z planes for an electron injected with $v_z = 0.20c$, $v_\theta = 0.96c$ into the interaction space with (a) $B_z = 1.4$ kG, $B_{0w} = 0$, and (b) $B_z = 1.4$ kG, $B_{0w} = 1.3$ kG.

TABLE I. Computed parameters for an electron ring of radius 6 000 cm rotating in a coaxial waveguide of radii $r_o = 6.509$ cm, $r_i = 5.398$ cm. $\beta_o = 0.968$, $B_{\omega} = 0.75$ kG; $J_o = 1.10$ A cm $^{-2}$; ω is the radiation frequency; ω_i , the temporal growth rate; and η the saturated efficiency.

N	l_o (cm)	m	l	$\omega/2\pi$ (GHz)	$\omega_i \times 10^{-4}$ (rad sec $^{-1}$)	η (%)
6	6.28	1	29	26.8	1.02	19
6	6.28	1	117	94.7	0.21	0.6
12	3.14	1	7	14.6	0.48	14
12	3.14	1	281	225.6	0.014	0.15
12	3.14	2	56	52.3	0.15	0.83
12	3.14	2	232	187.9	0.031	0.05

where $k_\omega = 2\pi/l_o$, $\omega_c(l,m)$ is the cutoff frequency for the TM_{lm} mode, l and m are the azimuthal and radial wavenumbers, respectively, and

$$v_{\theta\omega} = \omega_c(l,m)(r/l)$$

is the azimuthal phase velocity of the rf perturbation. It is interesting to compare this result to the dispersion relation for a conventional linear free-electron laser:

$$\omega = \frac{k_\omega v_o}{[1 - (v_o/c)]}$$

where v_o is now the axial electron velocity.

In the limit where the gap between the two coaxial conducting boundaries is small compared to their mean radius, the cutoff frequency of the TM_{lm} mode may be approximated by the expression

$$\omega_c(l,m) = [m\pi c/r_i(g-1)](1 + \alpha l^2)^{1/2},$$

where $g = r_o/r_i$, and

$$\alpha = \left[\frac{2}{m\pi} \left(\frac{g-1}{g+1} \right) \right]^2.$$

The resultant predicted radiation frequencies for actual experimental parameters discussed in the next section are summarized in Table I. For the specified parameters these are the only unstable interactions predicted by the theory. Because these predicted radiation frequencies are quite sensitive to the values chosen for the applied magnetic field and the electron energy, the values indicated in Table I must be treated as estimates. One important conclusion, however, is that high-frequency radiation is predicted for very low values of the radial mode number m , an important result because the electron beam radial width (about 5 mm) is a sizable fraction of the gap between the two coaxial conductors (13 mm). A comparison between these predicted values and experimental measurements will be made in Sec. IV. The growth rate of the instability ω_i was calculated for the case of an azimuthal current density $J_o = 1.1$ A cm $^{-2}$ in order to satisfy the assumption of a tenuous electron ring, and is also indicated in Table I. In the actual experiments, the azimuthal current density is estimated to be ~ 60 A cm $^{-2}$. In the so-called "single particle, high-gain strong pump" regime² the instability growth rate is proportional to $J_o^{1/2}$, which implies that the experimental growth rates would be

about a factor of 4 higher than those given in the table. The last column of Table I lists the estimated saturation efficiency η caused by phase trapping of electrons in the potential wells of the ponderomotive potential.

III. EXPERIMENTS

A. Apparatus

The general experimental configuration is shown in Fig. 1. A hollow, nonrotating electron beam is field emitted from a 6 cm radius, knife-edge cathode located 7.5 cm upstream of a brass anode plate. A 5 mm wide aperture slit in the anode plate allows a fraction of the electron beam current to pass through the anode plane into the cusp transition region. The cusp magnetic fields are produced by two independently controllable solenoids, and a soft iron plate is used to narrow the axial extent of the cusp transition region. The measured FWHM of the radial component of the magnetic field at the center of the cusp is 4 mm. The $v_z \times B_r$ force acts to convert axial electron velocity upstream of the cusp transition region into azimuthal velocity downstream, with resulting downstream beam parameters of 2 MeV, 1 kA, and 5

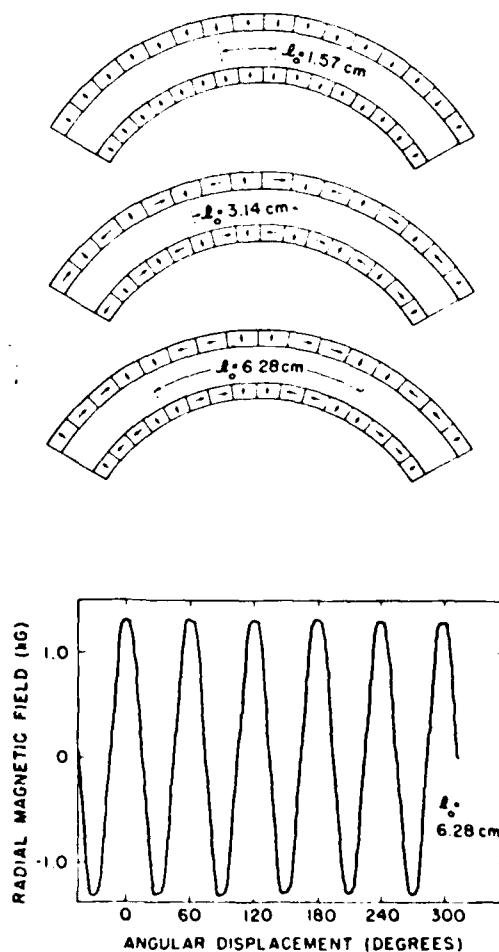


FIG. 3. Arrangement of bar magnets (top), Hall probe measurement of the wiggler field at a radial position $r = 5.92$ cm, as a function of azimuthal angle (bottom).

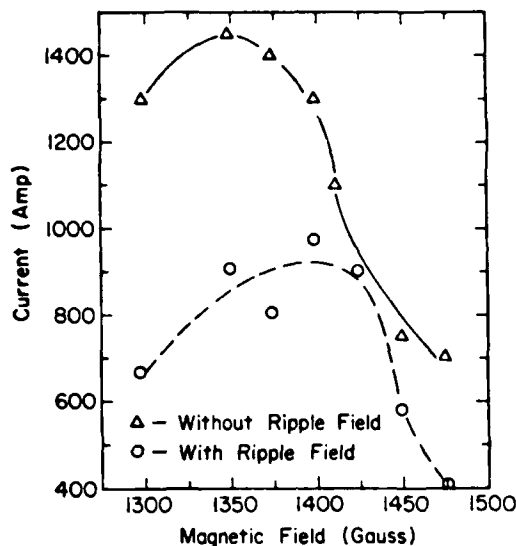


FIG. 4. Peak current exiting the interaction region versus applied cusp axial magnetic field. Results with and without the wiggler magnets are shown.

nsec. Because the cusp reflects all electrons with energies less than a threshold value given by

$$E_{th} = [(m_0c^2)^2 + (ce r_c B)^2]^{1/2} - m_0c^2,$$

the total energy spread in the downstream rotating beam is in the range 1%–3%. The velocity spread caused by local temperature in the beam has been estimated to be about 0.2%.

The downstream beam rotates between two concentric stainless steel cylinders of radii 5.40 and 6.51 cm, respectively. Single turn Rogowski coils can be located at the upstream and/or downstream ends of the interaction region to measure the axial current entering or leaving the wiggler region with or without the wiggler magnets in place. The samarium cobalt magnets used to provide the wiggler field are placed behind the cylinders and held in place by grooved aluminum holders. Typical arrangements of the magnets to achieve various periodicities are shown in Fig. 3. The axial length of the wiggler field is about 20 cm, and the wiggler strength has been varied in the experiments by simply removing some of the magnets from the 6.28 cm wiggler configuration shown in the figure.

The radiation generated in the experiments is measured with a small horn antenna located immediately downstream of the interaction region. The radiated power spectra for various configurations has been measured using a sensitive grating spectrometer,²¹ with gratings available in the range 70–200 GHz. The frequency resolution of the spectrometer is typically $\Delta f/f = 0.02$, and the insertion loss is in the range 3–5 dB.

B. Electron beam measurements

Measurement of the axial electron beam current exiting the interaction region with and without the wiggler magnets in place has been made using a single turn Rogowski coil located immediately downstream of the wiggler region. The results, shown in Fig. 4, indicate that a wiggler field of 1300

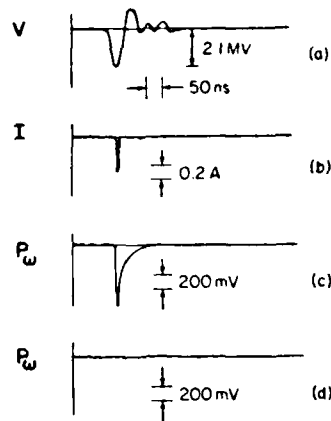


FIG. 5. Oscilloscope waveforms of (a) diode voltage, (b) axial current collected by a 2.24 mm² collector located in the center of the interaction region, (c) microwave signal in T band (91–170 GHz) with wiggler magnets, and (d) microwave signal in T band without wiggler magnets.

G amplitude and $l_0 = 6.28$ cm causes a drop in the beam current of only about 30%. These results confirm that the wiggler field does not have a disastrous effect on the electron orbits, a result consistent with the single particle orbit calculations. In fact, it is likely that the wiggler field acts to remove electrons with badly off-centered orbits from the beam.

Another indication of the nature of the beam current pulse shape has been obtained by placing a small-area axial current collector midway between the conducting cylinders at the axial center of the wiggler field region. A typical current pulse waveform is shown in Fig. 5 and shows dramatically the shortening of the downstream electron beam current pulse duration caused by the reflection of all low-energy electrons at the cusp transition region. This independent measurement of the beam current in the wiggler region also shows that even a relatively strong wiggler field does not disastrously disrupt the rotating electron beam.

C. Radiation measurements

Initial measurements of the radiation produced by the interaction of the rotating electron beam with the wiggler field involved inserting a small horn antenna into the region

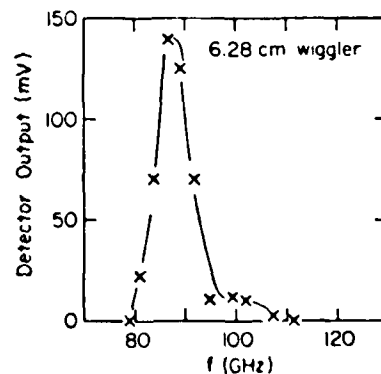


FIG. 6. Radiated power spectrum for $B_w = 1300$ G, $l_0 = 6.28$ cm.

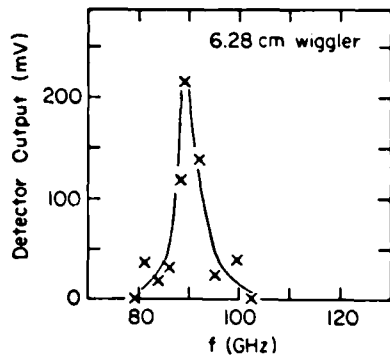


FIG. 7. Radiated power spectrum for $B_{0w} = 800$ G, $l_0 = 6.28$ cm.

immediately downstream of the interaction region and bringing the signal out through a length of Ka-band (22–40 GHz) waveguide. The radiation was then guided through various waveguide filters into calibrated attenuators and detectors. The receiving horn was oriented in such a way as to pick up TM waves in the coaxial conducting boundary system. In these initial experiments, a wiggler field amplitude of 1300 G and a wiggler period of 6.28 cm were used exclusively. Typical signals obtained in T band (91–170 GHz) with and without the wiggler magnets in place are shown in Fig. 5, and show dramatically that high-frequency radiation is only observed when the wiggler field is present. Because of the difficulty in efficiently coupling radiation out of the system, we have only been able to estimate the total radiated power as being in excess of 200 kW. Therefore, a reliable measurement of the electronic efficiency of the experiment is currently unavailable. These results have been reported previously.¹⁵

In these measurements, the horn has been located in various configurations, and the radiated power has been observed to be greatest in the direction of the electron orbits, as expected if the radiation is scattered in the forward direction as in a linear FEL. If the horn is moved to detect radiation in the opposite direction, the observed radiation is down by more than 10 dB. Waveguide cutoff filters were used to obtain a rough idea of the frequency content of the radiation. From these measurements it was determined that most of the radiated power was within N band (74–140 GHz).

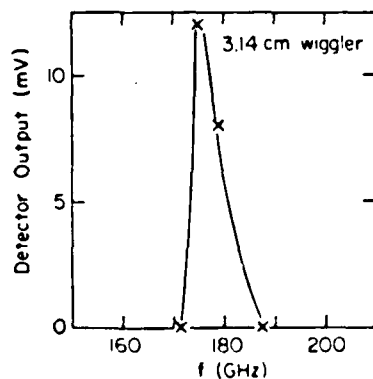


FIG. 8. Radiated power spectrum for $B_{0w} = 1000$ G, $l_0 = 3.14$ cm.

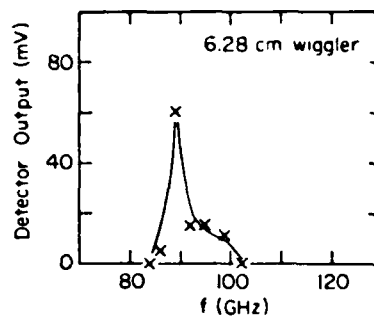


FIG. 9. Radiated power spectrum for $B_{0w} = 450$ G, $l_0 = 6.28$ cm, with inner magnets and inner conducting boundary removed.

Detailed measurements of the radiation spectra have been obtained for a variety of wiggler configurations using the grating spectrometer described previously. These configurations include (a) the 1300 G, 6.28 cm period wiggler first studies (Fig. 3, bottom magnet array), (b) an 800 G, 6.28 cm wiggler (same array, every other magnet removed), (c) a 1000 G, 3.14 cm wiggler (middle magnet array), and (d) a 450 G, 6.28 cm wiggler in which the inner magnets and the inner conducting boundary were removed entirely. Plots of detector output versus frequency are shown for these configurations in Figs. 6–9, respectively.

Several features of these spectra are worthy of mention. First, the radiation observed in all cases is very narrow band, approaching the resolving power of the spectrometer. Second, the center frequency for the 3.14 cm wiggler (175 GHz) is almost exactly double that observed for the 6.28 cm wiggler (88 GHz), and both frequencies are in close agreement with the predictions of theory summarized in Table I. This last result may be just a chance occurrence, as the predictions of the theory are quite sensitive to the values chosen for the electron beam energy and the applied magnetic field.

Although the detector used for these measurements has a sensitivity that does not vary substantially over a frequency range of 10 GHz or so, the detector sensitivity does fall steadily as the frequency of the detected signal is increased. As a result of this trend and the fact that we do not have a calibration source at 175 GHz, even a comparative estimate of the power radiated at this frequency is not possible. If we extrapolate our calibration of the detector response versus frequency from our data in the range 26–135 GHz, where we do have calibration sources, then the radiated power at 175 GHz appears to be roughly comparable to that at 88 GHz.

IV. CONCLUSIONS

The experimental studies indicate that the production of millimeter wave radiation by the interaction of a rotating electron beam with an azimuthally periodic wiggler field has been achieved in a manner consistent with theoretical expectations. The agreement between the measured radiation frequencies and predicted values given in Table I is excellent, but further work will be needed in order to determine if radiation is also produced at the other frequencies indicated. Although the efficiency of conversion of electron beam energy to radiation is currently low (less than 1%), it is not at all clear how efficiently the radiation is currently being coupled

out of the system. In addition, no attempts have been made to minimize wall losses or to optimize the experimental configuration for maximum radiated power. For example, it may be possible to design a system that will be unstable at only one frequency, in contrast to the several unstable frequencies predicted for the present configuration.

We note that in order to achieve frequencies similar to those reported above, the gyrotron²² would require magnetic fields more than an order of magnitude higher. Comparing ω , and η of Table I with those of a gyrotron operating with similar parameters, one finds that the gyrotron has somewhat lower growth rates ω_i , but higher efficiencies η .

Future studies of this novel source of coherent radiation will include attempts to generate submillimeter radiation by reducing the wiggler period and experiments using lower energy and lower current electron beams with longer pulse durations.

ACKNOWLEDGMENTS

It is a pleasure to acknowledge the assistance of A. Bromborsky in performing the orbit calculations.

This work was supported by the U. S. Department of Energy and the Air Force Office of Scientific Research.

¹N. M. Kroll and W. A. McMullin, *Phys. Rev. A* **17**, 300 (1978); P. Sprangle and R. A. Smith, *Phys. Rev. A* **21**, 293 (1980) and references therein.
²P. A. Sprangle, R. A. Smith, and V. L. Granatstein, in *Infrared and Sub-*

millimeter Waves, edited by K. Button (Academic, New York, 1979), Vol. 1, p. 279 and references therein.

³W. A. McMullin and G. Bekefi, *Appl. Phys. Lett.* **39**, 845 (1981).

⁴W. A. McMullin and G. Bekefi, *Phys. Rev. A* **25**, 1826 (1982).

⁵R. C. Davidson and W. A. McMullin, *Phys. Rev. A* **26**, 1997 (1982).

⁶R. C. Davidson and W. A. McMullin, *Phys. Fluids* **26**, 840 (1983).

⁷S. Benson, D. A. G. Deacon, J. N. Eckstein, J. M. J. Madey, K. Robinson, T. I. Smith, and R. Taber, *J. Phys. (Paris) Colloq.* **44**, C1-353 (1983).

⁸M. Billardon, P. Elleaume, J. M. Ortega, C. Bazin, M. Bergher, M. Velghe, Y. Petroff, D. A. G. Deacon, K. E. Robinson, and J. M. J. Madey, *Phys. Rev. Lett.* **51**, 1652 (1983).

⁹J. A. Edighoffer, G. R. Niel, C. E. Hess, T. I. Smith, S. W. Fornaca, and H. A. Schwettman, *Phys. Rev. Lett.* **52**, 344 (1984).

¹⁰T. J. Orzechowski, B. Anderson, W. M. Fawley, D. Prosnitz, E. T. Scharlemann, S. Yarema, D. Hopkins, A. C. Paul, A. M. Sessler, and J. Wurtele, submitted to *Phys. Rev. Lett.*

¹¹G. Bekefi, *Appl. Phys. Lett.* **40**, 578 (1972).

¹²R. C. Davidson, W. A. McMullin, and K. Tsang, *Phys. Fluids* **27**, 233 (1984).

¹³C.-L. Chang, E. Ott, T. M. Antonsen, Jr., and A. T. Drobot, *Phys. Fluids* **27**, 2937 (1984).

¹⁴G. Bekefi, R. E. Shefer, and B. D. Nevins, *Proceedings of the International Conference on Lasers '82*, New Orleans, Louisiana, December 1982, edited by R. C. Powell (STS Press, McLean, Virginia, 1982), p. 136.

¹⁵G. Bekefi, R. E. Shefer, and W. W. Destler, *Appl. Phys. Lett.* **44**, 280 (1984).

¹⁶Y. Z. Yin and G. Bekefi, *Phys. Fluids* **28**, 1186 (1985).

¹⁷M. J. Rhee and W. W. Destler, *Phys. Fluids* **17**, 1574 (1974).

¹⁸W. W. Destler, H. Romero, C. D. Striffler, R. L. Weiler, and W. Namkung, *J. Appl. Phys.* **52**, 2740 (1981).

¹⁹W. W. Destler, R. L. Weiler, and C. D. Striffler, *Appl. Phys. Lett.* **38**, 570 (1981).

²⁰P. Sprangle, *J. Appl. Phys.* **47**, 2935 (1976).

²¹J. Fischer, D. A. Boyd, A. Cavallo, and J. Benson, *Rev. Sci. Instrum.* **54**, 1085 (1983).

²²P. Sprangle and A. T. Drobot, *IEEE Trans. Microwave Theory Tech. MTT-25*, 528 (1977).

A LINEAR GROWTH RATE FLUID FORMULATION FOR LARGE ORBIT,
ANNULAR ELECTRON LAYERS WITH FINITE THICKNESS

W. Lawson and C. D. Striffler

Electrical Engineering Department

and

Laboratory for Plasma and Fusion Energy Studies

University of Maryland

College Park, Maryland 20742

Abstract

The macroscopic fluid equations are used to study the effect of beam thickness on the linear growth rates of a large orbit gyrotron. The chosen equilibrium models a rotating annular electron beam produced by a magnetic cusp. Two methods are used to calculate the growth rates. The analytic approach solves the problem to first order in the ratio of beam thickness to average beam radius and recovers the zero thickness limit. The numeric approach uses complete orthonormal systems comprised of the homogeneous wave equation solutions to calculate the growth rates for beams with arbitrary thicknesses. It is concluded that thick, tenuous beams in resonant systems must be operated near the cutoff of the electromagnetic wave. The decrease in growth rate as the wavelength decreases is attributed to the loss of synchronism in systems where the beam has a spread in its canonical angular momentum.

I. INTRODUCTION

Microwave generation at cyclotron harmonics from large orbit gyrotrons has been studied extensively in recent years. The reduced magnetic field requirements inherent in high harmonic operation make such devices good candidates for high power, high frequency applications. Considerable work has been done on the linear growth rate problem for the large orbit gyrotron configuration. Growth rates have been calculated from single particle,¹⁻⁶ fluid,^{7,8} and Vlasov⁹⁻¹¹ formalisms in a variety of waveguide geometries. Most of these analyses assume that the rotating electron layers have zero radial thickness. In this paper, the macroscopic fluid equations are used to study the effect of beam thickness on the linear growth rates.

A recent experiment¹² has suggested that an efficient way to produce a moderate energy rotating beam is to pass a linearly streaming beam from a thermionic diode through a magnetic cusp.¹³ (Other viable injection schemes include gyro-resonant rf acceleration¹⁴ and tilted Pierce-type guns.¹⁵) The equilibrium selected for this study models the cusp-injected configuration. Although the two previous fluid models cited (Refs. 7 and 8) allow for finite thickness beams, they never consider the case where the beam thickness, axial velocity, and axial electromagnetic wavelength are simultaneously finite. This situation is inherent in thermionic cusp-injected systems and leads to one of the main results of this paper. In Section II, the fluid equilibrium is presented and the perturbed density and velocity terms are calculated. An analytic solution is described in

Section III. The problem is solved to first order in the ratio of the beam thickness to the average beam radius. The result is shown to be in agreement with the single particle result in the appropriate limit. A numeric solution, valid for arbitrary beam thickness, is the subject of Section IV. The results of this study are summarized in Section V.

II. THE FLUID MODEL

A. The Equilibrium Distribution

The beam equilibrium is shown in Fig. 1. It is assumed that the equilibrium results from the passage of a thick, linearly streaming beam through a perfect magnetic cusp (of magnitude B_0). The beam originates on a cathode that has a thickness of $2\Delta r$ and an average radius of r_0 . The electron beam is assumed to be monoenergetic and the self-fields are neglected. Thus, after the cusp, all electrons move on helical orbits about the same gyration axis. The value of each electron's post-cusp axial velocity is a function of the injection radius. Any electrons above a certain critical radius will have insufficient energy and will be reflected. That maximum radius is given by $r_{\max} = (\gamma_0^2 - 1)^{1/2} (m_0 c / e B_0)$ where $\gamma_0 m_0 c^2$ is the equilibrium energy (see Ref. 13).

For this idealized situation, the equilibrium electron velocities are only a function of r :

$$v_{r_0}(r) = 0 \quad (1a)$$

$$v_{\theta_0}(r) = r\Omega_0 \quad (1b)$$

$$v_{z_0}(r) = [c^2(1 - \gamma_0^{-2}) - r^2\Omega_0^2]^{1/2} \quad (1c)$$

where $\Omega_0 = (eB_0)/(m_0\gamma_0)$ and γ_0 are independent of r . Because $v_{r_0} = 0$, the beam will be in equilibrium for any density profile which is only a

function of r . In this paper, two different density functions are considered. The first is a piecewise cubic model and is given by

$$n_o(r) = \begin{cases} \hat{n}_o & |z| < \rho \\ \hat{n}_o \left[3\left(\frac{1-|z|}{1-\rho}\right)^2 - 2\left(\frac{1-|z|}{1-\rho}\right)^3 \right] & \rho < |z| < 1 \\ 0 & |z| > 1 \end{cases} \quad (2)$$

where $z = (r - r_o)/\Delta r$. The parameter ρ is adjustable: $0 < \rho < 1$. A typical density profile and density profile derivative are shown in Fig. 2. The parameter \hat{n}_o is a measure of the volume density of particles. The surface density of particles is given by

$$n_s = \int_{r_o - \Delta r}^{r_o + \Delta r} n_o(r) dr .$$

For the piecewise cubic model, the relationship between the surface and volume densities is given by

$$n_s = \hat{n}_o (1 + \rho) \Delta r . \quad (3)$$

When $\rho = 1$, the distribution function becomes the usual constant density profile:

$$n_o(r) = \begin{cases} \hat{n}_o & |r - r_o| < \Delta r \\ 0 & \text{else} \end{cases} \quad (4)$$

and

$$n_s = \hat{n}_o(2\Delta r) . \quad (5)$$

The piecewise cubic model is used in both the analytic and the numeric problems.

The second density function, used only in the numeric solution, is given by:

$$n_o(r) = \begin{cases} \hat{n}_o \exp[-\hat{z}^2/(1-z^2)] & |z| < 1 \\ 0 & \text{else} \end{cases} \quad (6)$$

where \hat{z} can be adjusted to achieve a desired profile ($0 < \hat{z} < \infty$). It can be shown that $n_o(r)$ is infinitely differentiable and all of its derivatives are continuous everywhere. The extrema of $n'_o(r)$ can be found by calculus to be

$$z_{m\pm} = \pm \left\{ \frac{(1 - \hat{z}^2) + [(1 - \hat{z}^2)^2 + 3]^{1/2}}{3} \right\}^{1/2} . \quad (7)$$

Notice that $z_{m\pm} \rightarrow \pm 1$ as $\hat{z} \rightarrow 0$. In fact, this distribution approaches the constant distribution as $\hat{z} \rightarrow 0$. It is more practical, however, to use the first distribution when approximating the uniform case.

For the second distribution, the surface and volume densities are related by

$$n_s = \hat{n}_0 \Delta r [\hat{z}^2 e^{-\hat{z}^2} \Gamma(1/2) U(3/2, 2, \hat{z}^2)] \quad (8)$$

where $U(\nu, \mu, x)$ is a degenerate hypergeometric function,¹⁶ and $\Gamma(x)$ is the Gamma Function. It can be shown that $\hat{z}^2 U(3/2, 2, \hat{z}^2) \rightarrow \Gamma(3/2)^{-1}$ as $\hat{z}^2 \rightarrow 0$ which means that $n_s \rightarrow \hat{n}_0 (2\Delta r)$ as $\hat{z}^2 \rightarrow 0$. Profiles of $n_0(r)$ and $n'_0(r)$ are shown in Fig. 3 for $\hat{z} = 0.125$, $\hat{z} = 1.0$, and $\hat{z} = 2.0$. The curves are normalized so that $\int_{-1}^{+1} n_0(z) dz = 2$. The curves support the claim that the constant density profile is approached as $\hat{z} \rightarrow 0$.

The natural definition of the beam thickness for the numerical routine is $z = 1$, because the density distributions are identically zero when $|z| > 1$. However, as suggested by Fig. 3, this definition may not be appropriate when comparing results for different parameters. Three appropriate measures of the effective beam thickness are: (1) $n_s / (2\Delta r \hat{n}_0)$, (2) the location of the (negative) peak of n'_0 , and (3) the Full Width Half Maximum (FWHM). For the piecewise cubic model, these measures have the common value $z = (1 + \rho)/2$. For the smooth model, all three measures are different. The first is given by Eq. (8), the second by Eq. (7), and the third by

$$z = \left[\frac{\log_e 2}{\hat{z}^2 + \log_e 2} \right]^{1/2} .$$

In this paper, we use the first measure to denote the effective thickness of the E layer.

B. The Perturbed Fluid Equations

The fluid momentum equation is

$$\partial_t (\gamma \vec{v}) + \langle \vec{v}, \vec{\nabla} \rangle (\gamma \vec{v}) = - \frac{e}{m_0} (\vec{E} + \vec{v} \times \vec{B}) \quad (9)$$

where $\langle \cdot, \cdot \rangle$ denotes the usual inner product. This equation can be linearized about the equilibrium specified in Eq. (1) and Fourier analyzed to yield

$$\tilde{v}_{r1} = \frac{e}{m_0 \gamma_0 D_\ell^2} \{ \psi_\ell [-i\tilde{E}_r + \beta_{\theta_0} (-ic\tilde{B}_z) - \beta_{z_0} (-ic\tilde{B}_\theta)] + \Omega_0 (\tilde{E}_\theta + \beta_{z_0} c\tilde{B}_r) \} \quad (10a)$$

$$i\tilde{v}_{\theta 1} = \frac{e}{m_0 \gamma_0 \psi_\ell} [(1 - \beta_{\theta_0}^2) \tilde{E}_\theta + \beta_{z_0} c\tilde{B}_r - \beta_{\theta_0} \beta_{z_0} \tilde{E}_z] + \frac{\Omega_0}{\psi_\ell} \tilde{v}_{r1} \quad (10b)$$

$$i\tilde{v}_{z1} = \frac{e}{m_0 \gamma_0 \psi_\ell} [-\beta_{\theta_0} \beta_{z_0} \tilde{E}_\theta - \beta_{\theta_0} c\tilde{B}_r + (1 - \beta_{z_0}^2) \tilde{E}_z] - \frac{\Omega_0}{\psi_\ell} \frac{\beta_{\theta_0}}{\beta_{z_0}} \tilde{v}_{r1} \quad (10c)$$

for $D_\ell^2 = \psi_\ell^2 - \Omega_0^2$ and $\psi_\ell(r) = \omega - \ell\Omega_0 - k_z v_{z_0}(r)$.

The fluid continuity equation

$$\partial_t n + \langle \vec{v}, \vec{\nabla} n \rangle = 0 \quad (11)$$

can also be linearized and Fourier analyzed to yield

$$r(i\tilde{n}_1) = \psi_\ell^{-1} \{ \partial_r (r n_o \tilde{v}_{r1}) + n_o [\ell (i\tilde{v}_{\theta 1}) + k_z r (i\tilde{v}_{z1})] \} . \quad (12)$$

In the derivation of the above results, all variables were written as

$$\chi(\vec{x}, t) = \chi_o(r) + \tilde{\chi}_1(r) \exp[i(k_z z + \ell\theta - \omega t)]$$

and $|\tilde{\chi}_1(r)| \ll |\chi_o(r)|$ was assumed. Equations (10) and (12) express the perturbed velocity and density in terms of the equilibrium quantities and the electromagnetic (EM) fields. These equations are the starting points for both the analytic and numeric solutions. The differences in the two solutions arise from the procedures used to close these equations.

III. THE ANALYTIC SOLUTION

A. The Thin Beam Approximation

The assumption that yields the analytic solution is that the beam thickness is small compared to the average beam radius. That is, the thin beam must satisfy:

$$x_0 = \frac{\Delta r}{r_0} \ll 1. \quad (13)$$

The fluid equations are expanded about the equilibrium radius in the coordinate x , defined by the transformation $x = r/r_0 - 1$. Throughout the course of this analysis, many quantities will be linearized in x , resulting in additional constraints on the size of x_0 . Unfortunately, it turns out that the solutions will be valid for reasonable values of x_0 only in a few special cases. Nonetheless, this method yields a good deal of information about the linear growth rate problem as will be demonstrated in the remainder of the section.

Two critical limitations in the expansion parameter come from the linearization of $v_{z_0}(r)$. To first order in x ,

$$v_{z_0}(r) = \hat{v}_{z_0} [1 - x(\hat{v}_{\theta_0}/\hat{v}_{z_0})^2] = \hat{v}_{z_0} (1 - \tau x) \quad (14)$$

where \hat{v}_{θ_0} and \hat{v}_{z_0} are the azimuthal and axial velocities at the center radius r_0 , respectively, and $\tau = (\hat{v}_{\theta_0}/\hat{v}_{z_0})^2$. The worst case for this expansion is at $|x| = x_0$, resulting in the criteria $x_0 \ll (\hat{v}_{z_0}/\hat{v}_{\theta_0})^2$.

Because large orbit gyrotrons are normally designed to extract azimuthal energy, it is desirable to have $\hat{v}_z / \hat{v}_\theta$ as small as possible, causing a further restriction on the allowed size of x_0 .

The zero thickness linear growth rate solution that we compare our results to assumes a resonance condition, for which the frequencies of the beam mode and an empty waveguide mode coincide. It also requires a synchronous condition: the frequency of the actual electromagnetic mode is assumed to be near the frequency of the beam mode. The analysis in this section deals only with the synchronous case and the empty waveguide mode does not enter into the picture directly. Still, the resonant limit will be recovered for the proper axial wave numbers (k_z).

The concept of synchronism is somewhat ambiguous for the thin beam model, because the phase velocity of the beam perturbation is in general a function of radius:

$$\omega_0(r) = \ell\Omega_0 + k_z v_z(r) . \quad (15)$$

For simplicity in the analysis, it is assumed that the synchronous layer corresponds to $r = r_0$. This assumption does not affect the analysis in any way, it simply serves as a reference point when comparing this method to others. For $\psi_\ell(r) = \omega - \omega_0(r)$, the linear expansion is

$$\psi_\ell(r) = \hat{\psi}_\ell + x k_z r_0 \Omega_0 \frac{\hat{v}_\theta}{\hat{v}_z} = \hat{\psi}_\ell + x T \Omega_0 \quad (16)$$

where $\hat{\psi}_\ell = \omega - \omega_0(r_0)$ and $T = k_z r_0 \hat{v}_\theta / \hat{v}_z$. Thus, the synchronous limit is defined by $\hat{\psi}_\ell \rightarrow 0$. The expansion of ψ_ℓ requires that

$x_0 \ll (\hat{v}_{z_0} / \hat{v}_{\theta_0}) (\hat{\psi}_\ell / \Omega_0) (k_z r_0)^{-1}$. It was noted previously that $\hat{v}_{z_0} / \hat{v}_{\theta_0}$ is designed to be small. Furthermore, it is known that $\hat{\psi}_\ell \ll \Omega_0$ for tenuous beams.⁵ Although the method considered in this section is valid for somewhat higher beam densities, $\hat{\psi}_\ell / \Omega_0$ will be small in general and the available range for x_0 will be diminished further. Taking $k_z < r_0^{-1}$ will lessen the severity of this restriction. Indeed, at cutoff there is no restriction at all. When $k_z = 0$, the beam frequency is independent of r and the electromagnetic wave can be synchronized with the entire beam.

In the following analysis, other expansions in x are performed. However, the linear coefficients of those expansions are not inherently large and the restrictions imposed by them are not calculated. Still, it will be demonstrated later that the solution is very sensitive to small changes in certain terms. Thus, the error introduced by one of these "accurate" expansions can change the answer dramatically. The uncertainties discussed above make it difficult to predict the maximum beam thickness that yields reliable growth rates. Nonetheless, the method is accurate in the zero thickness limit and should be able to predict the initial growth rate trends as x_0 increases from zero.

B. Method of Solution

The solution is achieved by integrating several components of Maxwell's equations from $r_0 - \Delta r$ to $r_0 + \Delta r$. The resulting equations express the "jump" in the EM fields across the beam in terms of integrals of the source terms and the EM fields in the beam region. In order to perform the integrals, the EM fields must be evaluated to first order in x_0 in the region $|x| < x_0$. This is done in Section 1. The source

integrals are evaluated in Section 2. In Section 3, the formal solution is given. Properties of the solution are discussed in Section II.C.

1. The Field Expansions

Outside the beam region, the homogeneous wave equations are valid and the axial fields can be written

$$\tilde{E}_z = \begin{cases} \frac{J_\ell(y)}{J_\ell(y_-)} \tilde{E}_z^- & 0 < r < r_- \\ \frac{P_\ell(y, y_w)}{P_\ell(y_+, y_w)} \tilde{E}_z^+ & r_+ < r < r_w \end{cases} \quad (17a)$$

and

$$c\tilde{B}_z = \begin{cases} \frac{r_- J_\ell(y)}{y_- J'_\ell(y_-)} (\partial_r c\tilde{B}_z)^- & 0 < r < r_- \\ \frac{r_+ Q_\ell(y, y_w)}{y_+ S_\ell(y_+, y_w)} (\partial_r c\tilde{B}_z)^+ & r_+ < r < r_w \end{cases} \quad (17b)$$

for

$r_\pm = r_0 \pm \Delta r$, $\tilde{E}_z^\pm = E_z(r_\pm)$, $(\partial_r c\tilde{B}_z)^\pm = (\partial_r c\tilde{B}_z)|_{r_\pm}$, $\xi^2 = [(\omega/c)^2 - k_z^2]$, $y = r\xi$, $y_\pm = y(r_\pm)$, and where $P_\ell - S_\ell$ are cross products of Bessel functions:¹⁷

$$P_l(a,b) = J_l(a)Y_l(b) - Y_l(a)J_l(b) \quad (18a)$$

$$Q_l(a,b) = J_l(a)Y'_l(b) - Y_l(a)J'_l(b) \quad (18b)$$

$$R_l(a,b) = J'_l(a)Y_l(b) - Y'_l(a)J_l(b) \quad (18c)$$

$$S_l(a,b) = J'_l(a)Y'_l(b) - Y'_l(a)J'_l(b) \quad (18d)$$

When $|x| > x_0$, $\vec{J} = 0$, so \vec{E}_\perp and $c\vec{B}_\perp$ can be found from Maxwell's Equations given Eq. (17).

In the region $|x| < x_0$, the fields are expanded about the values of the fields at the edges of the beam (r_\pm). The piecewise cubic beam density profile is used so that the values of the fields and their derivatives are continuous at the beam edges. Thus, the limiting values of the homogeneous fields can be used in the expansions. Let χ represent any EM field component. For the fields to be accurate to first order in x_0 , it is necessary to approximate χ by a cubic:

$$\begin{aligned} \chi_c(r) = & \left[\chi^0 - \frac{\Delta r}{2} \left(\frac{d\chi}{dr} \right)^\Delta \right] + z \left[\frac{3}{2} \chi^\Delta - \frac{\Delta r}{2} \left(\frac{d\chi}{dr} \right)^0 \right] \\ & + z^2 \left[\frac{\Delta r}{2} \left(\frac{d\chi}{dr} \right)^\Delta \right] + z^3 \left[\frac{\Delta r}{2} \left(\frac{d\chi}{dr} \right)^0 - \frac{1}{2} \chi^\Delta \right] \end{aligned} \quad (19)$$

where $\chi^{\left\{ \begin{smallmatrix} 0 \\ \Delta \end{smallmatrix} \right\}} = (\chi_+ \pm \chi_-)/2$, $\chi_\pm = \chi(r_\pm)$, etc. By considering Taylor series expansions about r_\pm , it can be seen that $|\chi - \chi_c| = O(x_0^2)$ when

$|z| < 1$. Furthermore, Eq. (19) insures that $d\chi/dr$ is continuous on the same interval.

2. The Source Integrals

To lowest order in x_0 , the jump in the perturbed density across the beam is (see Eq. 12)

$$\begin{aligned} \frac{ie}{\epsilon_0} \int_{r_0-\Delta r}^{r_0+\Delta r} (r\tilde{n}_1) dr &= \frac{T\Omega_0}{\psi_\ell^2} \left(\frac{e}{\epsilon_0}\right) \int_{r_0-\Delta r}^{r_0+\Delta r} n_0(1+x)\tilde{v}_{r_1} dr \\ &+ \frac{\ell}{\psi_\ell} \left(\frac{ie}{\epsilon_0}\right) \int_{r_0-\Delta r}^{r_0+\Delta r} n_0\left(1-x\frac{T\Omega_0}{\psi_\ell}\right)\tilde{v}_{\theta_1} dr \\ &+ \frac{k_z r_0}{\psi_\ell} \left(\frac{ie}{\epsilon_0}\right) \int_{r_0-\Delta r}^{r_0+\Delta r} n_0\left[1+x\left(1-\frac{T\Omega_0}{\psi_\ell}\right)\right]\tilde{v}_{z_1} dr . \end{aligned} \quad (20a)$$

Because $\tilde{J}_1 = -en_0\tilde{v}_1 - en_1\tilde{v}_0$,

$$\frac{i}{\epsilon_0 c} \int_{r_0-\Delta r}^{r_0+\Delta r} \tilde{J}_{\theta_1} dr = -\frac{1}{c} \left(\frac{ie}{\epsilon_0}\right) \int_{r_0-\Delta r}^{r_0+\Delta r} n_0\tilde{v}_{\theta_1} dr - \frac{\Omega_0}{c} \left(\frac{ie}{\epsilon_0}\right) \int_{r_0-\Delta r}^{r_0+\Delta r} (r\tilde{n}_1) dr \quad (20b)$$

and

$$\begin{aligned}
\frac{1}{\epsilon_0 c} \int_{r_0 - \Delta r}^{r_0 + \Delta r} (r \tilde{J}_{z_1}) dr &= \frac{\hat{v}_{z_0}}{c} \left(\frac{T\Omega_0}{\hat{\psi}_l} + \frac{\tau}{\hat{\psi}_l} \right) \left(\frac{e}{\epsilon_0} \right) \int_{r_0 - \Delta r}^{r_0 + \Delta r} n_0 (1 + x) \tilde{v}_{r_1} dr \\
- \frac{\hat{v}_{z_0}}{c} \frac{l}{\hat{\psi}_l} \left(\frac{ie}{\epsilon_0} \right) \int_{r_0 - \Delta r}^{r_0 + \Delta r} n_0 \left[1 - x \left(\frac{T\Omega_0}{\hat{\psi}_l} + \tau \right) \right] \tilde{v}_{\theta_1} dr \\
- \frac{\hat{v}_{z_0}}{c} \frac{k_z r_0}{\hat{\psi}_l} \left(\frac{ie}{\epsilon_0} \right) \int_{r_0 - \Delta r}^{r_0 + \Delta r} n_0 \left[1 - x \left(\frac{T\Omega_0}{\hat{\psi}_l} + \tau - 1 \right) \right] \tilde{v}_{z_1} dr \\
- \frac{r_0}{c} \left(\frac{ie}{\epsilon_0} \right) \int_{r_0 - \Delta r}^{r_0 + \Delta r} n_0 (1 + x) \tilde{v}_{z_1} dr
\end{aligned} \tag{20c}$$

again to lowest order in x_0 . Therefore, evaluation of the source integrals requires the evaluation of integrals of the form $\int_{r_0 - \Delta r}^{r_0 + \Delta r} n_0 (1 + Fx) \tilde{v}_1 dr$ where F is some constant.

From the above comment and Eq. (10), it can be seen that all the source integrals can be expressed in terms of integrals of the form $\int_{r_0 - \Delta r}^{r_0 + \Delta r} n_0 (1 + Fx) \chi dr$ where χ again denotes a field component. The cubic approximation for χ can be used to show that

$$\begin{aligned}
&\int_{r_0 - \Delta r}^{r_0 + \Delta r} n_0(r) (1 + Fx) \chi(r) dr \\
&= n_s \left\{ \chi^0 - \frac{x_0}{3} \left[1 + \frac{1}{10} (1 - \rho) (3 + 2\rho) \right] r_0 \left(\frac{d\chi}{dr} \right)^\Delta \right. \\
&\quad \left. + \frac{2x_0}{5} \left[1 + \frac{1}{56} (1 - \rho) (31 + 19\rho - 5\rho^2 - 3\rho^3) \right] F \chi^\Delta \right\}
\end{aligned} \tag{21}$$

to first order in x_0 . Even though the continuity of dn_0/dr was required in the derivation of Eq. (19), the source integrals are continuous functions of ρ [their dependence is given by Eq. (21)]. In the remainder of this paper, ρ is set to one for convenience and only the constant distribution of Eq. (4) is considered.

In Appendix A, Eqs. (10) and (21) are used to find standard integrals of the perturbed fluid velocity in terms of the equilibrium beam quantities and the fields (and their derivatives) at the beam edges. Thus, from Eqs. (20) and (A.1), the integrals of the perturbed sources across the beam are known in terms of the electromagnetic fields at the beam edges.

3. The Jump Conditions and The Formal Solution

Six of the eight components of Maxwell's equations contain derivatives of the electromagnetic fields with respect to r and can be integrated across the beam. The results to first order in x_0 are:

$$-i\tilde{E}_r^\Delta + x_0(-i\tilde{E}_r^0 + \lambda\tilde{E}_\theta^0 + k_z r_0 \tilde{E}_z^0) - \frac{1}{2r_0} \frac{1e}{\epsilon_0} \int_{r_0-\Delta r}^{r_0+\Delta r} (r\tilde{n}_1) dr = 0 \quad (22a)$$

$$-ic\tilde{B}_\theta^\Delta + x_0(-ic\tilde{B}_\theta^0 + \frac{\omega r_0}{c} \tilde{E}_z^0 - \lambda c\tilde{B}_r^0) + \frac{1}{2r_0} \frac{1}{\epsilon_0 c} \int_{r_0-\Delta r}^{r_0+\Delta r} r\tilde{J}_z dr = 0 \quad (22b)$$

$$-ic\tilde{B}_z^\Delta - x_0(\frac{\omega r_0}{c} \tilde{E}_\theta^0 + k_z r_0 c\tilde{B}_r^0) - \frac{1}{2} \frac{1}{\epsilon_0 c} \int_{r_0-\Delta r}^{r_0+\Delta r} \tilde{J}_\theta dr = 0 \quad (22c)$$

$$c\hat{B}_r^\Delta + x_0 [c\hat{B}_r^0 - \ell(-ic\hat{B}_\theta^0) - k_z r_0 (-ic\hat{B}_z^0)] = 0 \quad (22d)$$

$$\hat{E}_\theta^\Delta + x_0 [\hat{E}_\theta^0 + \ell(-iE_r^0) + \frac{\omega r_0}{c} (-ic\hat{B}_z^0)] = 0 \quad (22e)$$

$$\hat{E}_z^\Delta + x_0 [k_z r_0 (-i\hat{E}_r^0) - \frac{\omega r_0}{c} (-ic\hat{B}_\theta^0)] = 0 \quad (22f)$$

Out of the six jump conditions, three contain source terms and three do not. The three sourceless equations are linearly dependent as are the three equations with sources. It can be shown that

$$-\left(\frac{\omega r_0}{c}\right) \times \text{Eq. (22a)} + (k_z r_0) \times \text{Eq. (22b)} - \ell \times \text{Eq. (22c)} \equiv 0$$

$$\left(\frac{\omega r_0}{c}\right) \times \text{Eq. (22d)} + (k_z r_0) \times \text{Eq. (22e)} - \ell \times \text{Eq. (22f)} \equiv 0 \ .$$

The four equations (22b), (22c), (22e), and (22f) form a linearly independent set even if $\ell = 0 = k_z$. Consequently, they are the ones used in the analysis.

Because E_\perp and cB_\perp are given in terms of \hat{E}_z , $c\hat{B}_z$, and their derivatives when $|x| > x_0$, Eq. (17) reveals that there are only four unknowns. Consequently, there are the same number of equations as unknowns and the system of equations is well defined. To simplify the $x_0 = 0$ limit, the four unknowns are chosen to be:

$$u_1 = (\hat{E}_z/r)^0 \quad (23a)$$

$$u_2 = (\hat{E}_z/r)^\Delta \quad (23b)$$

$$u_3 = -i(\partial_r c\hat{B}_z)^0 \quad (23c)$$

$$u_4 = -i(\partial_r c\hat{B}_z)^\Delta \quad (23d)$$

Defining the normalized wave admittances

$$\alpha_e^\pm = (r\partial_r \hat{E}_z)^\pm / (\hat{E}_z)^\pm \quad (24a)$$

and

$$\alpha_b^\pm = (-ic\hat{B}_z)^\pm / (-ir\partial_r c\hat{B}_z)^\pm \quad (24b)$$

and using Eqs. (17) and (24) it follows that

$$\begin{aligned} \alpha_e^+ &= [y_+ R_\ell(y_+, y_w)] / P_\ell(y_+, y_w) & \alpha_e^- &= [y_- J'_\ell(y_-)] / J_\ell(y_-) \\ \alpha_b^+ &= Q_\ell(y_+, y_w) / [y_+ S_\ell(y_+, y_w)] & \alpha_b^- &= J_\ell(y_-) / [y_- J'_\ell(y_-)] \end{aligned} \quad (25)$$

The thin beam geometry parameters are defined to be (in the usual notation):

$$\begin{aligned}
 \alpha_e^o &= \frac{1}{2} (\alpha_e^+ + \alpha_e^-) & \alpha_b^o &= \frac{1}{2} (\alpha_b^+ + \alpha_b^-) \\
 \alpha_e^\Delta &= \frac{1}{2} (\alpha_e^+ - \alpha_e^-) & \alpha_b^\Delta &= \frac{1}{2} (\alpha_b^+ - \alpha_b^-) .
 \end{aligned}
 \tag{26}$$

These expressions can be expanded in x_o to reveal their limiting behavior:

$$\begin{aligned}
 \alpha_e^o &= \frac{1}{2} \left[\frac{y_o \hat{R}}{\hat{P}} + \frac{y_o J'_\ell(y_o)}{J_\ell(y_o)} \right] + x_o \left[\frac{J_\ell(y_w)}{\pi J_\ell(y_o) \hat{P}} \right] \left[\frac{y_o \hat{R}}{\hat{P}} + \frac{y_o J'_\ell(y_o)}{J_\ell(y_o)} \right] \\
 \alpha_e^\Delta &= - \left[\frac{J_\ell(y_w)}{\pi J_\ell(y_o) \hat{P}} \right] + x_o \left\{ \ell^2 - y_o^2 - \frac{1}{2} \left\{ \left(\frac{y_o \hat{R}}{\hat{P}} \right)^2 + \left[\frac{y_o J'_\ell(y_o)}{J_\ell(y_o)} \right]^2 \right\} \right\} \\
 \alpha_b^o &= \frac{1}{2} \left[\frac{\hat{Q}}{y_o \hat{S}} + \frac{J_\ell(y_o)}{y_o J'_\ell(y_o)} \right] + x_o \left[\frac{-J'_\ell(y_w)}{\pi y_o^2 J'_\ell(y_o) \hat{S}} \right] (\ell^2 - y_o^2) \left[\frac{\hat{Q}}{y_o \hat{S}} + \frac{J_\ell(y_o)}{y_o J'_\ell(y_o)} \right] \\
 \alpha_b^\Delta &= \left[\frac{J'_\ell(y_w)}{\pi y_o^2 J'_\ell(y_o) \hat{S}} \right] + x_o \left\{ 1 - \frac{1}{2} (\ell^2 - y_o^2) \left\{ \left(\frac{\hat{Q}}{y_o \hat{S}} \right)^2 + \left[\frac{J_\ell(y_o)}{y_o J'_\ell(y_o)} \right]^2 \right\} \right\}
 \end{aligned}
 \tag{27}$$

for $\hat{P} = P_\ell(y_o, y_w)$, etc.

Maxwell's equations can be used to find all the fields to first order in x_o in terms of $u_1 - u_4$. For example, the average fields (χ^o) are

$$c\tilde{B}_r^o = (\ell \frac{\omega}{c} u_1 - k_z u_3)/\xi^2 \quad (28a)$$

$$\tilde{E}_\theta^o = (-\ell k_z u_1 + \frac{\omega}{c} u_3)/\xi^2 \quad (28b)$$

$$\tilde{E}_z^o = r_o u_1 + x_o r_o u_2 \quad (28c)$$

$$-i\tilde{E}_r^o = [k_z (\alpha_e^o u_1 + \alpha_e^\Delta u_2) - \ell \frac{\omega}{c} (\alpha_b^o u_3 + \alpha_b^\Delta u_4)]/\xi^2 \quad (28d)$$

$$-ic\tilde{B}_\theta^o = [\frac{\omega}{c} (\alpha_e^o u_1 + \alpha_e^\Delta u_2) - \ell k_z (\alpha_b^o u_3 + \alpha_b^\Delta u_4)]/\xi^2 \quad (28e)$$

$$-ic\tilde{B}_z^o = r_o (\alpha_b^o + x_o \alpha_b^\Delta) u_3 + r_o (\alpha_b^\Delta + x_o \alpha_b^o) u_4 \quad (28f)$$

The difference fields (χ^Δ) can be found from the average fields in Eq. (28) by interchanging u_1 and u_2 and by interchanging u_3 and u_4 (e.g. $\tilde{E}_z^\Delta = r_o u_2 + x_o r_o u_1$). The field derivatives $(d\chi/dr)^\Delta$ can also be found in terms of u_1 — u_4 directly from Maxwell's Equations.

At this point the solution is complete, however, the expressions are too cumbersome to assemble into one equation. Instead, the equations are built-up as follows. The geometry parameters are given in terms of the system configuration, the wave numbers ℓ and k_z , and the unknown frequency ω [Eq. (27)]. The EM fields are given in terms of u_1 — u_4 via the geometry parameters [Eq. (28)]. The sources integrals can be found in terms of u_1 — u_4 via the EM fields [Eqs. (20) and (A.1)]. Finally, the

jump conditions can be found (once again in terms of $u_1 - u_4$) from the EM fields and the source integrals [Eq. (22)].

C. Properties of the Solution:

When $x_0 = 0$, two of the jump conditions yield $\hat{E}_z^\Delta = 0 = u_2$ [Eq. (22f)] and $\hat{E}_\theta^\Delta = 0 = u_4$ [Eq. (22e)]. The remaining two equations then can be solved to find $\hat{\psi}_\ell$ and the ratio u_1/u_3 . To lowest order in $\hat{\psi}_\ell$, the equations yield the dispersion relation

$$\hat{\psi}_\ell^2 \alpha_b^\Delta \alpha_e^\Delta + \frac{\nu}{\gamma_0} (\alpha_e^\Delta \Omega_0^2 - \alpha_b^\Delta \Omega_*^2) = 0. \quad (29)$$

With the aid of Eq. (27), we can show that this expression agrees with the single particle result.⁵

The fluid method has expanded the single particle result in three dimensions: (1) axial wave number k_z , (2) beam density n_s , and (3) beam thickness Δr . Below, the properties of the growth rate solutions are examined as a function of these three variables.

Figure 4(a) demonstrates the effect of beam density on the growth rate Γ for a zero thickness beam at a resonant point ($\hat{\psi}_\ell = \omega_r + i\Gamma$). The parameters for this case are $\ell = 7$, $n_r = 1$ (first radial mode), $r_0 = 0.06$ m, $r_w = 0.0865$ m, $\hat{\beta}_\theta = 0.85$, $\hat{\beta}_z = 0.5$, and $k_z = 0$ (r_w is adjusted for cutoff). Because $\Gamma \propto n_s^{1/3}$ in the tenuous limit,⁵ the plots are normalized by $n_s^{1/3}$. Thus, the "tenuous" limit is valid for the densities where the curves are relatively flat. Consequently, the tenuous limit typically demands that $n_s < 10^{12} \text{ m}^{-2}$ in order for the lowest term in $\hat{\psi}_\ell$ to be dominant.

Self-fields introduce another kind of tenuous limit, outside of which the space-charge effects contribute significantly to the equilibrium and (perhaps) the growth rates. Because the self-fields have been neglected by this analysis, there is an unknown upper limit on the allowable beam density and the high density results may not be valid.

Figure 4(b) shows Γ for the system parameters of Fig. 4(a) midway between resonant points ($k_z = 66.11 \text{ m}^{-1}$). For this non-resonant case, $\Gamma \propto n_s^{1/2}$ in the tenuous regime and the plots are normalized appropriately. The tenuous limit again appears to be valid out to $n_s \sim 10^{12} \text{ m}^{-2}$.

Figure 5(a) shows a plot of growth rate as a function of k_z for a zero thickness beam. The parameters are $\ell = 11$, $r_o = 0.06 \text{ m}$, $r_w = 0.10 \text{ m}$, $\hat{\beta}_{\theta_o} = 0.85$, $\hat{\beta}_{z_o} = 0.5$, and $n_s = 10^8 \text{ m}^{-2}$. The corresponding beam line and empty waveguide curves are plotted in Fig. 5(b). The beam line intercepts the lowest three empty waveguide modes. The squares in Fig. 5(a) indicate the growth rates for the six resonant points and the one non-resonant point midway between the resonances as calculated by the single particle formula. The fluid result is indicated by the line. The growth rates drop abruptly to zero at synchronous points below the empty waveguide curves. Above the dispersion curves, the growth rates drop off rapidly to small but finite values. At synchronous points sufficiently above the lowest two waveguide modes, the growth rates again become zero, resulting in five frequency bands of instability.

As previously claimed, the fluid model agrees with the single particle model as $n_s \rightarrow 0$, both on and off resonance. It is interesting to note that the thin beam model's solution is independent of ρ at $x_o = 0$. Hence, the

particular shape of the density function is not important as $x_0 \rightarrow 0$. This is readily seen by setting $x_0 = 0$ in Eq. (21) and recalling that the source integrals can all be written in terms of that equation. The growth rate does depend on the surface density n_s and the EM fields at r_0 , as though the fluid momentum equation was simply evaluated at the equilibrium radius.

Figure 6 shows ψ_ℓ as a function of beam thickness for a system whose parameters are $\ell = 7$, $n_r = 1$, $r_0 = 0.06$ m, $r_w = 0.09$ m, $\hat{\beta}_\theta = 0.85$, $\hat{\beta}_z = 0.5$, $k_z = 0$, and $n_s = 10^8$ m⁻². Except for the wall radius, the parameters of Figs. 4(a) and Fig. 6 are the same. The wall radius is larger in the latter case so that the system is not resonant at $k_z = 0$. Cutoff is chosen so that the entire beam is synchronous with the EM wave. Two curves are plotted in the figure. One curve corresponds to the solution when the geometry parameters ($\alpha_e^0 - \alpha_b^\Delta$) are given by Eqs. (25) and (26) (exact) and the other curve corresponds to the solution when the geometry parameters are given by Eq. (27) (linear expansion). In this example, the restriction due to the geometry parameters is $x_0 \sim 0.02$.

Unfortunately, the restriction imposed by the geometry parameters is even more severe at resonance points. This can be seen by examining Eq. (27). Consider the solution near a TE resonant point. When $x_0 \rightarrow 0$, $\alpha_b^\Delta \rightarrow 0$ as $\hat{\psi}_\ell \rightarrow 0$. Thus, the linear term becomes the dominant term for extremely small values of x_0 . The solution is very sensitive to changes in α_b^Δ and the exact and linear solutions diverge rapidly as x_0 increases.

In fact, the thin beam model is only useful in determining the effect of beam thickness in growth rates for off resonance, cutoff points. The $k_z = 0$ restriction is due to the synchronous approximation given in Eq. (16). For this special case, $\hat{\psi}_\ell$ typically varies less than 1% over the

allowed range of x_0 . There are at least two ways to get more information about the effect of beam thickness on growth rates. The first possibility is to solve the equations to higher order in x_0 . The procedure for doing this is straightward, but the amount of algebraic work increases tremendously. For example, in order to expand the fields to second order in x_0 , they would have to be expanded to fifth order in z . The second order equilibrium density function would also be more complicated, at least until $\rho = 1$ could be justified. The second approach is a numerical one and is the subject of Section IV.

D. Solution of the Coaxial Case

The only computational difference between the cases of cylindrical waveguides with and without inner conductors is in the calculation of α_e^- and α_b^- . The axial fields between the inner conductor and the beam can be written

$$\hat{E}_z = \frac{P_\ell(y, y_1)}{P_\ell(y_-, y_1)} \hat{E}_z^- \quad (30a)$$

and

$$c\hat{B}_z = \frac{r_- Q_\ell(y, y_1)}{y_- S_\ell(y_-, y_1)} (\partial_r c\hat{B}_z)^- \quad (30b)$$

where $r_1 < r < r_-$, and so

$$\alpha_e^- = [y_{-R_\ell}(y_-, y_i)] / P_\ell(y_-, y_i) \quad (31a)$$

and

$$\alpha_b^- = Q_\ell(y_-, y_i) / [y_{-S_\ell}(y_-, y_i)] \quad (31b)$$

The new average and difference geometry parameters can be calculated for the inner conductor case and the remainder of the algorithm does not change. The linear expansions are

$$\begin{aligned} \alpha_e^o &= \frac{1}{2} \left(\frac{y_o \hat{R}_1}{\hat{P}_1} + \frac{y_o \hat{R}_2}{\hat{P}_2} \right) + x_o \left(\frac{\hat{P}_3}{\pi \hat{P}_1 \hat{P}_2} \right) \left(\frac{y_o \hat{R}_1}{\hat{P}_1} + \frac{y_o \hat{R}_2}{\hat{P}_2} \right) \\ \alpha_e^\Delta &= - \left(\frac{\hat{P}_3}{\pi \hat{P}_1 \hat{P}_2} \right) + x_o \left\{ \ell^2 - y_o^2 - \frac{1}{2} \left[\left(\frac{y_o \hat{R}_1}{\hat{P}_1} \right)^2 + \left(\frac{y_o \hat{R}_2}{\hat{P}_2} \right)^2 \right] \right\} \\ \alpha_b^o &= \frac{1}{2} \left(\frac{\hat{Q}_1}{y_o \hat{S}_1} + \frac{\hat{Q}_2}{y_o \hat{S}_2} \right) + x_o \left(\frac{-\hat{S}_3}{\pi y_o^2 \hat{S}_1 \hat{S}_2} \right) (\ell^2 - y_o^2) \left(\frac{\hat{Q}_1}{y_o \hat{S}_1} + \frac{\hat{Q}_2}{y_o \hat{S}_2} \right) \\ \alpha_b^\Delta &= \left(\frac{\hat{S}_3}{\pi y_o^2 \hat{S}_1 \hat{S}_2} \right) + x_o \left\{ 1 - \frac{1}{2} (\ell^2 - y_o^2) \left[\left(\frac{\hat{Q}_1}{y_o \hat{S}_1} \right)^2 + \left(\frac{\hat{Q}_2}{y_o \hat{S}_2} \right)^2 \right] \right\} \end{aligned} \quad (32)$$

for $\hat{P}_1 = P_\ell(y_+, y_w)$, $\hat{P}_2 = P_\ell(y_-, y_i)$, and $\hat{P}_3 = P_\ell(y_w, y_i)$, etc.

Figure 7 demonstrates the effect of axial wavelength on $\hat{\Psi}_\ell$ for a coaxial system with $\ell = 7$, $n_r = 1$, $r_o = 0.075$ m, $r_i = 0.0626$ m, $r_w = 0.10$ m, $\hat{\beta}_{\theta_o} = 0.9$, $\hat{\beta}_{z_o} = 0.4$, and $n_s = 10^{11} \text{ m}^{-2}$. Figure 7(a) shows the effect

of k_z on ω_r . Between resonance points, ω_r is close to zero as predicted.⁵ At resonance, $\omega_r \approx \Gamma/\sqrt{3}$. Outside the unstable region, ω_r increases rapidly, indicating that the solution is tracking the empty waveguide mode. Figure 7(b) shows the effect of k_z on Γ . The coaxial results are quite similar to the simple empty waveguide results.

IV. THE NUMERIC SOLUTION

The analytic model has the a priori restriction that $\Delta r \ll r_0$. Thus, the analytic model is valid from $\Delta r = 0$ to some small value which is at most a few percent of the average beam radius. In contrast, the numeric model is not defined for $\Delta r = 0$. The thickness can be made arbitrarily small, but the computational cost increases tremendously with decreasing thickness. Furthermore, there is no a priori limit on the maximum beam thickness, though each particular problem is limited by the cusp field cutoff. Thus, the domain of the analytic model extends from the zero thickness limit out to some small maximum value and the numeric model's validity ranges from some practical minimum out to the cusp cutoff layer. In principle, the ranges of the two models overlap and a complete growth rate versus thickness picture can be drawn. Unfortunately, in most cases the thin beam limit is too small for the thick beam model to be applied there.

The numeric approach involves solving the inhomogeneous wave equation for \tilde{E}_z and $c\tilde{B}_z$. In both simple and coaxial waveguides (among others), \tilde{E}_z can be written as a linear combination of the homogeneous transverse magnetic (TM) solutions and $c\tilde{B}_z$ can be written as a linear combination of the homogeneous transverse electric (TE) solutions. With the aid of these homogeneous solutions, the inhomogeneous wave equation problem is reduced to an exercise in finding the zeros of the determinant of an infinite matrix. The numerical method solves various finite approximations of this

matrix and compares the answers to determine whether or not the truncated solutions appear to be converging. The apparent limit is assumed to be the correct answer. The formal solution of the inhomogeneous problem is derived in Section A. Typical results are discussed in Section B. In Section C, the solution for the coaxial case is presented and results are given.

A. The Formal Solution

The perturbed velocity is still given by Eq. (10) but the perturbed density [Eq. (12)] has to be found in terms of the EM fields with the help of Maxwell's Equations:

$$\begin{aligned}
 N^* = \frac{i e \tilde{n}_1}{\epsilon_o} = & \left(\frac{c D_\ell^2}{\psi_\ell E_\ell^2} \frac{d n_o}{d r} - 2 n_o \frac{c \Omega_o}{E_\ell^2} k_z \frac{\beta_{\theta_o}}{\beta_{z_o}} \right) \frac{e \tilde{v}_{r1}}{\epsilon_o c} \\
 & + \frac{\omega_p^2}{E_\ell^2} \left(- \frac{\Omega_o}{\psi_\ell} \frac{\beta_{\theta_o}}{\beta_{z_o}} x_4 + \frac{\beta_{\theta_o}}{\beta_{z_o}} x_5 + x_6 \right) \\
 & + \frac{\omega_p^2}{E_\ell^2} \left\{ \left(\frac{\Omega_o}{\psi_\ell} \right)^2 \left[\frac{\ell}{r} \beta_{\theta_o} \beta_{z_o} - k_z (1 - \beta_{z_o}^2) \right] \right. \\
 & \left. + \beta_{z_o} \left(\frac{\psi_\ell}{c} - \frac{\omega_p^2 / \gamma_o^2}{c \psi_\ell} \right) \right\} \left(\frac{\beta_{\theta_o}}{\beta_{z_o}} x_2 + x_3 \right) \quad (33)
 \end{aligned}$$

where $\omega_p^2(r) = e^2 n_o(r) / (\epsilon_o m_o \gamma_o)$, $E_\ell^2 = D_\ell^2 - \omega_p^2 / \gamma_o^2$, and

$$\begin{aligned} \chi_1 &= -i\hat{E}_r & \chi_2 &= \hat{E}_\theta & \chi_3 &= \hat{E}_z \\ & & & & & (34) \end{aligned}$$

$$\begin{aligned} \chi_4 &= c\hat{B}_r & \chi_5 &= -ic\hat{B}_\theta & \chi_6 &= -ic\hat{B}_z . \end{aligned}$$

The perturbed currents can then be found as before:

$$J_r^* = \frac{\hat{J}_{r1}}{\epsilon_0 c} = - \left(\frac{en_0}{\epsilon_0 c} \right) \hat{v}_{r1} \quad (35a)$$

$$J_\theta^* = \frac{i\hat{J}_{\theta1}}{\epsilon_0 c} = -\beta_{\theta 0} N^* - \left(\frac{ien_0}{\epsilon_0 c} \right) \hat{v}_{\theta 1} \quad (35b)$$

$$J_z^* = \frac{i\hat{J}_{z1}}{\epsilon_0 c} = -\beta_{z 0} N^* - \left(\frac{ien_0}{\epsilon_0 c} \right) \hat{v}_{z 1} . \quad (35c)$$

For fixed ℓ and $1 < m < \infty$, we define the functions

$$u_{\ell m 1}(r) = \frac{\sqrt{2}}{r_w J'_\ell(\beta_{\ell m})} J_\ell(\beta_{\ell m} r/r_w) \quad (36a)$$

and

$$u_{\ell m 3}(r) = \frac{\sqrt{2} \alpha_{\ell m}}{r_w \sqrt{\alpha_{\ell m}^2 - \ell^2} J'_\ell(\alpha_{\ell m})} J_\ell(\alpha_{\ell m} r/r_w) \quad (36b)$$

where $\beta_{\ell m}$ is the m^{th} zero of J_ℓ and $\alpha_{\ell m}$ is the m^{th} zero of J'_ℓ . These functions satisfy the orthonormal conditions:

$$\int_0^{r_w} u_{\ell m 1}(r) u_{\ell n 1}(r) r dr = \delta_{mn} \quad (37a)$$

and

$$\int_0^{r_w} u_{\ell m 3}(r) u_{\ell n 3}(r) r dr = \delta_{mn} \quad (37b)$$

$\forall 1 < m, n < \infty$, where δ_{mn} is the Kronecker delta function. Furthermore, it can be shown that for

$$E_m = \int_0^{r_w} \chi_3(r) u_{\ell m 1}(r) r dr \quad (38a)$$

and

$$B_m = \int_0^{r_w} \chi_6(r) u_{\ell m 3}(r) r dr, \quad (38b)$$

the expressions

$$\chi_3 = \sum_{m=1}^{\infty} E_m u_{\ell m 1}(r) \quad (39a)$$

and

$$\chi_6 = \sum_{m=1}^{\infty} B_m u_{\ell m 3}(r) \quad (39b)$$

are valid, i.e. the sums converge at every point in the interval $[0, r_w]$. This fact is true because $\{u_{\ell m 1}\}_{m=1}^{\infty}$ and $\{u_{\ell m 3}\}_{m=1}^{\infty}$ are complete in the appropriate spaces and because χ_3 and χ_6 are assumed to have the required degree of "smoothness."

We define the unknown vector $\vec{k} = (\kappa_1 \ \kappa_2 \ \kappa_3 \ \kappa_4)^T$ by

$$\kappa_1(r) = \widehat{E}_z(r) = \sum_{m=1}^{\infty} E_m u_{\ell m 1}(r) \quad (40a)$$

$$\kappa_2(r) = r \partial_r \widehat{E}_z(r) = \sum_{m=1}^{\infty} E_m u_{\ell m 2}(r) \quad (40b)$$

$$\kappa_3(r) = -ic \widehat{B}_z(r) = \sum_{m=1}^{\infty} B_m u_{\ell m 3}(r) \quad (40c)$$

$$\kappa_4(r) = -ir \partial_r c \widehat{B}_z(r) = \sum_{m=1}^{\infty} B_m u_{\ell m 4}(r) \quad (40d)$$

($u_{\ell m 2} = r \partial_r u_{\ell m 1}$ and $u_{\ell m 4} = r \partial_r u_{\ell m 3}$). With these complete orthonormal systems (CONS), the numeric problem can be reformulated as a problem of finding allowable values of ω 's and the corresponding sequences $\{E_m, B_m\}_1^{\infty}$. To do this, the perturbed sources must be written in terms of \vec{k} . The sources are already known in terms of $\chi_1 - \chi_6$ from Eqs. (33) through (35) and can be written symbolically as

$$\begin{aligned} J_r^* &\triangleq \sum_{i=1}^6 j_r^i \chi_i & J_z^* &\triangleq \sum_{i=1}^6 j_z^i \chi_i \\ J_\theta^* &\triangleq \sum_{i=1}^6 j_\theta^i \chi_i & N^* &\triangleq \sum_{i=1}^6 n^i \chi_i \end{aligned} \quad (41)$$

From Maxwell's equations it can be shown that

$$\xi^2 \chi_1 = -\frac{\omega}{c} J_r^* + \frac{1}{r} (k_z \kappa_2 - \frac{\omega}{c} \ell \kappa_3) \quad (42a)$$

$$\xi^2 \chi_2 = -\frac{\omega}{c} J_\theta^* + \frac{1}{r} (-k_z \ell \kappa_1 + \frac{\omega}{c} \kappa_4) \quad (42b)$$

$$\xi^2 \chi_4 = k_z J_\theta^* + \frac{1}{r} (\frac{\omega}{c} \ell \kappa_1 - k_z \kappa_4) \quad (42c)$$

$$\xi^2 \chi_5 = -k_z J_r^* + \frac{1}{r} (\frac{\omega}{c} \kappa_2 - k_z \ell \kappa_3) \quad (42d)$$

With the help of Eq. (41), $\chi_1 - \chi_6$ can be eliminated from Eq. (42):

$$(J_r^* \quad J_\theta^*)^T = Q^{-1}(r) R(r) \vec{k}(r) \quad (43a)$$

for

$$Q = \begin{bmatrix} \xi^2 + j_r^1 \frac{\omega}{c} + j_r^5 k_z & j_r^2 \frac{\omega}{c} - j_r^4 k_z \\ j_\theta^1 \frac{\omega}{c} + j_\theta^5 k_z & \xi^2 + j_\theta^2 \frac{\omega}{c} - j_\theta^4 k_z \end{bmatrix} \quad (43b)$$

and

$$rR = \begin{bmatrix} rj_r^3 \xi^2 + \ell(-j_r^2 k_z + j_r^4 \frac{\omega}{c}) & rj_\theta^3 \xi^2 + \ell(-j_\theta^2 k_z + j_\theta^4 \frac{\omega}{c}) \\ j_r^1 k_z + j_r^5 \frac{\omega}{c} & j_\theta^1 k_z + j_\theta^5 \frac{\omega}{c} \\ rj_r^6 \xi^2 - \ell(j_r^1 \frac{\omega}{c} + j_r^5 k_z) & rj_\theta^6 \xi^2 - \ell(j_\theta^1 \frac{\omega}{c} + j_\theta^5 k_z) \\ j_r^2 \frac{\omega}{c} - j_r^4 k_z & j_\theta^2 \frac{\omega}{c} - j_\theta^4 k_z \end{bmatrix}^T \quad (43c)$$

Plugging Eq. (43) into Eq. (42) gives $\chi_1 - \chi_6$ in terms of \vec{k} (notice that $\chi_3 = \kappa_1$ and $\chi_6 = \kappa_3$). Afterward, J_z^* and N^* can be found from Eq. (41). The net result is that the perturbed sources are known in terms of \vec{k} and can be symbolically written

$$\begin{aligned} J_r^* &= \sum_{i=1}^4 J_r^i \kappa_i & J_z^* &= \sum_{i=1}^4 J_z^i \kappa_i \\ J_\theta^* &= \sum_{i=1}^4 J_\theta^i \kappa_i & N^* &= \sum_{i=1}^4 N^i \kappa_i \end{aligned} \quad (44)$$

The inhomogeneous wave equations for \hat{E}_z and $c\hat{B}_z$ are

$$\left(\frac{\partial^2}{\partial r^2} + \frac{1}{r} \frac{\partial}{\partial r} - \frac{\ell^2}{r^2} + \xi^2 \right) \kappa_1 = -\frac{\omega}{c} J_z^* - k_z N^* \quad (45a)$$

and

$$\left(\frac{\partial^2}{\partial r^2} + \frac{1}{r} \frac{\partial}{\partial r} - \frac{\ell^2}{r^2} + \xi^2 \right) \kappa_3 = \frac{1}{r} \partial_r (r J_\theta^*) + \frac{\ell}{r} J_r^* \quad (45b)$$

Multiplying Eq. (45a) by $ru_{\ell n1}(r)$, Eq. (45b) by $ru_{\ell n3}(r)$, and integrating both from 0 to r_w yields:

$$E_n(\xi^2 - \beta_{\ell n}^2/r_w^2) = \sum_{m=1}^{\infty} E_m S_{2n-1,2m-1} + \sum_{m=1}^{\infty} B_m S_{2n-1,2m} \quad (46a)$$

for

$$S_{2n-1,2m-1} = - \int_{r_o-\Delta r}^{r_o+\Delta r} ru_{\ell n1}(r) \{ [\frac{\omega}{c} J_z^1(r) + k_z N^1(r)] u_{\ell m1}(r) + [\frac{\omega}{c} J_z^2(r) + k_z N^2(r)] u_{\ell m2}(r) \} dr \quad (46b)$$

and

$$S_{2n-1,2m} = - \int_{r_o-\Delta r}^{r_o+\Delta r} ru_{\ell n1}(r) \{ [\frac{\omega}{c} J_z^3(r) + k_z N^3(r)] u_{\ell m3}(r) + [\frac{\omega}{c} J_z^4(r) + k_z N^4(r)] u_{\ell m4}(r) \} dr, \quad (46c)$$

and

$$B_n(\xi^2 - \alpha_{\ell n}^2/r_w^2) = \sum_{m=1}^{\infty} E_m S_{2n,2m-1} + \sum_{m=1}^{\infty} B_m S_{2n,2m} \quad (46d)$$

for

$$S_{2n,2m-1} = \int_{r_o-\Delta r}^{r_o+\Delta r} \{ u_{\ell n3}(r) \ell [J_r^1(r) u_{\ell m1}(r) + J_r^2(r) u_{\ell m2}(r)] - u_{\ell n4}(r) [J_\theta^1(r) u_{\ell m1}(r) + J_\theta^2(r) u_{\ell m2}(r)] \} dr \quad (46e)$$

and

$$S_{2n,2m} = \int_{r_o - \Delta r}^{r_o + \Delta r} \{ u_{\ell n 3}(r) [J_r^3(r) u_{\ell m 3}(r) + J_r^4(r) u_{\ell m 4}(r)] - u_{\ell n 4}(r) [J_\theta^3(r) u_{\ell m 3}(r) + J_\theta^4(r) u_{\ell m 4}(r)] \} dr . \quad (46f)$$

By defining

$$D = \text{diag} [\xi^2 - (\beta_{\ell 1} / r_w)^2, \xi^2 - (\alpha_{\ell 1} / r_w)^2, \dots, \xi^2 - (\beta_{\ell m} / r_w)^2, \xi^2 - (\alpha_{\ell m} / r_w)^2, \dots] , \quad (47)$$

it follows from Eqs. (46) and (47) that the eigenvalues are given by:

$$\det(D - S)(\omega) = 0 . \quad (48)$$

If $\hat{\omega}$ is a solution of Eq. (48), the fields are given by the vector

$$\hat{\mathbf{A}} = (E_1, B_1, \dots, E_m, B_m, \dots)^T \quad (49)$$

that satisfies $S(\hat{\omega})\hat{\mathbf{A}} = D(\hat{\omega})\hat{\mathbf{A}}$.

The solution of the linear growth rate problem can in theory be found by locating the solutions of Eq. (48). Everything that is needed to find the matrix S has been derived in this section. When $\hat{n}_0 = 0$, S is identically zero and the solutions correspond to the empty waveguide modes,

as they must. When $\hat{n}_0 \neq 0$, the solution can only be found approximately by numerical techniques.

Solutions are found as follows. The D and S matrices are truncated after a finite number of rows and columns. The integrals in the S matrix are approximated by Simpson's extended rule. The determinant of the matrix is found by Gaussian elimination with full pivoting. The zeros of the determinant are found by recursive linear extrapolation starting with the single particle results. Although the thick beam model is formally valid without any restrictions (except for self-field considerations), it is computationally practical only to look for solutions near the tenuous, resonant limit.

B. Properties of the Solution

Numerical solutions of Γ as a function of beam thickness are shown in Fig. 8 for a system with $\ell = 7$, $n_r = 1$ (TE), $r_0 = 0.06$ m, $r_w = 0.0865$ m, $\hat{\beta}_\theta = 0.85$, $\hat{\beta}_{z_0} = 0.5$, $n_s = 10^8$ m⁻², $k_z = 0$, and $\hat{z} = 2.0$, the equilibrium defined in Eq. (6). For these parameters, the cusp cutoff limits the beam thickness to $x_0 < 0.16$. The solutions are plotted for several different finite approximations of the D and S matrices in order to demonstrate convergence problems. As the beam thickness decreases, the growth rate solution for a fixed number of eigenvectors starts to decrease. The solution eventually begins to increase and ultimately heads toward infinity as the beam thickness approaches zero. The tendency of the growth rates to eventually increase as the beam thickness decreases is a result of the truncation of the D and S matrices and is not a property of the exact solution. As the number of eigenvectors used increases so does the region

of convergence. When 50 eigenvectors are used, the result appears to have converged all the way down to $x_0 \sim 0.06$. When $x_0 > 0.13$, 20 eigenvectors are sufficient to get an accurate answer. More eigenvectors are needed for convergence as the beam thickness decreases because the density distribution becomes more and more like a delta function distribution. Thus, it is the truncation of the infinite matrices that puts a practical limit on the allowed values of x_0 in the thick beam model. In the remainder of the figures in this section, the curves are plotted for a fixed number of eigenvectors (< 50), and regions where the solutions have not converged are indicated by dashed lines.

In Fig. 9, Γ is plotted as a function of the effective beam thickness for three different beam profiles. The beam parameters are still those of Fig. 8; the other two curves correspond to $\hat{z} = 1$ and $\rho = 0.95$. The effective thickness for the three models as defined by Eqs. (3) and (8) are: $0.383 x_0$ for $\hat{z} = 2.0$, $0.603 x_0$ for $\hat{z} = 1.0$, and $0.975 x_0$ for $\rho = 0.95$. The growth rate is in reasonably good agreement for the various models. Unfortunately, convergence problems make it impossible to determine if the solutions converge to the same point as $x_0 \rightarrow 0$ (as predicted by the thin beam model). Because an effective thickness is used, the differences between the curves are attributed mainly to the shapes of the density profiles. The curves predict less than a 1% shift in Γ over the whole range of beam thicknesses.

The three models (single particle, analytic, and numeric) are compared in Fig. 10 for the parameters of Fig. 8. (except that the $\rho = 0.95$ curve is shown). The effective thickness is used for the numeric model. The allowed range of x_0 for the analytic model is not well defined because the

solution is at a resonant point. Nonetheless, there is excellent agreement of the two models for Γ .

The agreement of the two fluid models should not be taken for granted. Although the models start with the same basic equations, the approaches taken are quite different. For example, the thin beam model is essentially an expansion about the zero thickness dispersion relation [Eq. (29)] while the numeric model is an expansion about an empty waveguide solution (the matrix D). The two methods should only be expected to agree perfectly when the analytic models' Taylor series expansion is carried out to all orders and the numeric models' D and S matrices are solved exactly.

In Fig. 11, the growth rate is plotted as a function of beam thickness for two systems with different wall radii. The common parameters are $\ell = 7$, $n_r = 1$, $r_o = 0.06$ m, $\hat{\beta}_{\theta_o} = 0.85$, $\hat{\beta}_{z_o} = 0.5$, $n_s = 10^8$ m⁻², and $\hat{z} = 2.0$. The axial wave numbers are adjusted so that both solutions correspond to resonance points. The first curve has $k_z = 0$ and $r_w = 0.0865$ m, and the second curve has $k_z = 1.165$ m⁻¹ and $r_w = 0.0860$ m. For the first time a solution has been plotted for a system having k_z , \hat{v}_{z_o} , and x_o all nonzero simultaneously. Consequently, this is the first result for a system whose E layer is only approximately in synchronism with the EM wave (for the first time ψ_ℓ is a function of r). The finite k_z growth rate is a rapidly decreasing function of beam thickness. For example, the finite k_z growth rate is roughly one half of the zero thickness growth rate (indicated by the square) at a relative thickness of 7.5%.

Because the two cases in Fig. 11 are very similar physically (the wall radius changes by less than 0.6%), the difference in the curves is attributed mainly to the loss of complete synchronism. This quasi-

synchronous effect can be scaled to higher densities as follows. An estimate of the relative deviation from synchronism at the outer beam edge is [from Eq. (15)]

$$\frac{\Delta\psi_\ell}{\hat{\psi}_\ell} = \Delta v_{z_0} k_z / \hat{\psi}_\ell, \quad (50a)$$

so in the tenuous limit⁵

$$\frac{\Delta\psi_\ell}{\hat{\psi}_\ell} \propto (k_z/n_s^{1/3}). \quad (50b)$$

Thus, for every three orders of magnitude increase in beam density, the growth rate curve will be similar for a one order magnitude decrease in axial wavelength. The axial wavelength for the finite k_z case is ~ 5.4 m. For a beam density of $n_s = 10^6 \text{ m}^{-2}$, the same relative decrease in Γ should be found for $\lambda_z \sim 25$ m. Likewise, for $n_s = 10^{10} \text{ m}^{-2}$, the appropriate λ_z is ~ 1.16 m. Normalized growth rates at isolated points are indicated in Fig. 11 for $n_s = 10^6 \text{ m}^{-2}$ (diamonds) and $n_s = 10^{10} \text{ m}^{-2}$ (circles). The axial wave numbers are scaled accordingly. The results support this simple scaling law. It should be noted that the $x_0 = 0.04$ point for $n_s = 10^{10} \text{ m}^{-2}$ had not completely converged after 50 eigenvectors and the actual result is (probably) closer to the curve than indicated.

C. Solution of the Coaxial Case

The only difference between the solutions of the coaxial case and the simple empty waveguide case is in the CONS used. The two CONS for the coaxial case are given by

$$u_{\ell m 1}(r) = \frac{\sqrt{2} P_{\ell}(\beta_{\ell m} y, \beta_{\ell m}) / r_w}{[(2/\pi \beta_{\ell m})^2 - y_i^2 R_{\ell}^2(\beta_{\ell m} y_i, \beta_{\ell m})]^{1/2}} \quad (51a)$$

and

$$u_{\ell m 3}(r) = \frac{\sqrt{2} Q_{\ell}(\alpha_{\ell m} y, \alpha_{\ell m}) / r_w}{\left\{ \left(\frac{2}{\pi \alpha_{\ell m}} \right)^2 [1 - (\ell/\alpha_{\ell m})^2] - [y_i^2 - (\ell/\alpha_{\ell m})^2] Q_{\ell}^2(\alpha_{\ell m} y_i, \alpha_{\ell m}) \right\}^{1/2}} \quad (51b)$$

for fixed ℓ and $1 < m < \infty$, and for $y = r/r_w$ and $y_i = r_i/r_w$. Now $\alpha_{\ell m}(\beta_{\ell m})$ is the m^{th} zero of $S_{\ell}(\alpha_{\ell m} y_i, \alpha_{\ell m}) [P_{\ell}(\beta_{\ell m} y_i, \beta_{\ell m})]$. Equations (37) and (38) are valid for the functions defined in Eq. (51) provided that the lower integration limit is set to r_i [κ_2 and κ_4 are still given by Eq. (40)].

Growth rates for coaxial cases with finite axial wave numbers are shown in Fig. 12. The parameters are $\ell = 7$, $n_r = 1$, $r_i = 0.0626$ m, $r_o = 0.07509$ m, $r_w = 0.1$ m, $\hat{\beta}_{\theta_o} = 0.9$, $\hat{\beta}_{z_o} = 0.4$, $k_z = 0.3 \text{ m}^{-1}$, and $n_s = 10^8 \text{ m}^{-2}$. The curves are drawn for $\hat{z} = 1.0$ and $\hat{z} = 2.0$. The curves are plotted as a function of the relative beam thickness and the $k_z = 0$ ($r_o = 0.07500$ m) growth rate is shown as a reference. The two finite k_z growth rates are in good agreement with each other. As usual, the curves drop off rapidly as the beam thickness increases.

V. CONCLUSIONS

In summary, we have carried out a linear fluid analysis that is applicable to cusp-injected beams with finite radial thickness. Two approaches were taken. In the analytic approach, we expanded the fluid equations in the ratio $\Delta r/r_0$ and recovered the single particle, tenuous beam result. Furthermore, we noted that the analytic result was valid off resonance and at somewhat larger beam densities (than the single particle result). The latter extension was useful in helping to quantify the limits of the tenuous regime. Unfortunately, we discovered that the analytic result has only limited usefulness in the analysis of thick beam configurations.

In the numeric approach, we solved the inhomogeneous wave equations via expansions in the homogeneous solutions. Because of computational limitations, results were only displayed for resonant systems with tenuous beams. We demonstrated that resonant systems with thick, tenuous beams cannot be operated far from cutoff without a substantial reduction in the linear growth rate. We attributed the reduced growth rates to the loss of synchronism inherent in systems that have a spread in canonical angular momentum (manifested by a finite Δv_z in our model).

In our analyses we focused on two particular conducting wall geometries: circular and coaxial waveguide systems. Extending the analyses to other waveguide geometries is straightforward. In the analytic model, only the geometry parameters (normalized wave admittances) need to be adjusted. For the numeric model, results can be obtained if the

complete, orthonormal systems consisting of the relevant homogeneous solutions are known. Other physical systems can be modeled by choosing the appropriate equilibrium and following the general procedures outlined in this paper.

Acknowledgments

This work is supported by the Air Force Office of Scientific Research with computational time provided by the University of Maryland Computer Center and the Electrical Engineering Computer Facilities.

References

1. R. J. Briggs and V. K. Neil, *J. Nucl. Energy* C9, 209 (1967).
2. P. Sprangle, *J. Appl. Phys.* 47, 2935 (1976).
3. W. W. Destler, H. Romero, C. D. Striffler, R. L. Weiler, and W. Namkung, *J. Appl. Phys.* 52, 2740 (1981).
4. C. D. Striffler, W. W. Destler, R. Kulkarni, and R. L. Weiler, *IEEE Trans. Nucl. Sci.* NS-30, 3429 (1983).
5. W. Lawson and C. D. Striffler, *Phys. Fluids* 28, 2868 (1985).
6. W. Lawson, W. W. Destler, and C. D. Striffler, to be published in *IEEE Trans. Plasma Sci.*
7. Y. Y. Lau, *IEEE Trans. Electron Devices* ED-29, 320 (1982).
8. D. Chernin and Y. Y. Lau, *Phys. Fluids* 27, 2319 (1984).
9. H. S. Uhm and R. C. Davidson, *J. Appl. Phys.* 49, 593 (1978).
10. H. S. Uhm and R. C. Davidson, *Phys. Fluids* 21, 265 (1978).
11. H. S. Uhm, C. M. Kim, and W. Namkung, *Phys. Fluids* 27, 488 (1984).
12. W. Namkung, *Phys. Fluids* 27, 329 (1984).
13. M. J. Rhee and W. W. Destler, *Phys. Fluids* 17, 1574 (1974).
14. D. B. McDermott, N. C. Luhmann, Jr., D. S. Furuno, A. Kupiszewski, and H. R. Jory, *Int. J. Infrared and Millimeter Waves* 4, 639 (1983).
15. L. R. Barnett, J. M. Baird, P. S. Rha, V. A. Shrivastava, and R. W. Grow, 1985 *IEEE Int. Conf. Plasma Science Conference Record*, p. 6.
16. I. S. Gradshteyn and I. M. Ryzhik, Table of Integrals, Series, and Products (Academic Press, New York, 1965), p. 1058.
17. M. Abramowitz and I. A. Stegun, Handbook of Mathematical Functions (Dover Publications, Inc., New York, 1965), p. 361.

APPENDIX A

Integrals of the Perturbed Fluid Velocity

Equations (10) and (21) are used many times to obtain the following results:

$$\begin{aligned}
& \left(\frac{en}{\epsilon_0} \right) \int_{r_0 - \Delta r}^{r_0 + \Delta r} \frac{(1 + Fx)}{\psi_\ell^n} \tilde{v}_{r1} dr \\
&= \frac{\omega_r}{D_\ell^2 \psi_\ell^n} \left\{ \hat{\psi}_\ell [-i\tilde{E}_r^0 + \hat{\beta}_\theta (-ic\tilde{B}_z^0) - \hat{\beta}_{z_0} (-ic\tilde{B}_\theta^0)] + \Omega_0 (\tilde{E}_\theta^0 + \hat{\beta}_{z_0} c\tilde{B}_r^0) \right. \\
&\quad - \frac{x_0}{3} \left\{ \hat{\psi}_\ell [-ir_0 (\tilde{E}_r')^\Delta + \hat{\beta}_\theta (-ir_0 (c\tilde{B}_z')^\Delta) - \hat{\beta}_{z_0} (-ir_0 (c\tilde{B}_\theta')^\Delta)] \right. \\
&\quad \left. \left. + \Omega_0 (r_0 (\tilde{E}_\theta')^\Delta + \hat{\beta}_{z_0} r_0 (c\tilde{B}_r')^\Delta) \right\} \right. \\
&\quad + \frac{2x_0}{5} \left\{ [(F - 2T\hat{G}_\ell^2)\hat{\psi}_\ell + T(1 - n)\Omega_0](-i\tilde{E}_r^\Delta) \right. \\
&\quad + [(F - 2T\hat{G}_\ell^2 + 1)\hat{\psi}_\ell + T(1 - n)\Omega_0]\hat{\beta}_\theta (-ic\tilde{B}_z^\Delta) \\
&\quad - [(F - 2T\hat{G}_\ell^2 - \tau)\hat{\psi}_\ell + T(1 - n)\Omega_0]\hat{\beta}_{z_0} (-ic\tilde{B}_\theta^\Delta) \\
&\quad \left. + (F - 2T\hat{G}_\ell^2 - nT\Omega_0/\hat{\psi}_\ell)\Omega_0(\tilde{E}_\theta^\Delta) \right. \\
&\quad \left. + (F - 2T\hat{G}_\ell^2 - nT\Omega_0/\hat{\psi}_\ell - \tau)\Omega_0\hat{\beta}_{z_0}(c\tilde{B}_r^\Delta) \right\}, \quad (A.1a)
\end{aligned}$$

$$\begin{aligned}
& \left(\frac{i e n_0}{\epsilon_0} \right) \int_{r_0 - \Delta r}^{r_0 + \Delta r} \frac{(1 + Fx)}{\psi_\ell^n} \hat{v}_{\theta 1} \, dr \\
&= \frac{\omega^2 b r_0}{\psi_\ell^{n+1}} \left\{ (1 - \hat{\beta}_{\theta 0}^2) \hat{E}_\theta^0 + \hat{\beta}_{z_0} c \hat{B}_r^0 - \hat{\beta}_{\theta 0} \hat{\beta}_{z_0} \hat{E}_z^0 \right. \\
&\quad - \frac{x_0}{3} [(1 - \hat{\beta}_{\theta 0}^2) r_0 (\hat{E}'_\theta)^\Delta + \hat{\beta}_{z_0} r_0 (c \hat{B}'_r)^\Delta - \hat{\beta}_{\theta 0} \hat{\beta}_{z_0} r_0 (\hat{E}'_z)^\Delta] \\
&\quad + \frac{2x_0}{5} \{ [F - (n+1)T\Omega_0 / \hat{\psi}_\ell] (1 - \hat{\beta}_{\theta 0}^2) - 2\hat{\beta}_{\theta 0}^2 \} \hat{E}_\theta^\Delta \\
&\quad + [F - (n+1)T\Omega_0 / \hat{\psi}_\ell - \tau] \hat{\beta}_{z_0} c \hat{B}_r^\Delta \\
&\quad \left. - [F - (n+1)T\Omega_0 / \hat{\psi}_\ell + 1 - \tau] \hat{\beta}_{\theta 0} \hat{\beta}_{z_0} \hat{E}_z^\Delta \right\} \\
&\quad + \Omega_0 \left(\frac{e n_0}{\epsilon_0} \right) \int_{r_0 - \Delta r}^{r_0 + \Delta r} \frac{(1 + F)}{\psi_\ell^{n+1}} \hat{v}_{r 1} \, dr, \tag{A.1b}
\end{aligned}$$

and

$$\begin{aligned}
& \left(\frac{i e n_o}{\epsilon_o} \right) \int_{r_o - \Delta r}^{r_o + \Delta r} \frac{(1 + Fx)}{\psi_\ell^n} \tilde{v}_{z_1} dr \\
& = \frac{\omega_b^2 r_o}{\hat{\psi}_{n+1}} (1 - \hat{\beta}_{z_o}^2) \tilde{E}_z^o - \hat{\beta}_{\theta_o} c \tilde{B}_r^o - \hat{\beta}_{\theta_o} \hat{\beta}_{z_o} \tilde{E}_\theta^o \\
& \quad - \frac{x}{3} [(1 - \hat{\beta}_{z_o}^2) r_o (\tilde{E}_z')^\Delta - \hat{\beta}_{\theta_o} r_o (c \tilde{B}_r')^\Delta - \hat{\beta}_{\theta_o} \hat{\beta}_{z_o} r_o (\tilde{E}_\theta')^\Delta] \\
& \quad + \frac{2x}{5} \{ [F - (n+1) T \Omega_o / \hat{\psi}_\ell] (1 - \hat{\beta}_{z_o}^2) + 2 \hat{\beta}_{\theta_o}^2 \} \tilde{E}_z^\Delta \\
& \quad - [F - (n+1) T \Omega_o / \hat{\psi}_\ell + 1] \hat{\beta}_{\theta_o} c \tilde{B}_r^\Delta \\
& \quad - [F - (n+1) T \Omega_o / \hat{\psi}_\ell + 1 - \tau] \hat{\beta}_{\theta_o} \hat{\beta}_{z_o} \tilde{E}_\theta^\Delta \\
& \quad - \Omega_o \frac{\hat{\beta}_{\theta_o}}{\hat{\beta}_{z_o}} \left(\frac{e n_o}{\epsilon_o} \right) \int_{r_o - \Delta r}^{r_o + \Delta r} \frac{[1 + (F + 1 + \tau)x]}{\psi_\ell^{n+1}} \tilde{v}_{r_1} dr,
\end{aligned}$$

(A.1c)

for $\omega_b^2 = n_s e^2 / (m_o \gamma_o \epsilon_o r_o)$, $\hat{D}_\ell^2 = \hat{\psi}_\ell^2 - \Omega_o^2$, and $\hat{G}_\ell^2 = \Omega_o \hat{\psi}_\ell / \hat{D}_\ell^2$.

Figure Captions

- FIG. 1. The fluid equilibrium.
- FIG. 2. The piecewise cubic equilibrium density profile: (a) $n_o(z)$ and (b) $n'_o(z)$ for $\rho = 0$ (\diamond), 0.5 (∇), and 0.95 (Δ). For each curve, $n_s = 2\Delta r$.
- FIG. 3. The smooth equilibrium density profile: (a) $n_o(z)$ and (b) $n'_o(z)$ for $\hat{z} = 0.125$ (Δ), 1.0 (∇), and 2.0 (\diamond). For each curve, $n_s = 2\Delta r$.
- FIG. 4. The dependence of the growth rate Γ on beam density: (a) at resonance ($k_z = 0$) and (b) off resonance ($k_z = 66.11 \text{ m}^{-1}$). The common parameters are $\ell = 7$, $r_o = 0.06 \text{ m}$, $r_w = 0.0865 \text{ m}$, $\hat{\beta}_{\theta_o} = 0.85$, $\hat{\beta}_{z_o} = 0.5$, and $x_o = 0$.
- FIG. 5. The dependence of the growth rate Γ on axial wave number: (a) Γ along a beam line and (b) the corresponding dispersion curves. Parameters: $\ell = 11$, $n_r = 1-3$, $n_s = 10^8 \text{ m}^{-2}$, $r_o = 0.06 \text{ m}$, $r_w = 0.10 \text{ m}$, $\hat{\beta}_{\theta_o} = 0.85$, $\hat{\beta}_{z_o} = 0.5$, and $x_o = 0$. Single particle results are indicated by \square .
- FIG. 6. The dependence of the growth rate Γ on beam thickness. Parameters: $\ell = 7$, $n_r = 1$, $n_s = 10^8 \text{ m}^{-2}$, $r_o = 0.06 \text{ m}$, $r_w = 0.09 \text{ m}$, $\hat{\beta}_{\theta_o} = 0.85$, $\hat{\beta}_{z_o} = 0.5$, and $k_z = 0$. Linear expansion ∇ , exact solution Δ .
- FIG. 7. The dependence of $\hat{\psi}_\ell$ on the axial wave number for a coaxial system: (a) ω_r and (b) Γ . Parameters: $\ell = 7$, $n_r = 1$, $n_s = 10^{11} \text{ m}^{-2}$, $r_o = 0.075 \text{ m}$, $r_i = 0.0626$, $r_w = 0.10 \text{ m}$, $\hat{\beta}_{\theta_o} = 0.9$, $\hat{\beta}_{z_o} = 0.4$, and $x_o = 0$.

FIG. 8. The convergence of the truncated solutions for Γ : 20 (Δ), 30 (∇), 40 (\circ), and 50 (\square) eigenvectors. Parameters: $\ell = 7$, $n_r = 1$, $r_o = 0.06$ m, $r_w = 0.0865$ m, $\hat{\beta}_{\theta_o} = 0.85$, $\hat{\beta}_{z_o} = 0.5$, $n_s = 10^8$ m $^{-2}$, $k_z = 0$, and $\hat{z} = 2.0$.

FIG. 9. The effect of the density profile on Γ . The common parameters are $\ell = 7$, $n_r = 1$, $n_s = 10^8$ m $^{-2}$, $r_o = 0.06$ m, $r_w = 0.0865$ m, $\hat{\beta}_{\theta_o} = 0.85$, $\hat{\beta}_{z_o} = 0.5$, and $k_z = 0$. Models: \square single particle, \diamond $\rho = 0.95$, Δ $\hat{z} = 1.0$, and ∇ $\hat{z} = 2.0$.

FIG. 10. Comparison of the three methods of solution for Γ . The common parameters are those of Fig. 9. Models: \square single particle, \circ analytic, and \diamond numeric: $\rho = 0.95$.

FIG. 11. The effect of axial wavelength on the growth rate Γ . Common parameters: $\ell = 7$, $n_r = 1$, $r_o = 0.06$ m, $\hat{\beta}_{\theta_o} = 0.85$, $\hat{\beta}_{z_o} = 0.5$, and $\hat{z} = 2.0$. Models: \square single particle; Δ $n_s = 10^8$ m $^{-2}$, $r_w = 0.0865$ m, and $k_z = 0$; ∇ $n_s = 10^8$ m $^{-2}$, $r_w = 0.0860$ m, and $k_z = 1.16$ m $^{-1}$; \diamond $n_s = 10^6$ m $^{-2}$, $r_w = 0.0864$ m, and $k_z = 0.251$ m $^{-1}$; and \circ $n_s = 10^{10}$ m $^{-2}$, $r_w = 0.0843$ m, and $k_z = 5.41$ m $^{-1}$.

FIG. 12. The effect of axial wavelength on the growth rate of a coaxial system. Common parameters: $\ell = 7$, $n_r = 1$, $n_s = 10^8$ m $^{-2}$, $r_o = 0.075$ m, $r_i = 0.063$ m, $r_w = 0.10$ m, $\hat{\beta}_{\theta_o} = 0.9$, and $\hat{\beta}_{z_o} = 0.4$. Models: \square single particle, \diamond $k_z = 0$, Δ $k_z = 0.3$ m $^{-1}$ and $\hat{z} = 1.0$, and ∇ $k_z = 0.3$ m $^{-1}$ and $\hat{z} = 2.0$.

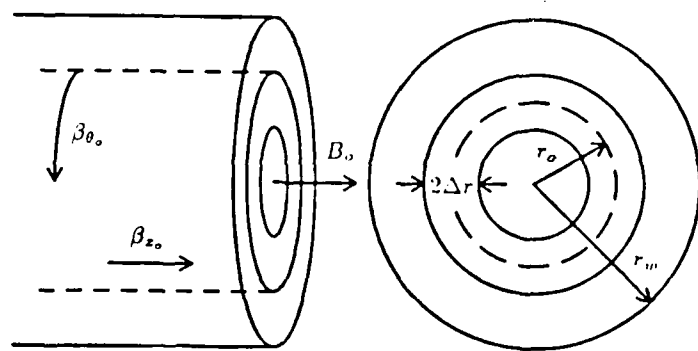


FIG. 1

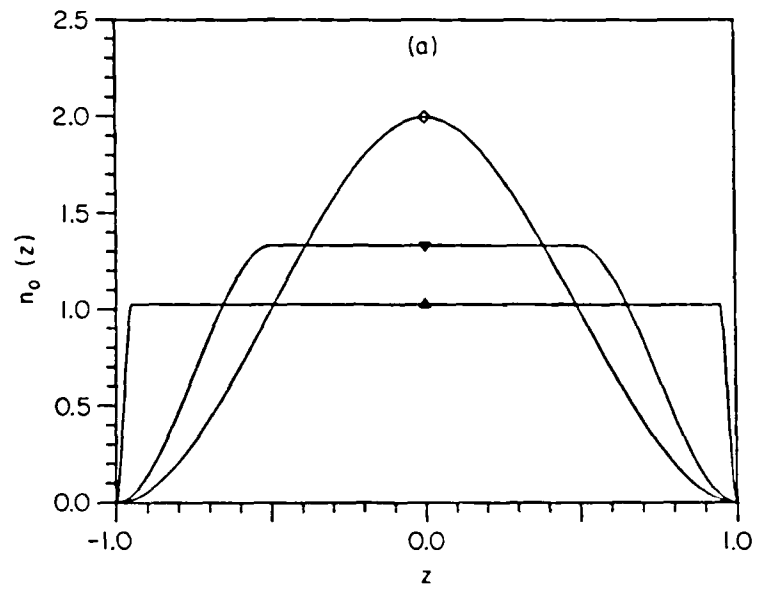


FIG. 2(a)

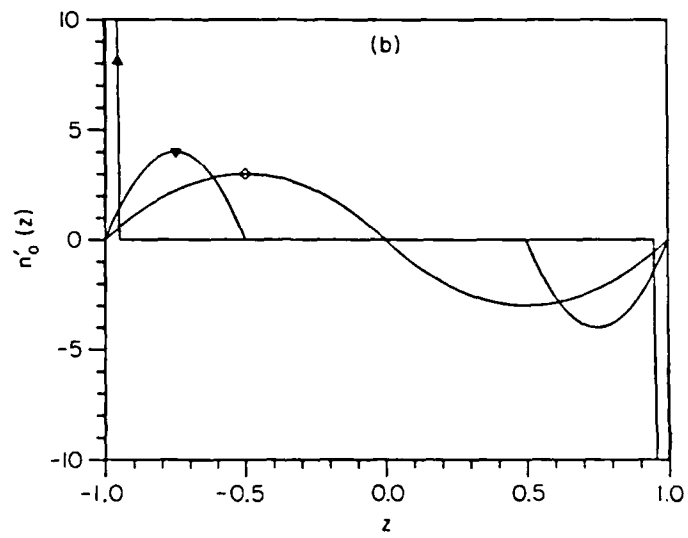


FIG. 2(b)

AD-A168 794

EXPERIMENTAL AND THEORETICAL INVESTIGATION OF MICROWAVE
MILLIMETER RADIAT (U) MARYLAND UNIV COLLEGE PARK LAB
FOR PLASMA AND FUSION ENERGY S W W DESTLER 30 NOV 85
AFOSR-TR-86-0280 AFOSR-83-0013

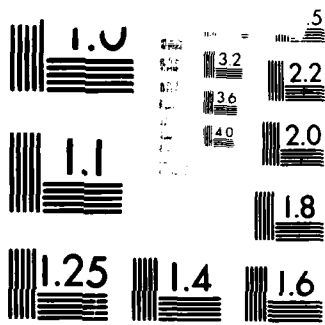
2/2

UNCLASSIFIED

F/G 28/14

NL





WILSON J. BROWN, JR.

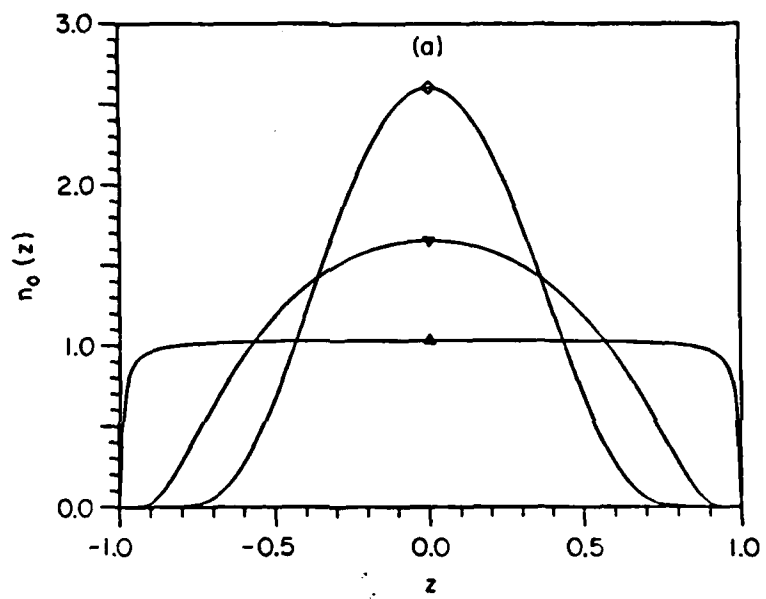


FIG. 3(a)

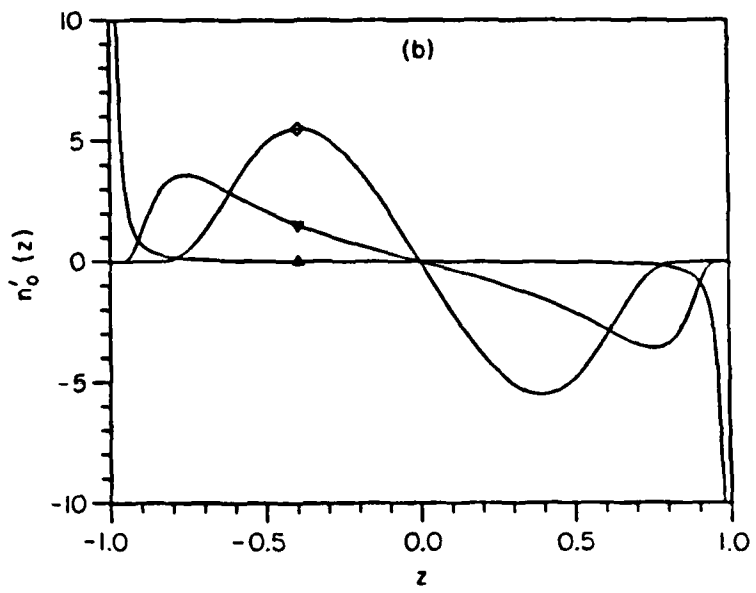


FIG. 3(b)

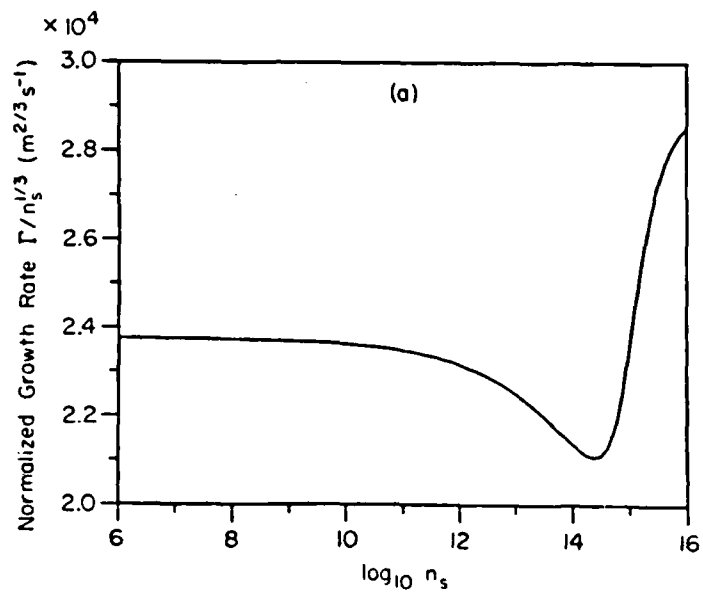


FIG. 4(a)

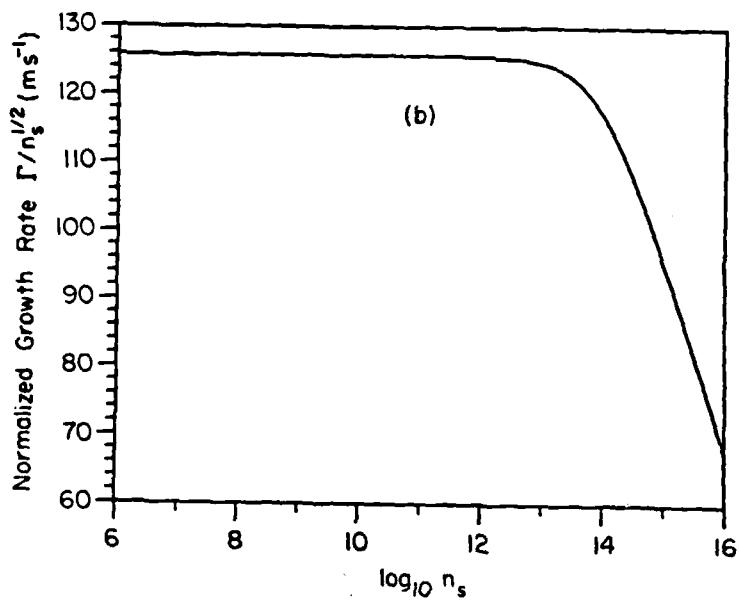


FIG. 4(b)

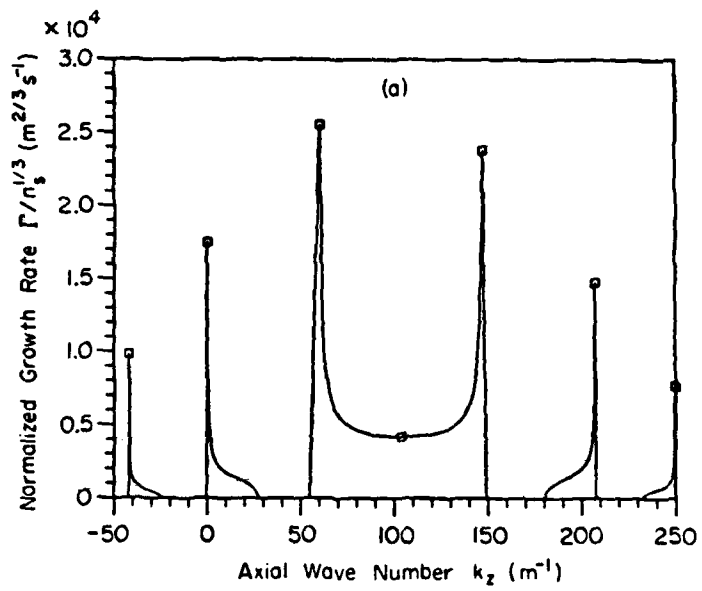


FIG. 5(a)

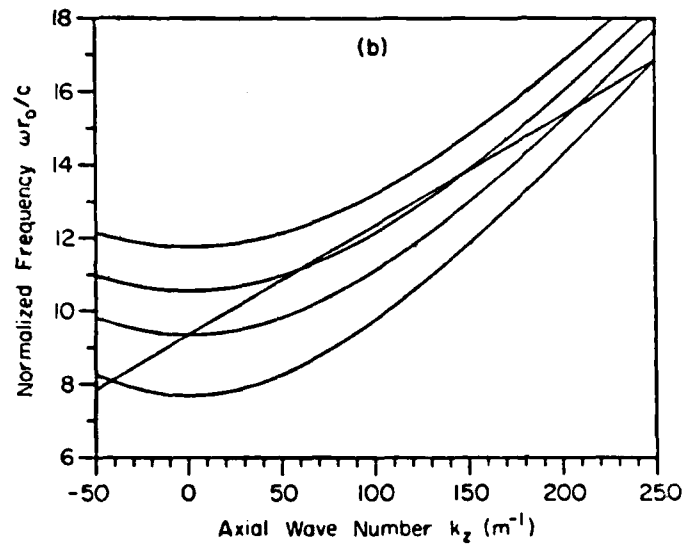


FIG. 5(b)

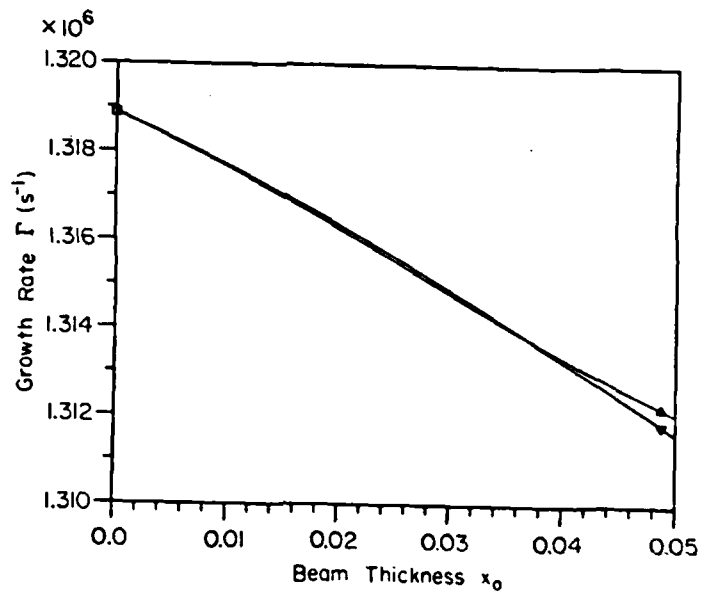


FIG. 6

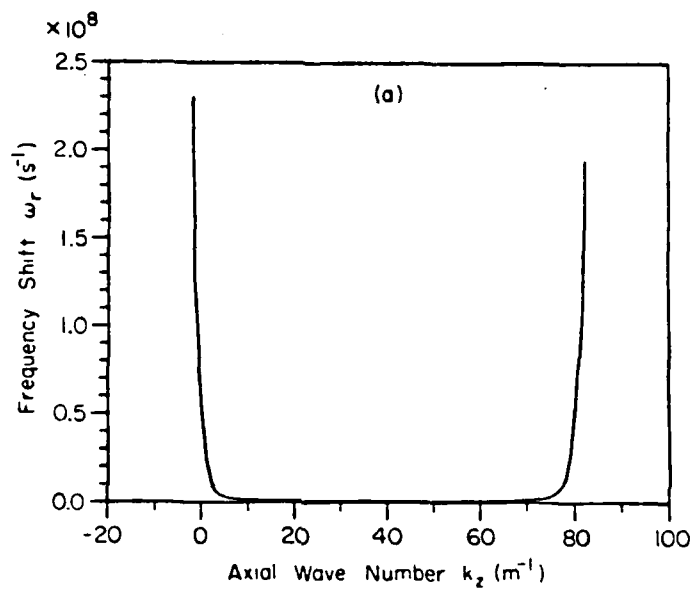


FIG. 7(a)

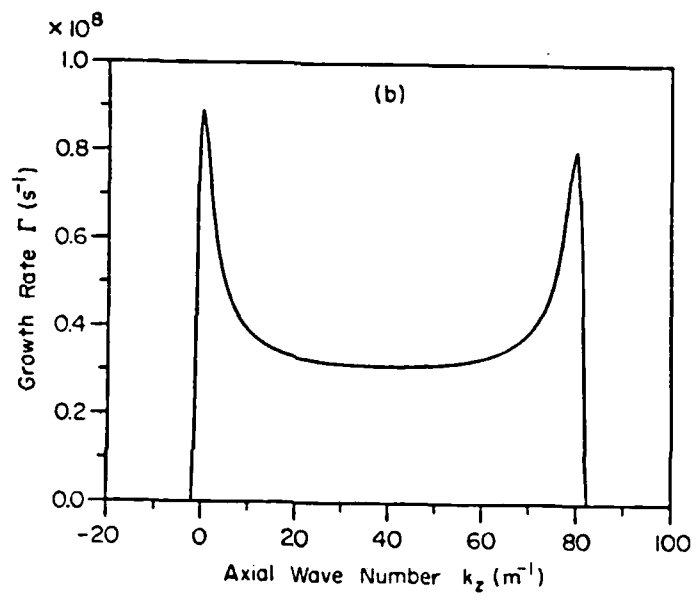


FIG. 7(b)

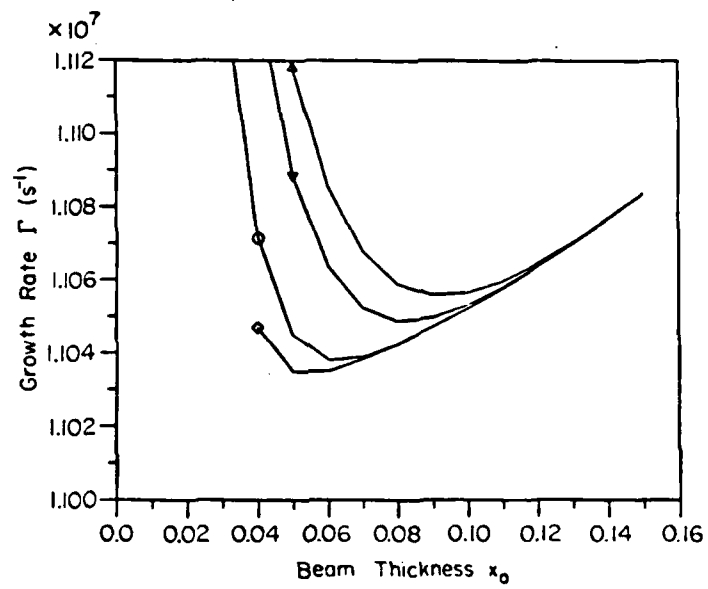


FIG. 8

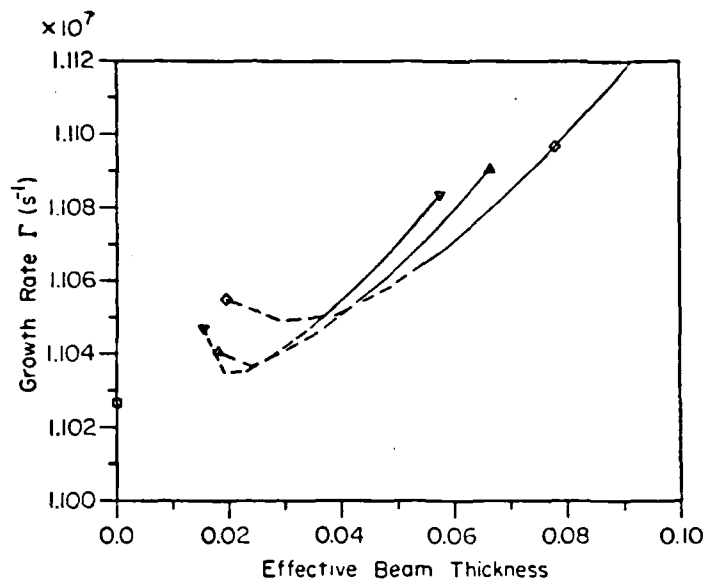


FIG. 9

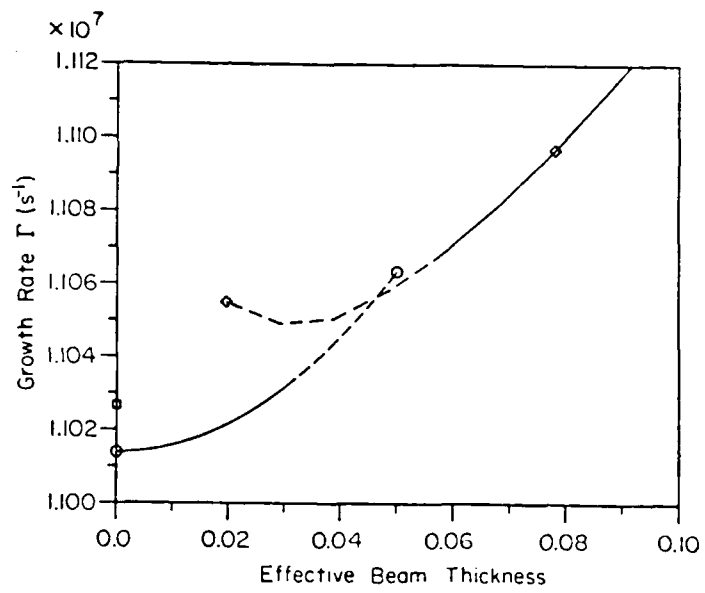


FIG. 10

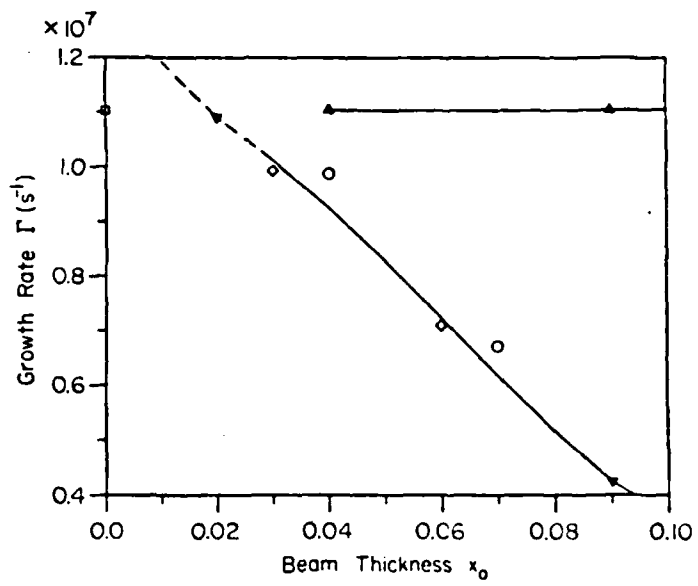


FIG. 11

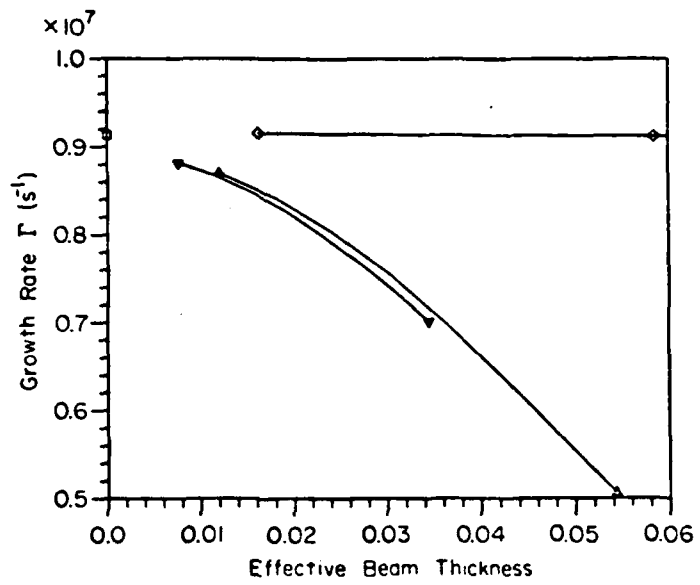


FIG. 12

END

Ditic

7-86